

A Digital Twin for Offshore Mooring Chains based on Acoustic Emission Monitoring

Riccioli, F.

DOI

[10.4233/uuid:974c17df-db78-4fe1-b947-68067471a95a](https://doi.org/10.4233/uuid:974c17df-db78-4fe1-b947-68067471a95a)

Publication date

2025

Document Version

Final published version

Citation (APA)

Riccioli, F. (2025). *A Digital Twin for Offshore Mooring Chains based on Acoustic Emission Monitoring*. [Dissertation (TU Delft), Delft University of Technology]. <https://doi.org/10.4233/uuid:974c17df-db78-4fe1-b947-68067471a95a>

Important note

To cite this publication, please use the final published version (if applicable).
Please check the document version above.

Copyright

Other than for strictly personal use, it is not permitted to download, forward or distribute the text or part of it, without the consent of the author(s) and/or copyright holder(s), unless the work is under an open content license such as Creative Commons.

Takedown policy

Please contact us and provide details if you believe this document breaches copyrights.
We will remove access to the work immediately and investigate your claim.

A Digital Twin for Offshore Mooring Chains based on Acoustic Emission Monitoring

Filippo Riccioli



A Digital Twin for Offshore Mooring Chains based on Acoustic Emission Monitoring

Filippo Riccioli

A Digital Twin for Offshore Mooring Chains based on Acoustic Emission Monitoring

Dissertation

for the purpose of obtaining the degree of doctor
at Delft University of Technology
by the authority of the Rector Magnificus prof.dr.ir. T.H.J.J. van der Hagen
chair of the Board for Doctorates
to be defended publicly on
Wednesday 22, October 2025 at 10:00 o'clock

by

Filippo RICCIOLI
Master of Science in Naval Engineering, University of Genova, Italy
born in Carate Brianza, Italy

This dissertation has been approved by the promotor.

Composition of the doctoral committee:

Rector Magnificus,	chairperson
Prof.dr.ir. B.J. Boersma,	Delft University of Technology, promotor
Dr. L. Pahlavan,	Delft University of Technology, promotor

Independent members:

Prof.dr.ir. J.M.C. Mol,	Delft University of Technology, NL
Prof.dr. C. Kassapolou,	Delft University of Technology, NL
Prof.dr. C. Rizzo,	University of Genova, IT
Dr.ir. J.H. den Besten,	Delft University of Technology, NL
Dr. A. Duggal,	SOFEC, USA

This research was supported and funded by the DONUT Joint Industry Project (JIP), Top consortium for Knowledge and Innovation Maritime (TKI Maritime) of the Netherlands Enterprise Agency (RVO), and Delft University of Technology (TU Delft).



Printed by: Ridderprint, The Netherlands.

Cover by: Filippo Riccioli.

Copyright © 2025 by F. Riccioli.

ISBN/EAN: 978-94-6384-838-1

An electronic copy of this dissertation is available at: <https://repository.tudelft.nl/>

To Giovanni, Rosa Maria, and Edoardo

Summary

High energy demand of contemporary society increasingly relies on offshore production. Offshore floating energy production infrastructure, such as floating wind turbines, photovoltaics, and production storage and offloading units, is central to sustaining the energy supply. Mooring chains, which are crucial elements of these floating units, are particularly vulnerable to degradation mechanisms, such as corrosion, fatigue, and their combination. Their frequent inspection is critical to prevent structural failure, production shutdowns, and severe environmental consequences.

A Digital Twin (DT) is a virtual representation of a physical object that uses real-time data to simulate and predict its behaviour. Digital twins have emerged as promising tools, enhancing the monitoring and management of physical assets using real-time data and predictive models. The effectiveness and reliability of a DT for quantitative integrity assessment are contingent on the quality of the input data and the models employed. When paired with predictive models, DTs offer valuable insights for managing the integrity of offshore mooring systems.

The main contribution of this work is to lay the groundwork for enrichment of DTs for mooring chains with quantitative damage assessment. Assessing the structural integrity of submerged offshore mooring chains presents significant challenges due to their difficult accessibility and the complexities involved in subsea inspections. Additionally, the presence of marine growth on the chain links often requires cleaning before detailed inspections can be conducted. The cleaning process is often undesirable from technical, economic, and environmental perspectives. Currently, no in-water inspection techniques for mooring chains have been reported that do not

require the removal of marine growth beforehand. Enabling this is another contribution area of this research.

This thesis proposes a novel non-contact acoustic emission (AE) monitoring approach in underwater environments, enhancing DTs of mooring chains without suffering from the limitations of conventional inspection methods. As a passive ultrasound method, AE is an established non-destructive testing (NDT) technique to detect and monitor corrosion and fatigue. Piezoelectric sensors, typically mounted in contact with the material surface, are often employed to capture high-frequency waves generated by damage initiation and propagation. Three key areas have been explored: (i) the feasibility of detecting and monitoring corrosion-fatigue in submerged conditions, both with and without marine growth, using non-contact AE, (ii) the construction of a DT representation based on AE data to identify the location of corrosion-fatigue damage in mooring chain links, and (iii) the integration of AE data with fatigue models to enhance the DT predictive capabilities for damage prognosis.

The feasibility of monitoring corrosion-fatigue damage in submerged conditions using non-contact AE monitoring has been explored using small-scale corrosion-fatigue experiments. The results demonstrated the effectiveness of the proposed approach, with corrosion-fatigue-induced ultrasound signals being detected with a satisfactory signal-to-noise ratio within the frequency range of 50–450 kHz. Cumulative and rate values of AE parameters provided a reliable representation of damage progression, successfully identifying four distinct stages of damage evolution. AE energy, in particular, proved to be the most promising indicator, especially for highlighting crack formation and rapid growth phases. Corrosion-fatigue-induced signals exhibited significantly higher energy levels, approximately an order of magnitude greater than those induced by corrosion alone. In addition, corrosion-induced damage resulted in fewer ultrasound signals than corrosion-fatigue damage. Further experiments demonstrated that simulated crack signals could be measured on steel plates both with and without marine growth, indicating

that ultrasound waves in the frequency range of interest can penetrate marine growth and be detected by non-contact AE transducers in submerged conditions. While marine growth caused a noticeable drop in signal amplitude, the findings suggest that non-contact AE monitoring remains feasible in the presence of marine growth.

Large-scale experiments have been used to construct a DT representation based on AE data to identify the location of corrosion-fatigue damage in mooring chain links. Large-scale corrosion and fatigue tests were conducted to assess the feasibility of detecting, localising, and monitoring corrosion and fatigue damage in mooring chains. The results demonstrated the effectiveness of the proposed approach in monitoring growing damage over time. AE measurements were parameterised to track acoustic activity associated with the initiation and progression of corrosion-fatigue damage. A 3D source localisation algorithm was successfully implemented to localise damage-induced ultrasound signal sources, with the localisation results being mapped onto the surfaces of the mooring chain segment. In the fatigue test, the AE-based DT identified three distinct zones of acoustic activity, which aligned well with post-failure inspection results. The remote AE technique accurately detected and localised all damage indications found during post-failure mechanical testing, showcasing its potential for real-time damage detection and localisation in mooring chain links.

Large-scale fatigue test data were subsequently used to assess the feasibility of fatigue crack growth prognosis in submerged mooring chains using remote AE monitoring. A prognosis model, based on the Paris relation and AE energy, was proposed, and its predictive capabilities were evaluated. The results demonstrated the potential of remote AE monitoring to predict fatigue crack growth in submerged mooring chains. AE energy analysis at various test stages revealed distinct phases of crack growth, including initiation, stable propagation, and acceleration toward failure. The prognosis model effectively reflected these stages, as indicated by changes in AE energy rate. A sensitivity analysis on the model parameters showed that reducing the scaling coefficient B led to overestimated crack growth and shorter

predicted fatigue life, while increasing it resulted in underestimated crack growth and longer predicted fatigue life. The power-law exponent p further amplified these effects. The fatigue life predictions underscored the importance of accurately determining the initial crack size and selecting the appropriate crack growth models to improve prognosis accuracy.

This research provides a foundation for enhancing DTs of offshore mooring chains through real-time monitoring and predictive analysis. The proposed system shows potential for autonomous inspections of subsea structures, with possible benefits including reduced inspection costs, condition-based maintenance, and improved safety. Its non-intrusive nature may also lessen disturbance to marine ecosystems. Demonstration under offshore conditions will be an important next step to assess and strengthen its practical value for supporting the safety, efficiency, and sustainability of floating energy infrastructure.

Samenvatting

De hoge energievraag van de hedendaagse samenleving steunt in toenemende mate op offshoreproductie. Drijvende offshore-energieproductie-infrastructuur, zoals drijvende windturbines, fotovoltaïsche systemen en productie-, opslag- en overslagunits, is essentieel voor het waarborgen van de energievoorziening. Afmeerkettingen, die cruciale elementen vormen van deze drijvende eenheden, zijn bijzonder kwetsbaar voor degradatiemechanismen zoals corrosie, vermoeiing en combinaties van beide. Regelmatige inspectie van afmeerkettingen is van groot belang om structureel falen, productiestilstanden en ernstige milieugevolgen te voorkomen.

Een Digital Twin (DT) is een virtuele representatie van een fysiek object die gebruikmaakt van realtime gegevens om het gedrag ervan te simuleren en te voorspellen. Digital twins zijn naar voren gekomen als veelbelovende hulpmiddelen die het monitoren en beheren van fysieke assets verbeteren door middel van realtime data en voorspellende modellen. De effectiviteit en betrouwbaarheid van een DT voor kwantitatieve integriteitsbeoordeling is afhankelijk van de kwaliteit van de ingevoerde gegevens en de gebruikte modellen. In combinatie met voorspellende modellen bieden DT's waardevolle inzichten voor het beheren van de integriteit van offshore ankersystemen.

De belangrijkste bijdrage van dit werk is het leggen van de basis voor de verrijking van DT's voor afmeerkettingen met kwantitatieve schadebeoordeling. Het beoordelen van de structurele integriteit van onderwater offshore afmeerkettingen brengt aanzienlijke uitdagingen met zich mee vanwege hun moeilijke toegankelijkheid en de complexiteit van onderwaterinspecties. Bovendien vereist de aanwezigheid van mariene aangroei op de schakels vaak reiniging voordat

gedetailleerde inspecties kunnen worden uitgevoerd. Dit reinigingsproces is vaak onwenselijk vanuit technisch, economisch en ecologisch perspectief. Momenteel zijn er geen technieken voor onderwaterinspectie van ankerkettingen gerapporteerd die niet vooraf het verwijderen van mariene aangroei vereisen. Het mogelijk maken hiervan vormt een ander onderzoeksgebied binnen dit werk.

Dit proefschrift stelt een nieuwe contactloze akoestische emissie (AE) monitoringsaanpak voor in onderwateromgevingen, waarmee DT's van afmeerkettingen kunnen worden verbeterd zonder de beperkingen van conventionele inspectiemethoden. Als een passieve ultrasone methode is AE een gevestigde niet-destructieve testtechniek (NDT) om corrosie en vermoeiing te detecteren en te monitoren. Piëzo-elektrische sensoren, die doorgaans in contact met het materiaaloppervlak worden gemonteerd, worden vaak gebruikt om hoogfrequente golven vast te leggen die worden gegenereerd door schade-initiatie en -propagatie. Drie belangrijke gebieden zijn onderzocht: (i) de haalbaarheid van het detecteren en monitoren van corrosievermoeiing in onderwatercondities, zowel met als zonder mariene aangroei, met behulp van contactloze AE, (ii) de opbouw van een DT representatie op basis van AE-gegevens om de locatie van corrosievermoeiingsschade in afmeerkettingschakels te identificeren, en (iii) de integratie van AE-gegevens met vermoeiingsmodellen om de voorspellende capaciteiten van DT's voor schadeprognoses te versterken.

De haalbaarheid van het monitoren van corrosievermoeiingsschade in onderwater omstandigheden met behulp van contactloze AE-monitoring is onderzocht met kleinschalige corrosievermoeiingsexperimenten. De resultaten toonden de effectiviteit van de voorgestelde aanpak aan, waarbij door corrosievermoeiing geïnduceerde ultrasone signalen werden gedetecteerd met een toereikend signaal-ruisverhouding binnen het frequentiebereik van 50–450 kHz. Cumulatieve en snelheidswaarden van AE-parameters gaven een betrouwbare weergave van schadeprogressie en identificeerden met succes vier verschillende fasen van schadeontwikkeling. Vooral AE-energie bleek de meest veelbelovende indicator, in

het bijzonder voor het markeren van scheurvorming en snelle groeifasen. Door corrosievermoeiing geïnduceerde signalen vertoonden aanzienlijk hogere energieniveaus, ongeveer een orde groter dan signalen veroorzaakt door corrosie alleen. Bovendien leidde corrosieschade tot minder ultrasone signalen dan corrosievermoeiingsschade. Verdere experimenten toonden aan dat gesimuleerde scheursignalen konden worden gemeten op stalen platen, zowel met als zonder mariene aangroei, wat aangeeft dat ultrasone golven in het relevante frequentiebereik mariene aangroei kunnen doordringen en worden gedetecteerd door contactloze AE-transducers in onderwater omstandigheden. Hoewel mariene aangroei een merkbare afname in signaalamplitude veroorzaakte, suggereren de bevindingen dat contactloze AE-monitoring haalbaar blijft in aanwezigheid van mariene aangroei.

Grootschalige experimenten zijn gebruikt om een DT representatie op te bouwen op basis van AE-gegevens om de locatie van corrosievermoeiingsschade in afmeerkettingsschakels te identificeren. Grootschalige corrosie- en vermoeiingstesten zijn uitgevoerd om de haalbaarheid van het detecteren, lokaliseren en monitoren van corrosie- en vermoeiingsschade in afmeerkettingen te beoordelen. De resultaten toonden de effectiviteit van de voorgestelde aanpak aan bij het monitoren van toenemende schade in de tijd. AE-metingen werden geparameteriseerd om akoestische activiteit die verband houdt met de initiatie en progressie van corrosievermoeiingsschade te volgen. Een 3D-bronlokalisatie-algoritme werd met succes geïmplementeerd om door schade geïnduceerde ultrasone signaalbronnen te lokaliseren, waarbij de lokalisatieresultaten werden geprojecteerd op de oppervlakken van het ankerkettingsegment. In de vermoeiingstest identificeerde de AE-gebaseerde DT drie afzonderlijke zones van akoestische activiteit, die goed overeenkwamen met de inspectieresultaten na falen. De remote AE-techniek detecteerde en lokaliseerde nauwkeurig alle schade-indicaties die tijdens mechanische testen na falen werden gevonden, wat de potentie aantoont voor realtime schade-detectie en lokalisatie in ankerkettingsschakels.

Grootschalige vermoeiingstestgegevens zijn vervolgens gebruikt om de haalbaarheid van het voorspellen van vermoeiingsscheurgroei in onverwater afmeerkettingen met behulp van remote AE-monitoring te beoordelen. Een prognosemodel, gebaseerd op de relatie van Paris en AE-energie, werd voorgesteld en de voorspellende capaciteiten ervan werden geëvalueerd. De resultaten toonden het potentieel van remote AE-monitoring aan om vermoeiingsscheurgroei in onderwater afmeerkettingen te voorspellen. AE-energieanalyse in verschillende testfasen onthulde duidelijke fasen van scheurgroei, waaronder initiatie, stabiele propagatie en versnelling richting falen. Het prognosemodel weerspiegelde deze fasen effectief, zoals aangegeven door veranderingen in de AE-energiesnelheid. Een gevoeligheidsanalyse van de modelparameters liet zien dat het verlagen van de schaalcoëfficiënt B leidde tot overschatting van scheurgroei en kortere voorspelde vermoeiingslevensduur, terwijl verhoging ervan resulteerde in onderschatting van scheurgroei en langere voorspelde levensduur. De machtswet-exponent p versterkte deze effecten verder. De voorspellingen van de vermoeiingslevensduur onderstreepten het belang van een nauwkeurige bepaling van de initiële scheurafmeting en het selecteren van de juiste scheurgroeimodellen om de prognose-nauwkeurigheid te verbeteren.

Dit onderzoek vormt een basis voor het verbeteren van DT's van offshore afmeerkettingen door realtime monitoring en voorspellende analyse. Het voorgestelde systeem toont potentieel voor autonome inspecties van onderwaterstructuren, met mogelijke voordelen zoals lagere inspectiekosten, conditiegebaseerd onderhoud en verbeterde veiligheid. Het niet-intrusieve karakter kan bovendien verstoring van mariene ecosystemen verminderen. Demonstratie onder offshorecondities zal een belangrijke volgende stap zijn om de praktische waarde ervan te beoordelen en te versterken ter ondersteuning van de veiligheid, efficiëntie en duurzaamheid van drijvende energie-infrastructuur.

Contents

Summary	7
Samenvatting	11
1 INTRODUCTION	20
1.1 DEGRADATION MECHANISMS OF OFFSHORE MOORING CHAINS	22
1.2 DIGITAL TWIN FOR MOORING INTEGRITY MANAGEMENT	23
1.3 STATE-OF-THE-ART METHODS FOR MOORING INTEGRITY ASSESSMENT	25
1.4 NON-CONTACT ACOUSTIC EMISSION MONITORING FOR DIGITAL TWIN OF MOORING CHAINS	30
1.5 RESEARCH OBJECTIVES	31
1.6 KNOWLEDGE GAP AND RESEARCH QUESTIONS	32
1.7 STRUCTURE OF THE THESIS	32
2 NON-CONTACT ACOUSTIC EMISSION MONITORING OF CORROSION-FATIGUE IN SUBMERGED STEEL STRUCTURES	36
2.1 INTRODUCTION	36
2.2 NON-CONTACT ACOUSTIC EMISSION MONITORING OF CORROSION-FATIGUE	37
2.2.1 ACOUSTIC EMISSION SOURCES DURING CORROSION-FATIGUE	39
2.2.2 MONITORING OF CORROSION-FATIGUE DAMAGE USING NON-CONTACT ACOUSTIC EMISSION	40
2.3 SMALL-SCALE EXPERIMENTS	41
2.3.1 EXPERIMENTAL SETUP AND TEST SPECIMEN	42
2.3.2 ACCELERATED CORROSION-FATIGUE PROCESS	45
2.3.3 ACOUSTIC EMISSION MEASUREMENTS	47

2.3.4	ATTENUATION DUE TO MARINE GROWTH	49
2.4	RESULTS AND DISCUSSION	51
2.4.1	RESULTS OF THE ARTIFICIAL MARINE GROWTH ATTENUATION STUDY	63
2.5	CONCLUSION	64
3	ACOUSTIC EMISSION-BASED DIGITAL TWIN FOR DIAGNOSIS OF CORROSION-FATIGUE DAMAGE IN SUBMERGED MOORING CHAINS	68
3.1	INTRODUCTION	68
3.2	DETECTION AND LOCALISATION OF CORROSION-FATIGUE USING NON-CONTACT ACOUSTIC EMISSION	69
3.2.1	ACOUSTIC EMISSION MONITORING OF CORROSION- FATIGUE	69
3.2.2	DIGITAL TWIN AND AE SOURCE LOCALISATION	70
3.3	FULL-SCALE EXPERIMENTS	72
3.3.1	FULL-SCALE FATIGUE TEST	73
3.3.2	FULL-SCALE CORROSION TEST	77
3.4	RESULTS AND DISCUSSION	80
3.4.1	DETECTION AND LOCALISATION OF FATIGUE	80
3.4.2	DETECTION AND LOCALISATION OF CORROSION	90
3.4.3	ENVISIONED IMPLEMENTATION	93
3.5	CONCLUSIONS	93
4	FATIGUE CRACK GROWTH PROGNOSIS IN SUBMERGED MOORING CHAINS USING NON-CONTACT ACOUSTIC EMISSION MONITORING	98
4.1	INTRODUCTION	98
4.2	FATIGUE CRACK GROWTH PROGNOSIS USING NON- CONTACT ACOUSTIC EMISSION	99
4.2.1	THEORETICAL MODEL FOR FATIGUE CRACK GROWTH PROGNOSIS USING ACOUSTIC EMISSION	101
4.2.2	CALCULATION OF MODEL PARAMETERS	102
4.2.3	ESTIMATION OF FATIGUE LIFE USING ACOUSTIC EMISSION	104
4.3	TEST DATA	106

	Contents
4.3.1	FULL-SCALE EXPERIMENT 106
4.3.2	ACOUSTIC EMISSION MEASUREMENTS 107
4.3.3	POST-FAILURE INSPECTION 108
4.4	RESULTS AND DISCUSSION 108
4.4.1	FATIGUE CRACK GROWTH PROGNOSIS 109
4.4.2	SENSITIVITY ANALYSIS 112
4.4.3	FATIGUE LIFE ESTIMATION 113
4.5	CONCLUSIONS 116
5	CONCLUSIONS & OUTLOOK 120
5.1	CONCLUSIONS 120
5.2	RECOMMENDATIONS 123
	Bibliography 125
	Acknowledgements 143
	Curriculum vitae 145
	List of publications 147

1

Introduction

1 INTRODUCTION

Contemporary society relies on exceptionally high energy demand, with approximately 80% of energy supplied by conventional fossil fuel sources. Of this, nearly 50% is derived from natural gas and oil, where offshore production plays a significant role. The remaining 20% of energy is produced from non-fossil sources, with onshore wind energy far exceeding offshore wind by a ratio of 9:1. Looking ahead, global energy demand is projected to nearly double by 2050, boosting a significant transition in energy production strategies. By that time, it is anticipated that fossil fuels will account for about 50% of the energy supply, with offshore production continuing to contribute substantially. At the same time, non-fossil energy sources are expected to rise to about 50%, with the gap between onshore and offshore wind narrowing to 3:1. World-installed floating offshore wind capacity is expected to rise to about 10 GW in the coming five years and reach nearly 220 GW in 2050 [1].

Floating wind turbines, photovoltaics, and production storage and offloading units are notable examples of floating energy production infrastructures (Figure 1.1).



Figure 1.1. Examples of floating energy production systems [2-3].

Mooring chains are key elements of offshore floating energy production systems. They are susceptible to various degradation mechanisms (Figure 1.2), primarily due to their exposure to seawater and cyclic loading.

Inspection and monitoring of mooring chains are essential to mitigating the risk of failures that could result in structural damage and catastrophic environmental consequences. At the same time, these practices can ensure continuous energy production by minimising the chances of unplanned downtime or disruption, which are vital for the uninterrupted generation and supply of energy.

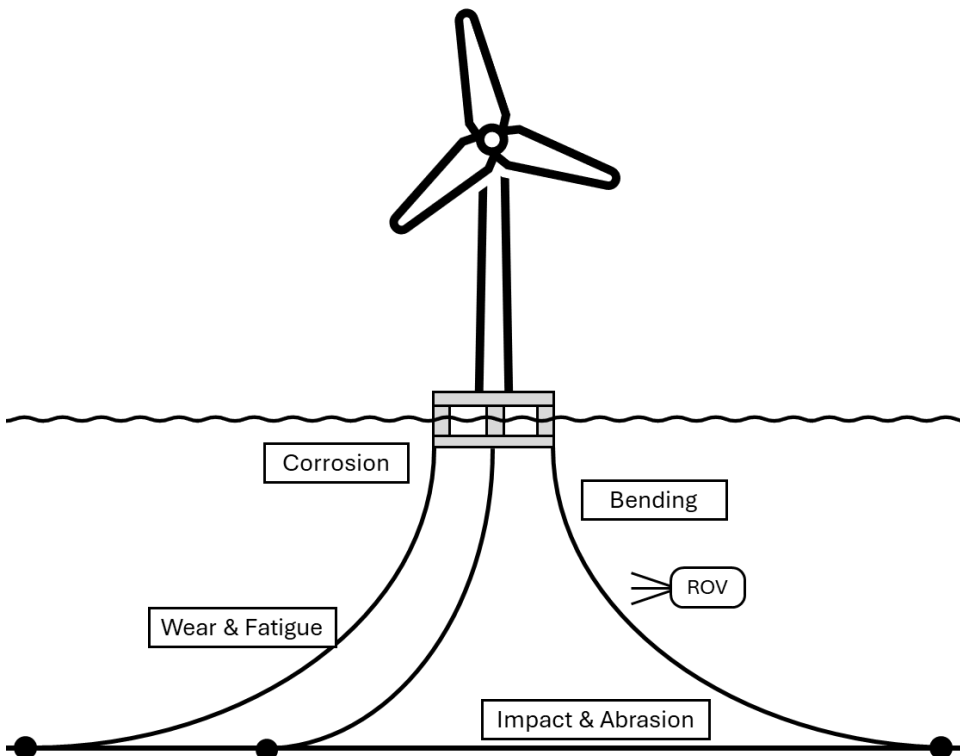


Figure 1.2. Example of a moored floating energy system, with mooring degradation mechanisms and failure modes. In addition to corrosion and fatigue (primary degradation mechanisms), other notable failure modes include wear, out-of-plane bending, and mechanical damage due to handling and installation processes [4-5].

1.1 DEGRADATION MECHANISMS OF OFFSHORE MOORING CHAINS

Offshore mooring chains are typically subject to cyclic loads and harsh marine environments, significantly impacting their structural integrity. The conditions of used mooring chains after several years of service are shown (Figure 1.3). The prolonged exposure to seawater induces the relatively slow deterioration of the chain metal surface due to corrosion. Repeated cyclic loading, even below the material ultimate strength, can lead to fatigue crack initiation and propagation over time. The combined effect of corrosion and cyclic loading, i.e. corrosion-fatigue [6], can further accelerate the degradation process.

Marine growth, such as algae, barnacles, and other biofouling organisms, often covers the mooring chains, posing significant challenges for damage detection. Layers of marine growth can also cover corrosion and cracks, hindering the effectiveness of visual inspections and other non-destructive testing methods.



Figure 1.3. Corrosion pits (left) and fatigue crack (centre) in used mooring chain links, and marine growth deposits on submerged mooring chains (right) [7].

Corrosion pits can act as initiation sites for fatigue cracks. These cracks, once formed, can propagate over time, compromising the chain structural integrity and longevity.

The design life of offshore mooring chains is typically between 20 and 25 years, with the expectation that they will withstand ‘100-year period storm’ conditions [5].

Despite this, early and unexpected failures have been recorded, emphasising the importance of monitoring and structural integrity assessments. Historical examples of such failure are documented [8-9].

1.2 DIGITAL TWIN FOR MOORING INTEGRITY MANAGEMENT

Digital Twins (DTs) have gained significant attention across various industries as tools to improve the monitoring and management of physical assets. A digital twin is defined as a virtual representation of a physical object (or process) capable of using real-time data to simulate, validate, and predict the behaviour of its physical counterpart [10]. This technology can assist informed decision-making using real-time monitoring and predictive analysis.

Michael Grieves first introduced the concept (and initial definition) of DT in 2002. Over time, several definitions of DT have been proposed. Generally, these definitions centre around three core elements: the physical object, its virtual representation, and the data connection between them (Figure 1.4).

Digital twins offer significant advantages for monitoring, predicting, and optimising system performance and maintenance across various industries. Digital twins provide actionable insights to improve reliability, safety, and operational efficiency by integrating real-time data with advanced modelling techniques. Their applications span across industries such as aerospace, civil engineering, process industries, and building management, where they contribute to cost reduction, enhanced system reliability, and improved energy performance. Different authors provided a detailed discussion of the benefits and applications of DTs [11-13].

In Building Information Modelling, Level of Development (LOD) defines the level of detail and reliability of the information in a model, which is crucial for developing a DT with appropriate precision and data fidelity. On the other hand, markers and glyphs are physical and digital indicators, such as Augmented Reality markers or

visual identifiers, used to anchor or synchronise digital models with real-world objects or environments for accurate interaction and alignment.

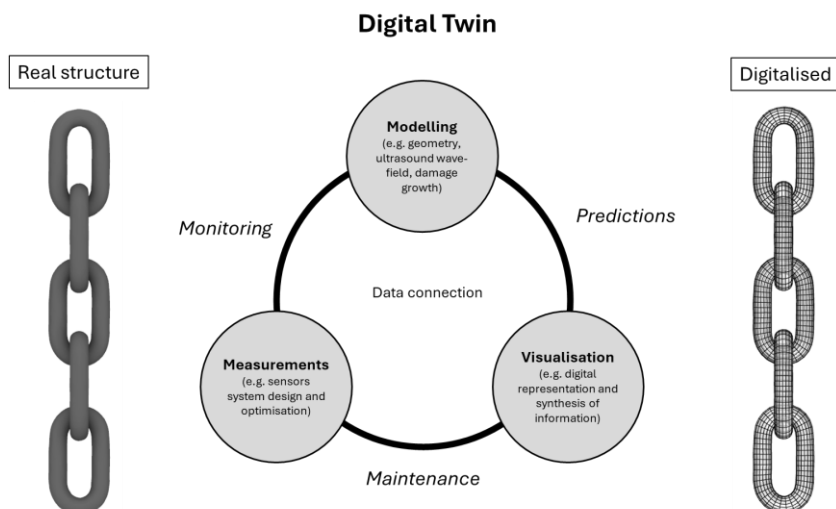


Figure 1.4. Schematic of the general definition of Digital Twin (DT).

The application of DTs in the integrity management of mooring systems has been expanding, with a few notable examples highlighted in [14-16]. Most of these DT implementations gather measurements related to load and other operational parameters to assess the presence of potential damage and/or failure. However, these parameters are often not directly linked to the physical damage, leading to gaps in accuracy, consistency, and understanding of structural integrity and reliability.

The focus of the DT in the present research is on the enhanced monitoring of mooring chains structural integrity by facilitating damage diagnosis (detection and localisation) and damage prognosis (using damage growth models). The quality and reliability of a DT primarily depend on the quality of the input information and the adopted models. It is therefore critical to have an accurate (and quantitative) integrity assessment technique to ensure the quality of the measured data. At the same time, integrating predictive models in the DT can unlock its full potential, offering enhanced insights into the integrity management of offshore mooring systems. Finally, proper data visualisation, presenting the data in a clear and actionable

manner, is key in output interpretation and facilitates informed decision-making. The main contribution of this work is laying the foundation for improved DTs for mooring chains.

1.3 STATE-OF-THE-ART METHODS FOR MOORING INTEGRITY ASSESSMENT

Structural integrity assessment of submerged offshore mooring chains can be challenging due to their difficult access and the required arrangements for subsea inspections. Furthermore, the presence of marine growth on the surface of the chain links often necessitates surface cleaning before a detailed inspection can be performed [5]. While necessary, the cleaning process (Figure 1.5) is generally undesirable from technical, economic, and environmental points of view.

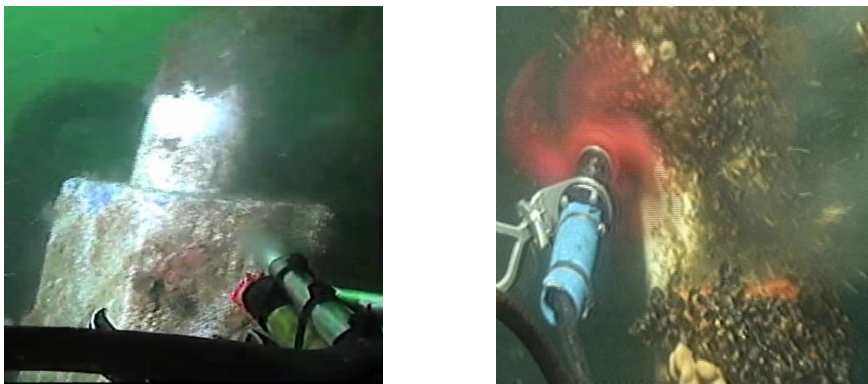


Figure 1.5. Examples of marine growth cleaning process [17-18].

Marine growth cleaning is typically performed using high-pressure water jetting and/or brushes. Unfortunately, this process may accelerate corrosion by exposing fresh steel to the corrosive effects of saltwater [5]. Currently, there are no in-water inspection methods for mooring chains that do not require the prior removal of marine growth. This has been representing a technology gap for 20 years now.

So far, various methods have been proposed for non-intrusive integrity assessment of mooring chains, though many exhibit suboptimal reliability or are constrained by operational conditions (for example, requiring marine growth cleaning). Visual

inspection (Figure 1.6), for instance, can be performed in wet and dry conditions after surface cleaning [19]. However, only relatively large-sized surface defects (in the order of mm) can be detected by this technique. When conducted underwater, inspection results can also be influenced by the clarity of the seawater, which imposes strict requirements on lighting conditions. This technique often needs further damage inspection using more advanced Non-Destructive Testing (NDT) methods after surface cleaning.



Figure 1.6. Examples of visual inspection of mooring chains in wet (left) and dry (right) conditions [20-21].

Magnetic Particle Inspection (MPI) can detect surface and near-surface flaws in ferromagnetic materials in wet and dry conditions [22-25]. Results of the analysis, such as the true length of discontinuities, may be obtained with reasonable accuracy [26]. Nonetheless, deeply embedded flaws cannot be detected using this technique, and application of the method also requires surface cleaning [19]. Eddy-Current (EC) Testing and Magnetic Flux Leakage (MFL) are also electromagnetic testing methods, and both can also be applied underwater. Although EC testing is a non-contact technique, meaning it does not require surface preparation or cleaning, it is sensitive to variations in the distance between the probe and the surface (lift-off) and is limited to detecting surface or near-surface defects [26]. On the other hand, MFL can identify defects deeper within the material, but only where the clean material

surface can be accessed. Examples of MPI and EC applications are shown (Figure 1.7).



Figure 1.7. Examples of Magnetic Particle Inspection and Eddy-Current Testing [27-28].

Ultrasonic testing (Figure 1.8) can detect and size surface and subsurface defects and even be used for weld inspection [22]. Guided ultrasonic waves allow for the localisation of cracks and notches, probing larger areas of the structure from a few monitoring points. This method requires proper coupling between the material surface (after preparation, i.e. cleaning) and probes. Generally, the accuracy and reliability of all these methods are adversely affected by the presence of corrosion pits on the material surface.

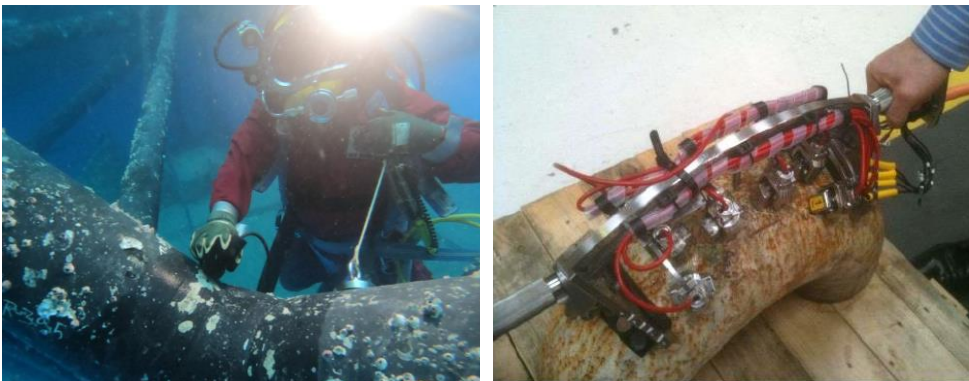


Figure 1.8. Examples of Ultrasonic testing of offshore support structures in wet (left) [29] and dry (right) [30] conditions.

Radiography techniques can image internal and surface defects using high-energy electromagnetic waves. However, their subsea utilisation is limited due to safety hazards and environmental concerns [22]. In recent years, underwater 3D scanning has gained significant popularity as an advanced tool for offshore mooring chain inspections. This technique allows the collection of detailed 3D images of underwater structures, which can be captured before or after surface cleaning. When combined with sophisticated image processing algorithms, 3D scanning can provide information regarding the severity of corrosion on a structure such as mooring chains [31-32]. However, this accurate assessment requires cleaning the surface of marine growth to reveal the condition of the underlying material. The potential of 3D scanning is undeniable however, its true value emerges when integrated with more quantitative techniques and advanced data processing methods. Examples of radiography underwater inspection and results of underwater 3D scanning are shown (Figure 1.9).

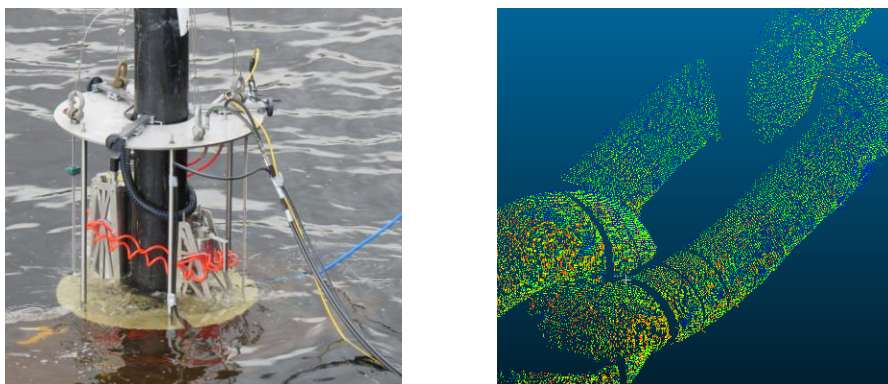


Figure 1.9. Examples of radiography underwater inspection (left) [33-34] and results of underwater 3D scanning technique (right) [35].

Acoustic Emission (AE), a passive ultrasound method, is an established technique for detecting and monitoring corrosion, fatigue, and corrosion-fatigue (i.e. simultaneous actions of corrosive environment and repeated stress [6]) using surface-bonded transducers [36-39]. AE enables damage identification, localisation, and characterisation by continuously monitoring the transient stress waves generated

by the rapid release of energy from localised sources within the material [40]. Piezoelectric sensors, typically in contact with the material surface, can capture high-frequency elastic waves. Measuring the arrival time of the waves at different sensors enables the localisation of AE sources in the material. The onset of new damage or progression of an active fault in the material structure is typically associated with localised AE events. Several authors conducted small-scale experiments to investigate corrosion and fatigue using AE [36; 41-57]. Despite promising results of corrosion and fatigue damage detection and monitoring using AE, only a few large-scale testing attempts have been made using mooring chains. Rivera et al. [58] conducted a long-term tensile test to evaluate the feasibility of monitoring crack initiation and growth in mooring chain links in artificial seawater using the AE technique (Figure 1.10, left). Similarly, Angulo et al. [59] carried out a 72-day large-scale fatigue experiment to assess the capabilities of AE as a monitoring tool to detect crack initiation and propagation in mooring chains under realistic loading and environmental conditions (Figure 1.10, right). Although both studies presented promising results for AE monitoring of cracks in mooring chain links, their approach does not overcome the limitations of conventional NDTs, i.e. marine growth removal for coupling between inspection probe and material structure.



Figure 1.10. Sample illustration of AE testing of mooring chain links [58-59].

1.4 NON-CONTACT ACOUSTIC EMISSION MONITORING FOR DIGITAL TWIN OF MOORING CHAINS

This thesis proposes a novel approach for non-contact AE monitoring in underwater environments. This approach addresses the limitations of conventional methods that rely on direct contact between sensors and the structure under assessment. Contact-based AE methods require material surface preparation such as cleaning and removing marine growth, particularly for underwater mooring chains. However, this process introduces critical drawbacks to the inspection procedure. Removing the marine growth can expose the underlying material to the underwater environment, potentially accelerating the corrosion rate of the chain links. Additionally, the material surface conditions (usually with small and large pits) can adversely affect the quality of sensor coupling, leading to unreliable inspection measurements. Marine growth cleaning is a labour-intensive and time-consuming process. As a result, it is often performed only at specific locations rather than along the entire mooring line, limiting the comprehensiveness of the structure integrity assessment. Furthermore, the operational costs of marine growth cleaning add a significant financial burden to the overall inspection process. Cleaning also disrupts marine biodiversity, even when efforts are made to collect the removed growth. In cases where cleaning is required to remove invasive alien species, the process can inadvertently cause the dispersion of these species into the marine environment, facilitating their spread. Further details on the advantages and drawbacks of currently used techniques can be found in the literature [4-5].

A schematic representation of the underwater non-contact AE technique applied to mooring chain links covered with marine growth is shown (Figure 1.11). In the non-contact AE approach, ultrasound waves can propagate in the water medium (after propagating through marine growth), which acts as a couplant, eliminating the need for direct contact with the structure. This method offers a much less intrusive alternative to conventional AE assessment and monitoring.

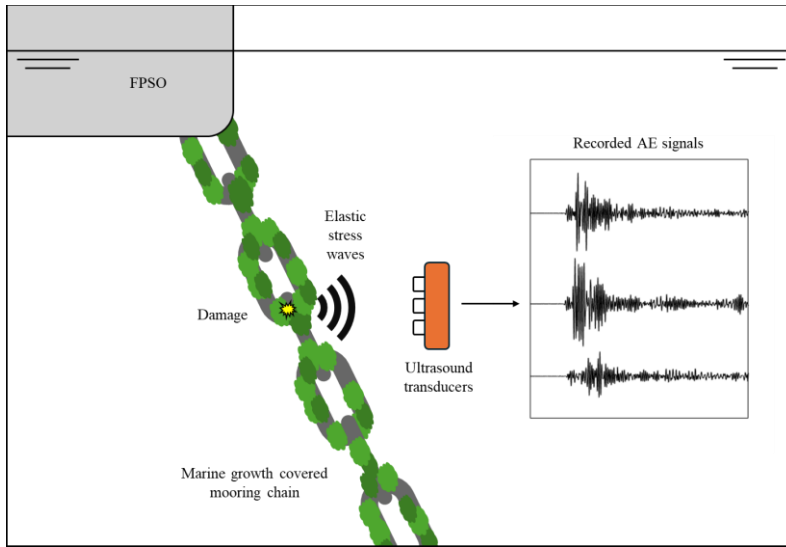


Figure 1.11. Schematic of underwater non-contact AE measurements for mooring chain links covered with marine growth.

Although a number of studies have been published on non-contact AE techniques [75-78], there is, to the best of the author's knowledge, no existing research specifically addressing the use of non-contact AE for underwater monitoring of mooring chain links.

1.5 RESEARCH OBJECTIVES

The primary objective of this dissertation is to present a methodology for enabling enhanced DTs of mooring chains by a novel underwater monitoring technique. The proposed method aims for non-intrusive and non-destructive diagnosis and prognosis of corrosion-fatigue damage in mooring chains. This method allows for structural integrity assessments without cleaning the marine growth from the material surface. Additionally, the proposed approach holds potential for remote operation, enabling real-time monitoring and reducing the need for manual inspections in harsh offshore environments.

1.6 KNOWLEDGE GAP AND RESEARCH QUESTIONS

Currently, there is a lack of effective underwater inspection/monitoring methods for mooring chains that (i) do not require prior removal of marine growth and (ii) can provide sufficiently quantitative damage information remotely. Addressing this gap is crucial to enable advanced DTs of mooring chains in submerged conditions.

To bridge this gap, the study investigates the following central research question:

- Can a prognostic digital twin of mooring chains be created using AE monitoring and fatigue models?

Four sub-questions further guide the research:

- Can AE monitoring in submerged conditions effectively detect and monitor corrosion-fatigue?
- Is it feasible to measure AE through layers of marine growth?
- Can a digital twin representation be constructed from AE data to indicate the location of corrosion-fatigue damage in mooring chain links?
- Can AE data be integrated with fatigue models to enhance the digital twin with predictive capabilities for damage prognosis?

1.7 STRUCTURE OF THE THESIS

This dissertation is built around three main chapters, which aim to answer the key research questions. Chapter 2 presents a feasibility assessment of detecting and monitoring corrosion-fatigue damage in submerged steel structures using non-contact AE measurements. The feasibility of measuring damage-induced AE through layers of marine growth is also addressed in this chapter. Chapter 3 explores the feasibility of constructing an AE-based DT through detection, localisation, and monitoring corrosion-fatigue damage in mooring chain links using remote AE technique in submerged conditions. Insights from full-scale fatigue and corrosion

experiments on mooring chains are presented in this chapter. Chapter 4 investigates the feasibility of using remote AE for crack growth prognosis in submerged mooring chain links. Conclusions drawn from the research and recommendations for future research directions are summarised in the last chapter.

2

Non-contact Acoustic Emission monitoring of corrosion-fatigue in submerged steel structures

This chapter is based on the journal article:

F. Riccioli, S. Alkhateeb, A. Mol, and L. Pahlavan, “Feasibility assessment of non-contact acoustic emission monitoring of corrosion-fatigue damage in submerged steel structures,” *Ocean Engineering*, vol. 312, p. 119296, Nov. 2024, doi: 10.1016/j.oceaneng.2024.119296.

2 NON-CONTACT ACOUSTIC EMISSION MONITORING OF CORROSION-FATIGUE IN SUBMERGED STEEL STRUCTURES

2.1 INTRODUCTION

Among existing methods for assessing the integrity of submerged steel structures, Acoustic Emission (AE) offers a high potential for monitoring and characterising corrosion-fatigue. The primary mechanisms responsible for the generation of AE are pitting, crack initiation, and/or propagation [41; 44; 56-57]. Secondary mechanisms can also be present in the context of corrosion monitoring, such as hydrogen bubble evolution (and friction at crack walls), debris fracturing, and corrosion product formation on metal surfaces [41; 56; 60].

Conventional approaches emphasize the necessity of contact between AE transducers and the material surface [36; 40]. This can facilitate the realization of high signal-to-noise ratio and precise AE source localisation. However, in scenarios involving complex geometries or inaccessible areas (e.g. submerged offshore structures), achieving proper coupling between the sensors and the material surface may be challenging. Non-contact AE offers a non-intrusive solution for measurements in such environments. Nonetheless, this technique may offer a lower signal-to-noise ratio and increased susceptibility to external disturbances (e.g. ambient noise). Assessing the detectability of AE signals, considering factors such as signal-to-noise ratio, AE energy, and number of AE signals measured during corrosion-fatigue, is crucial for enabling a non-intrusive integrity assessment of submerged offshore structures and mooring systems.

This chapter aims to demonstrate the feasibility of detecting and monitoring corrosion-fatigue damage in submerged steel structures using non-contact AE measurements. The findings of this study provide a basis for more efficient and

environmentally friendly procedures for the integrity assessment of mooring systems while enhancing the safety of energy production offshore. Corrosion-fatigue experiments were conducted on a dog-bone steel specimen. The AE parameters extracted from the measured signals were analysed as a function of the load cycles to assess the detectability and evolution of corrosion-fatigue-induced ultrasound signals.

2.2 NON-CONTACT ACOUSTIC EMISSION MONITORING OF CORROSION-FATIGUE

A schematic illustration of the non-contact AE measurement for a steel specimen submerged in seawater and subjected to corrosion-fatigue degradation is shown (Fig. 2.1).

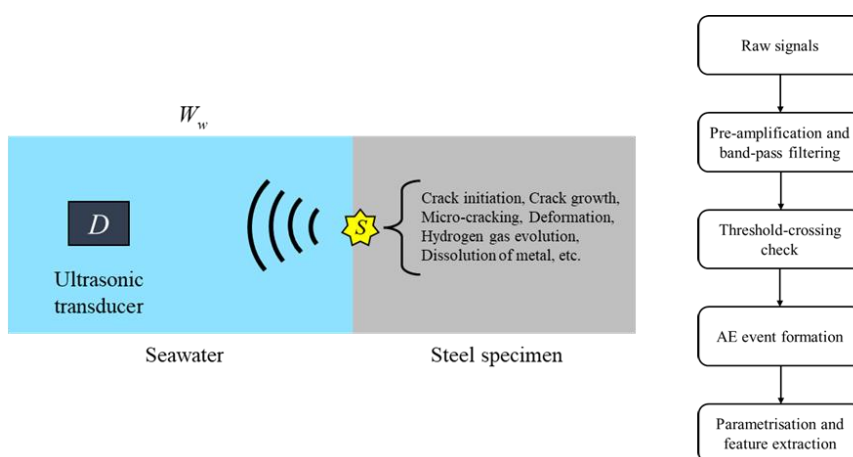


Figure 2.1. Schematic illustration of underwater non-contact AE measurement (left) and signal analysis process (right).

Damage-induced ultrasound waves can propagate in steel media as bulk waves (following longitudinal and shear mode), surface (i.e. Rayleigh) waves, or guided waves, depending on the frequency of the waves and the thickness of the medium [40; 61]. When reaching and propagating through seawater, ultrasound waves

propagate (at a constant speed) as pressure waves. Reflected and transmitted waves are generated at the interface between the two media [62]. The attenuation (of the transmitted) and reflection of ultrasound waves depend on the characteristic acoustic impedance r and speed of sound c in the two media (and the incident angle) [63]. Ultrasound wave components with sufficient energy (to overcome geometrical spreading and material attenuation) can reach the transducer. In the present study, for the corrosion-fatigue damage type of interest, it is feasible to assume that the source signal S is generated by surface defects (Fig. 2.1). In the frequency domain, the measured signal P can be described as the convolution of the source signal S with the propagation (transfer) function of water, W_w , and the transducer transfer function, D , as follows:

$$P = DW_w S + N \quad (2.1)$$

where N refers to the background noise and neglected components of the ultrasound wave, for example reflections from neighbouring surfaces. When N is sufficiently small, the measured damage-induced set of signals may be described as

$$\sum_i P_i = \sum_i DW_w S_{n_i} \quad (2.2)$$

where n is an indicator equal to 1 in the case of a corrosion-induced source ($S_{corrosion-induced}$), and 2 in the case of a corrosion-fatigue-induced source ($S_{corrosion-fatigue-induced}$). If the two source mechanisms are separated, their respective total released energy can be approximated as

$$\begin{aligned}
 E_{n_{total}} &= \sum_i E_{n_i} \\
 &= \sum_i \int (P_{n_i})^2 d\omega \\
 &= \sum_i \int (DW_w S_{n_i})^2 d\omega \\
 &= \sum_i \int (Z S_{n_i})^2 d\omega \\
 &\approx \sum_i \sum_j \Delta\omega Z_j^2 S_{n_{ij}}^2
 \end{aligned} \tag{2.3}$$

where Z denotes the consolidation of propagation transfer functions on the path from the source S to the ultrasonic receiver [64].

2.2.1 ACOUSTIC EMISSION SOURCES DURING CORROSION-FATIGUE

Acoustic emissions during the evolution of corrosion-fatigue damage can be generated by several mechanisms. Typically, resonance-type piezoelectric transducers are used for measuring these signals. For each damage mechanism, the AE source can be described by its specific properties, such as amplitude, count, and energy [42; 45]. Dissolution of metal or breakdown of thin passive film are typically characterised by the lowest AE energy level (proportional to peak amplitude, typically less than 10 μV) [57; 65]. These AE events are considered detectable only by highly sensitive measurement systems. The fracture of thick oxide films is associated with AE with relatively small amplitudes (in the order of 10 μV) [65]. Hydrogen bubble evolution due to hydrogen ion reduction in acid solutions can generate ultrasound signals characterised by higher energy levels and peak amplitudes at approximately 0.1–1 mV [65–66]. A similar energy level characterises slip or twin deformation (in which continuous-type AE are typically observed) [66]. Microcracking mechanisms (e.g. cleavage and/or intergranular cracking and separations) can provide an AE energy level of intermediate magnitude with a peak amplitude on the order of 1–10 mV [36; 66]. The highest AE energy level (above 10

mV) is expected from macrocracking, as a result of the large-scale cleavage or coalescence of microcracks [36; 65-66]. Furthermore, specific AE sources can be related to the fracture or decohesion of precipitates, second-phase particles, and/or non-metallic inclusions in the crack tip plastic zone [51; 65].

2.2.2 MONITORING OF CORROSION-FATIGUE DAMAGE USING NON-CONTACT ACOUSTIC EMISSION

The parameterization of the AE signals was considered in this investigation to extract their main features, as graphically shown (Fig. 2.2). The peak amplitude, energy, and counts were analysed for all the sensors used to investigate the feasibility of detecting and monitoring corrosion-fatigue-induced signals using non-contact AE measurements.

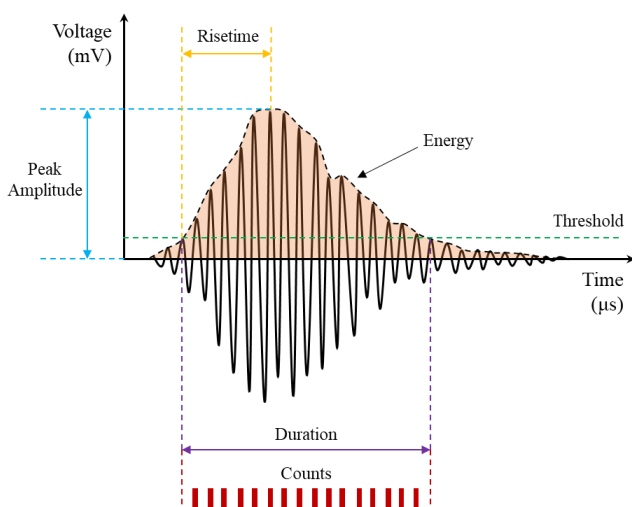


Figure 2.2. Schematic illustration of the AE signal waveform and parameters. *Peak amplitude* is the value of the highest peak of the measured signal (in Voltage), typically expressed in decibels (dB). *Energy* (in eu, and/or V^2s) represents the area measured under the envelope of the recorded signal waveform. *Counts* (an absolute number) is the number of signal amplitude peaks greater than the threshold value.

In this study, variations in peak amplitude, energy, and counts were analysed as a function of load cycles to assess the detectability of corrosion-fatigue-induced ultrasound signals using non-contact AE transducers.

The variation and evolution of the hit rates and cumulative AE parameters (e.g. the number of burst-type signals, energy, and counts) were calculated as functions of the load cycles to assess the evolution of the corrosion-fatigue damage. By evaluating the cumulative trends of AE parameters as a function of time (and/or load cycles), different stages of damage growth can be defined [43-44; 48; 54-55].

The variation of AE burst hit rate (i.e. the rate of burst-type signals per load cycles and/or time unit), energy rate, and count rate throughout the corrosion-fatigue experiment were analysed to monitor active AE sources and provide insights into the various stages of damage growth. Considering the nature of AE signals, every relevant AE event can indicate the onset of new damage, the progression of an active defect, and/or the occurrence of plastic deformations in the material structure. The AE burst hit rate can provide information on the damage growth rate.

The coefficients of variance (CV) of the peak amplitude, energy, and counts were calculated and compared to quantify the parameter performance for the detection and identification of damage. The mean energies of the AE signals were calculated for each stage of damage growth. Analysis of the mean energy can provide valuable insights into the energy characteristics of corrosion- and corrosion-fatigue-induced signals at different stages of damage evolution.

2.3 SMALL-SCALE EXPERIMENTS

Accelerated corrosion-fatigue experiments were conducted on a dog-bone steel specimen to assess the detectability of damage-induced ultrasound signals using non-contact AE transducers. In the context of this feasibility investigation, corrosion and fatigue were simultaneously accelerated at different rates.

2.3.1 EXPERIMENTAL SETUP AND TEST SPECIMEN

A dedicated experimental setup was designed and fabricated to simultaneously apply accelerated corrosion and cyclic loads on a dog-bone steel specimen submerged in artificial seawater. A schematic of the corrosion-fatigue test setup and instrumentation is shown (Fig. 2.3).

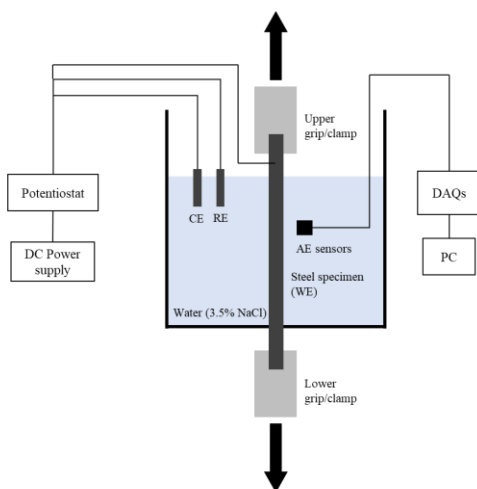


Figure 2.3. Schematic illustration of the corrosion-fatigue test setup and instrumentation. Artificial seawater, i.e. a 3.5 wt-% sodium chloride aqueous solution was used as electrolyte.

A corrosion-fatigue cell was fabricated (Fig. 2.4) and an aluminium support frame (Fig. 2.5a) was used to accommodate the 630x630x630mm³ Plexiglas tank between the two grips of the mechanical testing machine.

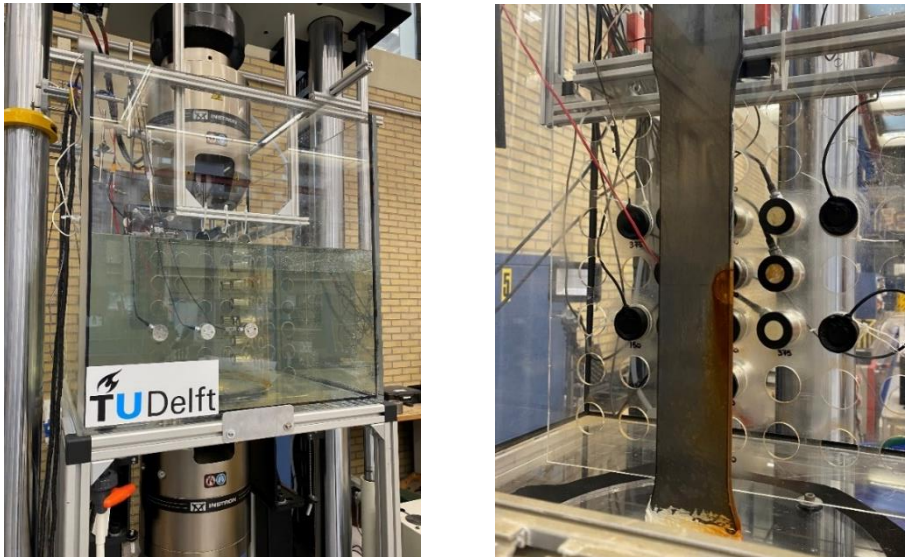


Figure 2.4. The corrosion-fatigue cell located between the two grips of a bi-axial Instron fatigue testing machine (left) and pre-corroded steel specimen (right).

A circular hole was created at the centre of the bottom of the tank (Fig. 2.5b) with a dedicated sealing mechanism around the connector disk. A cutout was realised in the centre of the connector disk with the same dimensions as the shoulder of the steel specimen for installation. The connector disk was bolted to the bottom of the tank using six bolted connections (Fig. 2.5c). Sealed coupling between the specimen and the disk was achieved using a thick layer of elastic glue. The design (Fig. 2.5d) ensured a watertight connection between the steel specimen submerged in artificial seawater and the lower clamp of the fatigue testing machine.

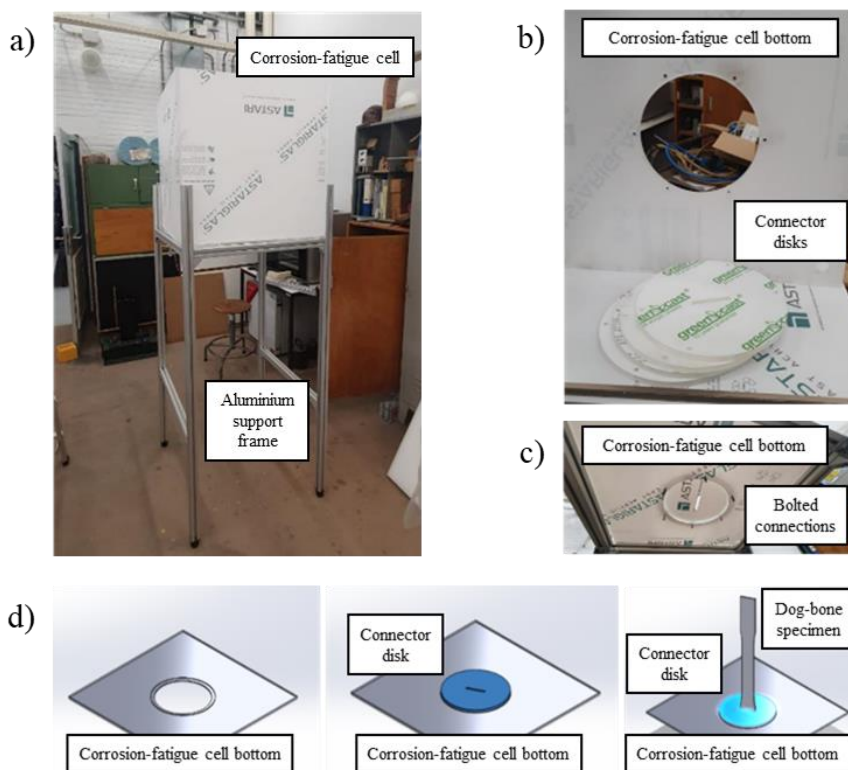


Figure 2.5. (a) Preparation of the corrosion-fatigue cell and aluminium support frame; (b-c) preparation of sealing mechanism; (d) schematic of the seal design.

A schematic of the dog-bone steel specimen is shown (Fig. 2.6). The chosen material for the dog-bone specimen, that is, S420NL, was characterised by a yield stress of 420 N/mm², a tensile strength of 480–620 N/mm², and an elongation of 20%. The mechanical properties of the selected material were in the range of those characteristic of the R3 steel grade (a typical steel grade for offshore support structures, e.g. mooring chains [73]). The specimen was designed according to ASTM E8/E8M standards [67]. The damage-induced AE signals are directly transmitted into the surrounding seawater, where they propagate towards the sensors. In the frequency range considered in this study (~150 kHz), the dominant factor governing the reduction in signal amplitude is geometric spreading, rather than

dissipative losses. For this reason, the geometry of the test sample is expected to have no notable influence on the conclusions. The general trends of the AE measurements could also hold for other underwater steel structures; however, further investigation will be needed to extend the detailed insights and correlations of this study.

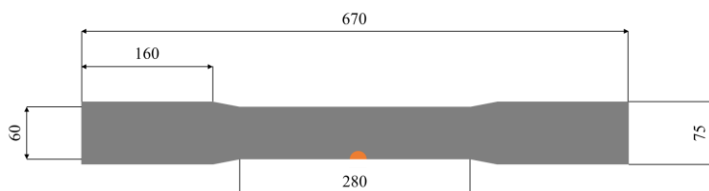


Figure 2.6. Schematic representation of the dog-bone steel specimen (dimensions in mm). The thickness of the specimen is 8 mm.

The dog-bone steel specimen was prepared before the test to induce corrosion-fatigue damage in a constrained area of the steel specimen. This area is a half-circle (2 cm of diameter) exposed surface located at the edge of the width of the specimen, in line with the centre of the gauge area and extended in the width and thickness directions (Fig. 2.4 and Fig. 2.6).

2.3.2 ACCELERATED CORROSION-FATIGUE PROCESS

A three-electrode electrochemical configuration under potentiostatic control was used to accelerate corrosion. The exposed surface of the dog-bone working electrode steel specimen and a graphene bar as counter electrode were submerged in artificial seawater, i.e. a 3.5 wt-% sodium chloride aqueous solution. Artificial seawater was selected as it provides a reproducible and controlled electrolyte. Minor differences may exist between natural and artificial seawater conditions due to the absence (in the latter) of organic matter, microorganisms, and site-specific trace elements that are present in natural seawater, which could, in practice, influence localised corrosion mechanisms. Nevertheless, for comparative laboratory testing, artificial

seawater is generally considered a reasonable and accepted alternative to real seawater. A reference silver/silver chloride electrode (Ag/AgCl) with a stable and well-known potential completed the three-electrode system, allowing the potentiostatic control of the steel specimen with respect to the reference electrode. A fixed potential, equal to $-0.435 \text{ V}_{\text{Ag/AgCl}}$, was imposed allowing to measure the current between the counter and the working electrode. A schematic diagram of the three-electrode system is shown (Fig. 2.7).

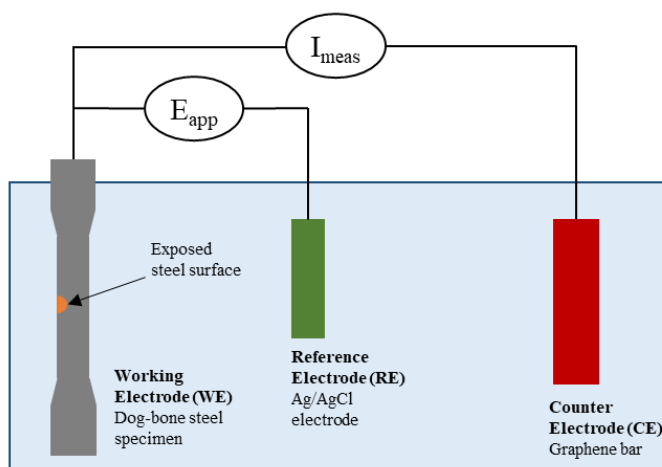


Figure 2.7. Schematic illustration of the three-electrode system.

Uniaxial fatigue loading was applied using an Instron axial-torsion servo-hydraulic testing machine (Fig. 2.4). The specimen was subjected to a sinusoidal cyclic loading regime with a maximum peak load $F_{max} = 168 \text{ kN}$ ($\sigma_{max} = 350 \text{ MPa}$), a load ratio $R = 0.18$, and a loading frequency of 2 Hz. The tested coupon was subjected to an accelerated corrosion process for 100 h before the start of the accelerated corrosion-fatigue test. This process aims to simulate the initiation of surface defects and is referred to as ‘pre-corrosion’. After the pre-corrosion process, accelerated corrosion (i.e. no cyclic load applied to the specimen) was alternated with accelerated corrosion-fatigue. A total of approximately 140 h of accelerated corrosion was

reached by the end of the experiment. A total of approximately 270000 load cycles was performed during the corrosion-fatigue test. A schematic of the testing conditions is shown (Fig. 2.8).

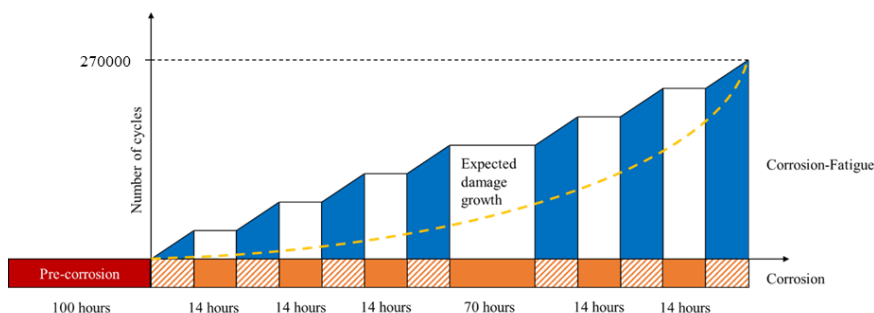


Figure 2.8. Diagram of the testing conditions. Pre-corrosion process is indicated by the red solid fill. Accelerated corrosion (orange solid fill) is alternated with accelerated corrosion-fatigue (blue solid fill and orange diagonal stripes).

In order to estimate the contribution of fatigue and corrosion in the AE measurements, two situations are investigated: (i) corrosion-fatigue (i.e. the combined effect of corrosion and cyclic loading [6]) and (ii) corrosion-only. The difference between the two situations is believed to provide insights into the contribution of fatigue.

2.3.3 ACOUSTIC EMISSION MEASUREMENTS

To collect and record the ultrasound signals generated during the corrosion-fatigue process, an AMSY-6 Vallen data acquisition (DAQ) system and five watertight piezoelectric AE transducers (VS150-WICV01, with integrated preamplifier having a gain of 34 dB) were used. Piezoelectric AE sensors were connected to the DAQs using watertight coaxial cables. A schematic of the sensor layout during the corrosion-fatigue test is shown (Fig. 2.9). The sensors were placed at a fixed distance from the specimen (7 cm) and held in position by a sensor holder (400x400mm² acrylic plate with a 7x7 grid of holes 5 cm equispaced). The fixed distance between

the sensor holder and the specimen was measured with a laser meter (and confirmed with a tape measure) before testing. In practice keeping this distance constant during the measurement is preferable. However, as long as the relative position of the sensors in the measurement array is kept constant, the movement of the measurement array with respect to the specimen only shifts the calculated location of the damage (i.e. timing accuracy and damage activity indices remain unaffected), which can be further corrected by logging this relative position. The sensors were resonant piezoelectric AE transducers with a resonant frequency of 150 kHz and an operating frequency range of 50–450 kHz. The transfer function of the piezoelectric AE transducers can be found in Alkhateeb et al. (2022) [68]. In the proposed experimental setup, seawater is a couplant of ultrasound waves in contactless AE measurements. Removing seawater would require the placement of AE sensors on the specimen surface and using a different coupling medium (e.g. glue), which would change the measurement conditions.

With the expected AE signals in the range of a few hundred kHz and the transfer function of the selected transducers, a conservative sampling rate of 2.5 MHz for recording the ultrasound signal waveforms was selected, to ensure that no possible aliasing would occur. AE parameters, such as the peak amplitude, count, and energy, were extracted from the AE signals to monitor the evolution of the corrosion-fatigue damage.

The proper operation of the AE measurement system was verified before the corrosion-fatigue test by performing pencil lead break (PLB) tests according to ASTM E976-15 standards [69] at different locations on the specimen (e.g. in the area of the exposed surface and outside). The noise level was assessed during the commissioning of the experimental setup. A dummy dog-bone steel specimen submerged in artificial seawater was subjected to cyclic loading (the same conditions as in the reported experiment) for 1 h. The measured noise level is approximately 50 dB.

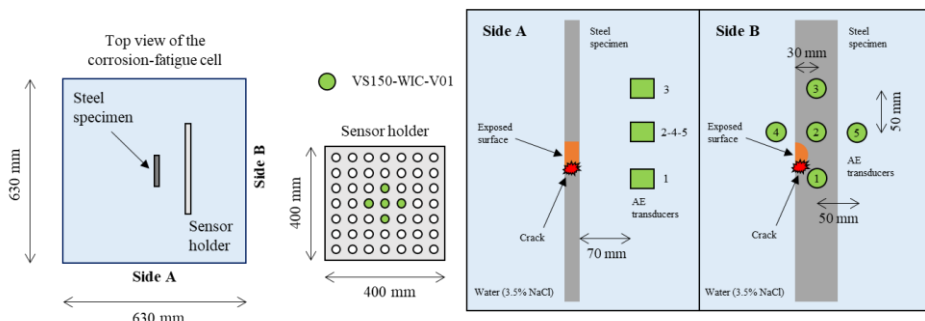


Figure 2.9. Schematic illustration of the AE sensor layout.

The recorded ultrasound signals were pre-processed using a signal-to-noise ratio (SNR) filter of 6 dB to separate burst-type from continuous-type signals. In real-world offshore applications, underwater noise may be expected due to currents, ship propellers, waves, external operations, etc. Nonetheless, these sources are generally characterised by AE signatures with frequencies predominantly below 100 kHz [70-72], whereas corrosion-fatigue-induced AE signals are mostly pronounced in the range of 100–400 kHz.

2.3.4 ATTENUATION DUE TO MARINE GROWTH

Small-scale experiments were conducted to assess the feasibility of measuring AE signals through layers of marine growth. Main highlights about AE signals attenuation due to marine growth are presented in this section. Alkhateeb et al. (2022) [68] present a detailed description of the present study.

Simulated crack experiments were performed using Pencil Lead Breaks (PLBs) on two carbon steel plates, one baseline sample and one covered with artificially fabricated marine growth. The marine growth layer had a thickness of about 15 ± 5 mm, and its composition was based on the DNV-GL definition [73]. It contained mussels, shells, bladder-wrack, and seaweed to represent both soft and hard marine

growth. Epoxy resin was used to bind components to the surface of the specimen (Fig. 2.10).

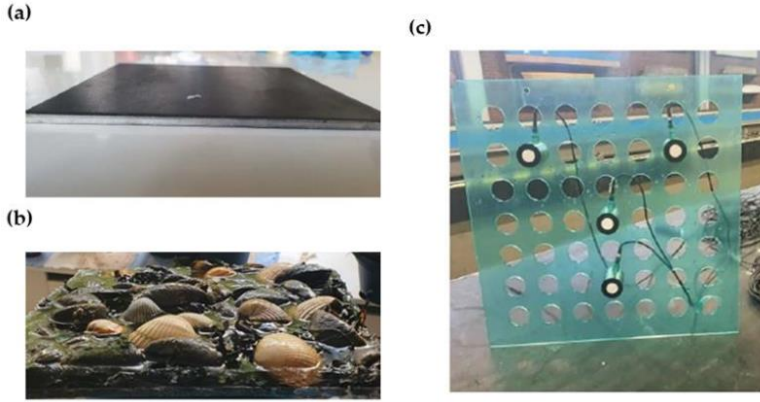


Figure 2.10. Test specimen (a) baseline plate and (b) marine growth covered plate.
(c) Sensor holder with four ultrasound transducers [68].

The PLBs generated signals were measured using 4 underwater non-contact AE transducers placed at a fixed distance (around 50 mm) from the samples. The signals were processed by applying a windowing function and a frequency-domain bandpass (120-380 kHz, typical frequency range of corrosion and crack signals [41-42; 57]) filter to de-noise the signals.

The drop of the maximum signal amplitude was defined as:

$$\text{Amp}_{\text{drop}} = 20 \log_{10} \frac{\max |\text{Amp}_{\text{base}}|}{\max |\text{Amp}_{\text{mg}}|} \quad (2.4)$$

where Amp_{base} and Amp_{mg} refer to the amplitude of recorded signals of the base plate and the marine growth-covered plate, respectively.

2.4 RESULTS AND DISCUSSION

The experiments described (Section 2.3) were performed, and the methodology for the analysis of the ultrasound signals (Section 2.2) was applied. The specimen was subjected to 100 h of pre-corrosion prior to corrosion-fatigue testing. During the corrosion-fatigue process, the specimen was subjected to approximately 270000 load cycles until failure. Approximately 140 h of corrosion were reached by the end of the experiment.

The variation in the analysed AE parameters (i.e. peak amplitude, energy, and counts) as a function of the normalized number of load cycles (for all five sensors) is shown (Fig. 2.11). Four stages of damage growth were identified (A-D, indicated by vertical black dashed lines), as suggested by previous studies [42; 44; 54-55; 74]. Following the prior literature about the detection of different stages of damage growth using AE, the four stages can be referred to as macrocrack initiation (Stage A), growth of macrocrack with different crack growth rates (Stages B and C), and unstable crack growth and fracture (Stage D). The analysis of the measured peak amplitudes from different sensors during the corrosion-fatigue process provides valuable insights into the detectability of corrosion-fatigue damage using non-contact AE. Sensors 1, 2, and 4, which were the closest to the crack location, displayed similar acoustic activity throughout the corrosion-fatigue test.

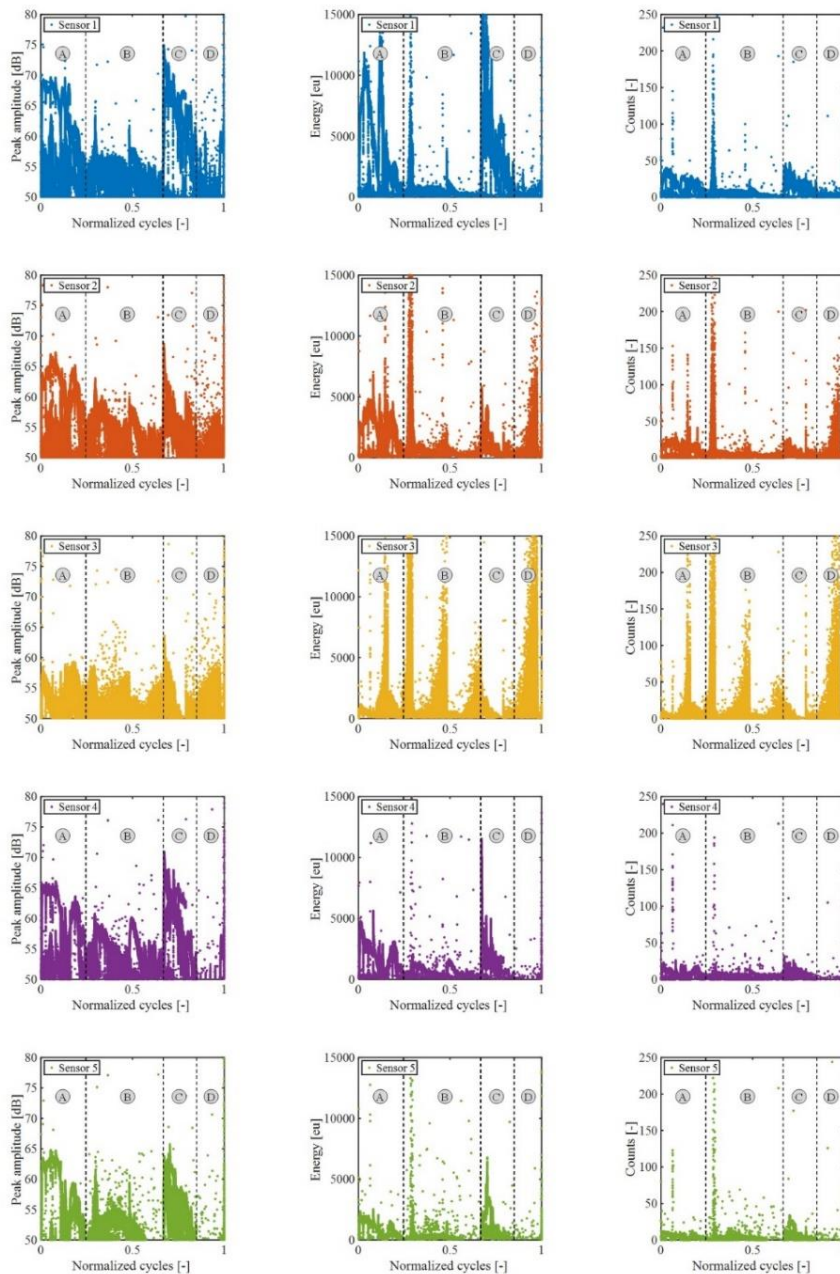


Figure 2.11. Variation of AE parameters as a function of the normalized number of load cycles. Peak amplitude, energy, and counts are shown from left to right for every sensor.

During Stage A, the peak amplitude ranges from 65 dB to 70 dB, indicating significant AE activity as the crack initiated and propagated. In Stage B, the amplitude decreases to 55–60 dB. At this stage, sensors 1 and 2 exhibited occasional jumps up to 65 dB, suggesting localised bursts of acoustic activity. This phenomenon is expected to have no adverse effect on the damage detection process. In fact, given the high SNR of these signals, they could serve as early indications of damage (after AE source localisation). Throughout Stage C, the peak amplitudes range from 55 dB to 75 dB. In Stage D, the amplitude ranges from 55 dB to 60 dB. Peak amplitudes up to 80 dB were recorded at the final failure of the specimen. Sensor 3 exhibited less variation in the peak amplitude throughout the test duration. The measured activity fluctuated within a range of 50–60 dB. During Stage D, which was close to the final failure stage, a distinct increase in peak amplitude was recorded. This trend was also evident in the activity measured using sensor 2. The increase in acoustic activity measured by sensors 2 and 3 during the critical stage (i.e. stage D) seems to detect the approaching failure. Sensor 5, located furthest from the crack location, recorded the lowest AE activity among all sensors. Despite the lower activity (compared to the other sensors), the measured peak amplitude still seems to follow the overall variations exhibited by sensors 1, 2, and 4. In the considered frequency range, geometric spreading is the leading factor influencing signal amplitude attenuation. Considering the background noise floor (i.e. 50 dB), the measurement results can be expected to hold up to 1 m from the specimen. The analysis of the energy levels recorded by different sensors highlights the relevant trends in energy variations throughout the corrosion-fatigue test. Sensor 1 exhibited the highest energy levels among all sensors. Throughout the test, substantial variations in energy were recorded. During Stage A, bursts up to 1.5×10^4 eu ($1 \text{ eu} = 1 \text{ mV}^2 \cdot \text{ms}$ [84]) are observed, suggesting intense AE activity during damage initiation and propagation. In Stage B, the energy level remains below 0.5×10^4 eu, except for two instances already captured by the peak amplitude analysis. The activity of sensor 2 was similar to that of sensor 1. However, an observation was made during Stage D,

close to the specimen failure. Sensor 2 showed increasing energy levels, possibly indicating AE activity leading to the impending failure of the specimen. Although sensor 3 recorded activity relatively similar to that of the other sensors, notable differences were observed. Sensor 3 captures 4–5 highly energetic bursts that were not highlighted by the behaviour of the peak amplitude. Additionally, sensor 3 showed a clear increasing trend in energy during Stage D, similar to sensor 2, indicating the potential importance of AE energy analysis in detecting approaching failure. Sensors 4 and 5 exhibit similar variations in AE energy. Sensor 5, which was furthest from the damage location, displayed the lowest energy levels (consistent with the measured peak amplitude). Despite the lower energy levels, the variations in energy captured by this sensor resembled those observed by other transducers, indicating its sensitivity in detecting AE activity. Although sensor placement seems to influence the measured energy levels, with sensors closer to the crack location generally detecting higher energy levels, the analysis of AE energy highlights the importance of this parameter in detecting active sources of AE signals, especially during the critical stages leading to specimen failure. The analysis of AE counts for damage detection during the corrosion-fatigue test presents both challenges and promising indications. In general, the AE counts exhibited less pronounced (compared to peak amplitude and energy) variations, remaining below 100 counts. Therefore, it is challenging to detect and identify active damage-induced sources. During the initial stages (A and B) of the test, all the sensors (1–5) record a few bursts of AE activity. Sensors 2 and 3 displayed the most remarkable behaviour in terms of AE counts. Sensor 2 exhibited a notably increasing trend in counts as the specimen failed. This trend is consistent with the observations from the energy and peak amplitude analyses, suggesting the potential of the AE counts to predict imminent failure. The same consideration can be made regarding the activity measured by sensor 3 during Stage D. The limited count variations and low values pose difficulties in identifying the active damage sources. However, sensors 2 and 3 exhibited promising behaviour close to specimen failure. When combined with other

AE parameters such as energy and peak amplitude, AE counts can contribute significantly to the detection of damage.

The variation and evolution of the rates of and cumulative AE parameters (i.e. burst-type signals, energy, and counts) as a function of the normalized number of cycles (for all five sensors) is shown (Fig. 2.12). The four stages of damage growth are labelled from A to D and distinguished by vertical black dashed lines.

Analysis of the AE hit rate obtained from different sensors during the corrosion-fatigue test provided valuable insights into the various stages of damage growth. Sensors 1, 2, and 4 exhibit similar AE hit rates throughout the test. In Stage A, the hit rate ranged from two to four hits per cycle, indicating high acoustic activity during the initiation of crack formation and propagation. Stage B shows a stable hit rate between 1 and 2 hits per cycle, indicating stable damage growth at a low rate. In Stage C, which is characterised by a higher rate of damage growth, the hit rate stabilises at three hits per cycle. In Stage D, differences emerged between the activities of the sensors. Remarkably, the behaviour of sensor 2, which exhibited an increasing trend in the hit rate from 0 to 4 hits per cycle before failure, suggests the occurrence of the specimen failure. Sensor 3 showed more variance in the hit rate measurements, making it challenging to distinguish between stages of damage growth. However, as with sensor 2, it shows a similar increasing AE hit rate (from 0 to 4.5 hits per cycle) when approaching final failure in Stage D. Sensor 5, which is the furthest from the damage location, recorded the lowest level of acoustic activity. Nonetheless, it still resembled the trend of AE activity with the most active sensors.

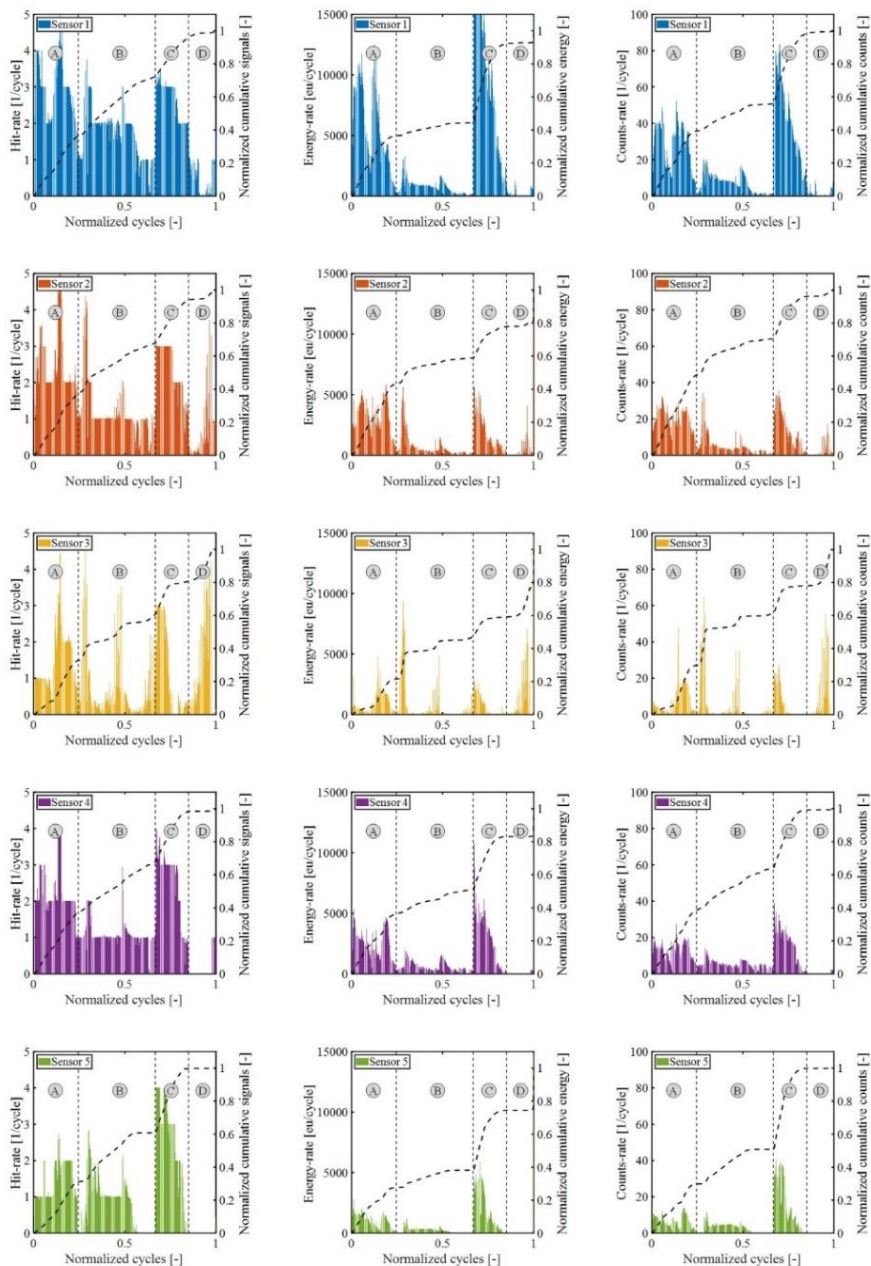


Figure 2.12. Variation and evolution of rate and cumulative AE parameters as a function of the normalized number of load cycles. Hits, energy, and counts are shown from left to right for every sensor.

The cumulative number of AE signals provides clear distinctions between the different stages of damage growth. The slope of the cumulative signals is related to the AE hit rate and indicates how rapidly the damage grows. In Stage A, the slopes of the cumulative signals were relatively high during the initiation of crack formation and propagation. It decreased during Stage B because of the low rate of damage growth. In Stage C, the slope of the cumulative number of signals increases, possibly indicating a higher rate of damage growth. Stage D is characterised by a very low initial slope that increases close to failure, as observed in sensors 2 and 3. Fluctuations in the AE hit rate caused by bursts of acoustic activity were smoothened in the cumulative number of AE signals, providing a more stable representation of damage progression.

The analysis of the energy rates and cumulative energy levels during the corrosion-fatigue test also provided valuable indications of the stages of damage growth. Sensor 1 was the most active in terms of energy rate, followed by sensors 2, 4, and 3. Despite the varying energy rates among the sensors, an important consistent trend was observed. Stage A and C exhibited energy rate levels that were one order of magnitude higher than those in stages B and D. This indicates highly energetic activities during crack initiation and formation in Stage A and rapid damage growth in Stage C. Sensors 2 and 3 show a similar pattern, displaying an increasing trend in energy rate during Stage D. This signifies an escalation not only in the number of AE hits but also in the level of energy associated with each hit as it approaches final failure.

The cumulative energy also seems to add relevant information to the cumulative number of AE signals for identifying the damage growth stages. This is evident from the larger changes in the curve slopes. Stage B, characterised by low slope values, can be clearly distinguished from Stage A and C, which display steeper slopes, representing higher energy accumulation during these stages. Stage D shows a

unique pattern of cumulative energy. It starts with an almost zero slope; however, as observed in sensor 3, the slope increases drastically close to failure.

An analysis of the AE count rate obtained from various sensors during the corrosion-fatigue test is also reported. Throughout the test, the count rate remained consistently below 100 counts/cycle. Although the count rates show limited variation, stage C exhibits the highest count rate, followed by stages A, B, and D. The count rates obtained from sensors 2 and 3 increased steadily in Stage D (Fig. 2.11 and Fig. 2.12). This consistent trend points towards the approaching critical failure stage.

The cumulative number of counts, whose trends resemble the cumulative energy, appears to be more effective (than the count rate) in distinguishing between different stages of damage growth.

The Coefficient of Variation (CoV) of the peak amplitudes, energies, and counts are calculated and compared to quantify the performance of the parameters considered for the detection and identification of damage. The CoV is a measure of the dispersion of data around the mean and can be calculated by dividing the standard deviation by the mean of the data series. AE parameters with high CoV values are typically preferred for damage detection and identification because they are associated with larger data dispersion. Large data dispersion indicates the presence of different AE source mechanisms [44]. The calculated CoV values of selected AE parameters are listed (Table 2.1). For all considered sensors, the AE energy exhibited the highest CoV value. This suggests that AE energy is the most effective parameter (among the selected parameters) for the detection and identification of damage evolution in the steel specimen. The higher value of CoV displayed by sensor 5 is caused by the lower mean of the AE energy characterising its measurements.

AE parameter	Amplitude	Energy	Counts
Sensor 1	0.99	2.09	1.30
Sensor 2	1.09	2.99	1.85
Sensor 3	1.67	3.74	3.29
Sensor 4	1.01	2.24	1.74
Sensor 5	1.11	4.26	1.99

Table 2.1. Coefficient of Variation (CoV) of the selected AE time domain parameters.

The mean energy of the AE signals was calculated for each stage of damage growth. The mean energies of the corrosion and corrosion-fatigue-induced signals throughout the different stages of damage growth are compared (Fig. 2.13). Decoupling of the corrosion- and corrosion-fatigue-induced signals was done based on the testing conditions and on the assumption that during corrosion-fatigue the degradation of the material was mainly caused by the fatigue process. Analysis of the mean energy at different stages of the test provided valuable insights into the energy characteristics of corrosion- and corrosion-fatigue-induced signals during damage evolution. The mean energy of the corrosion-induced signals appeared to be relatively stable and was limited to values below 500 eu. The mean energy of the corrosion-induced signals was approximately one order of magnitude lower than that of the corrosion-fatigue-induced signals. Regarding the corrosion-fatigue-induced signals, in the initial Stage A, mean energy displays relatively high values. As the damage progressed to Stage B, the mean energy decreased. During Stages C and D, the mean energy experienced a drastic increase, reaching magnitudes on the order of 10^5 at the end of the test (because of the final failure of the specimen). Despite the complexity of the corrosion-induced damage mechanisms, based on this result, the corrosion process seems to induce less energy (confirming the considerations in Section 2.2.1) and more stable acoustic activity (possibly indicating a more controlled degradation process). In contrast, the corrosion-fatigue-induced damage

exhibited a more intense and dynamic energy distribution, suggesting a more severe and less consistent material degradation mechanism. Finally, the rapid and substantial increase in the corrosion-fatigue-induced mean energy may be an indication of accelerated material degradation as it approaches the final failure.

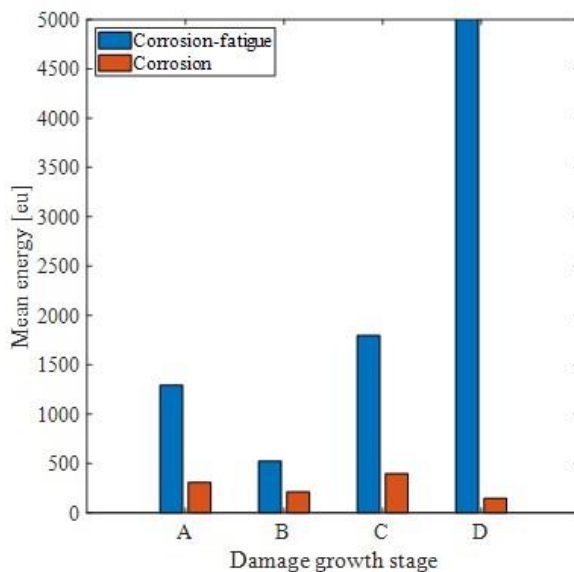


Figure 2.13. Mean energy of corrosion- and corrosion-fatigue-induced signals during different stages of damage growth.

The relative contributions of the corrosion- and corrosion-fatigue-induced ultrasound signals throughout the experiment are defined as the number of burst-type signals per hour of testing. The relative contributions in the four different stages of damage growth is shown (Fig. 2.14).

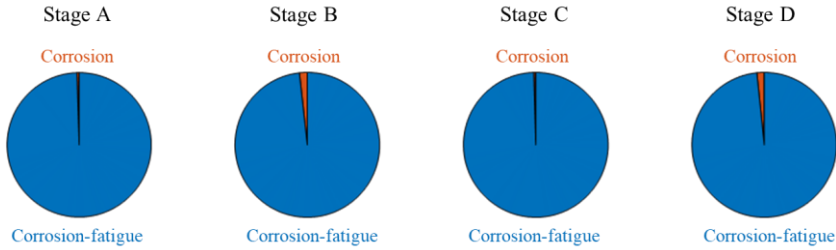


Figure 2.14. Average number of corrosion- and corrosion-fatigue-induced signals per hour of testing

The total numbers of corrosion- and corrosion-fatigue-induced ultrasound signals at different stages of damage growth is shown (Fig. 2.15).

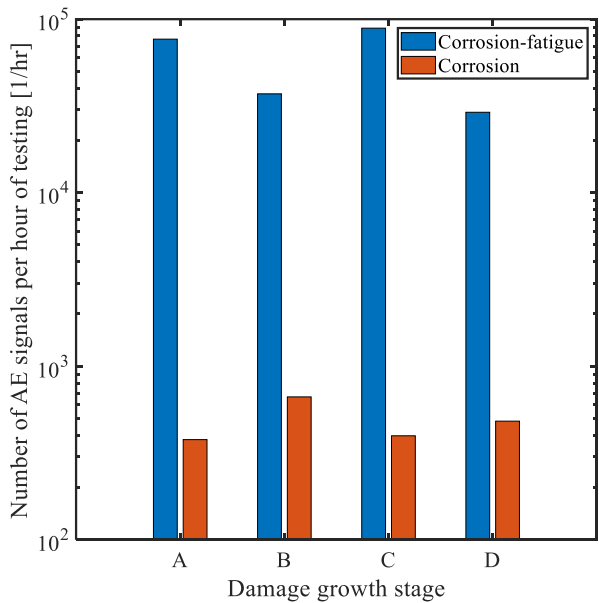


Figure 2.15. Total number of corrosion- and corrosion-fatigue-induced signals per hour of testing during different stages of damage growth.

Combined with the previous insights (Fig. 2.14), it can be inferred that the contribution of the corrosion-induced signals did not exceed 2% of the total number

of measured signals (per hour of testing). During stages A and C, the corrosion-induced signals were limited to 1% of the total number of signals. In stages A and C, 378 and 397 corrosion-induced signals were detected, respectively, while 76717 and 88745 corrosion-fatigue-induced AE signals were observed. Stages B and D showed the highest relative contribution of corrosion-induced signals, at 2% of the total measured signals. A total of 666 and 483 corrosion-induced signals were measured, against 37132 and 29073 corrosion-fatigue-induced AE signals during stages B and D, respectively. Although in the proposed experimental set-up, the corrosion mechanism seems to induce a lower number of ultrasound signals (at a lower energy level) than the corrosion-fatigue mechanism, it can be concluded that corrosion-induced signals can be detected throughout the evolution of the corrosion-fatigue damage.

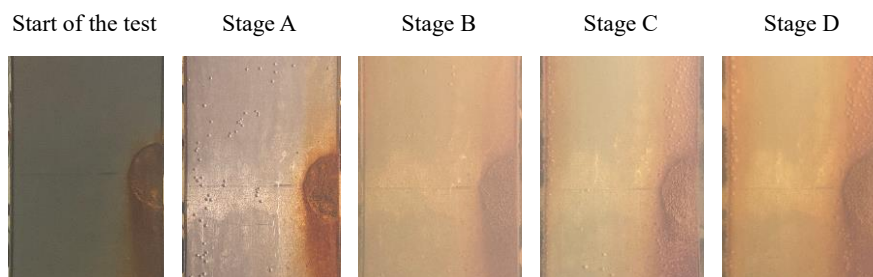


Figure 2.16. Exposed surface condition during different stages of the experiment.

The condition of the exposed surface during the test is shown (Fig. 2.16). At the start of the test, after the pre-corrosion process, the exposed surface shows uniform corrosion and a thin oxide layer. In Stage A, corrosion appears more uniform, and bubbles form on the specimen surface. In Stage B, fewer bubbles are visible, and the surface continues to show uniform corrosion. A thicker oxide layer forms and the water becomes turbid due to the release of iron ions into the solution. In Stage C, bubbles appear on the edges of the specimen along with corrosion activity. This likely occurred after part of the coating layer detached from the specimen surface. The exposed surface shows a thicker oxide layer. In stage D, fewer but larger bubbles

are present. The oxide layer is thicker and more uniform, and water turbidity increases. Both the mean energy (Fig. 2.13) and the number of signals (Fig. 2.15) exhibit limited fluctuations in corrosion-induced acoustic activity, suggesting a stable degradation process. This is further supported by the consistent growth of the oxide layer on the exposed surface. Additionally, the continuous increase in water turbidity suggests an ongoing corrosion process. The appearance of bubbles and the coating layer detachment may influence the corrosion dynamics. These factors can be expected to be sources of the fluctuations in the corrosion-induced AE activity.

2.4.1 RESULTS OF THE ARTIFICIAL MARINE GROWTH ATTENUATION STUDY

The drop of the maximum signal amplitude in the time domain differed between the four sensors, as shown in Table 2.2.

	Sensor 1	Sensor 2	Sensor 3	Sensor 4
Maximum amplitude (mV)	7.7	21.2	25.2	22.6
Baseplate				
Maximum amplitude (mV)				
Marine growth covered plate	3.6	5.6	8.7	3.4
Amplitude drop (%)	53.2	73.6	65.5	85.0
Amplitude drop (dB)	6.6	11.6	9.2	16.5

Table 2.2. Maximum amplitude of measured signals and amplitude drop between baseplate and marine growth covered plate experiment.

The average amplitude drop is about 12.4 dB (considering channels 2–4). The drop in signal amplitude can be considered promising and expected to be measurable in realistic conditions. The non-homogeneous marine growth layer can explain the difference in amplitude drop. The different dimensions and types of shells may affect the ultrasound wave propagating in different directions. The sensors were placed at different distances and angles from the AE source to account for such irregularities.

The variation in the amplitude drop is expected to be mainly due to the details of the positioning of hard shells on each wave propagation path. Given the relatively high volume fraction of hard shells in this mixture, the measured attenuation is expected to be representative of an extreme case. Establishing further correlation between marine growth shapes and dimensions with the amplitude drop was outside the scope of this work, and these variations always exist in practice. In this study, both hard and soft growth types were present, providing a combined effect that intends to capture the range of possible interactions with the propagating ultrasound waves.

2.5 CONCLUSION

Small-scale corrosion-fatigue experiments were conducted on a dog-bone steel specimen to assess the detectability of corrosion-fatigue damage using non-contact AE. Corrosion-fatigue was successfully induced using the proposed experimental setup, and damage-induced ultrasound signals were detected with a satisfactory signal-to-noise ratio using non-contact AE sensors (in the frequency range of 50–450 kHz). The trends in the AE parameters over the load cycles revealed four stages of damage evolution (from A to D). The cumulative number of AE signals shows clear distinctions between the stages, smoothing fluctuations in the rates and providing a more stable representation of damage progression. The energy rate trends suggest highly energetic activity during crack formation and rapid growth in stages A and C, respectively. Among the considered parameters, the AE energy exhibited the highest variability, making it an effective indicator of the damage evolution in the specimen. A comparison of mean energy levels throughout the experiment differentiated corrosion- and corrosion-fatigue-induced signals, with the latter exhibiting a mean energy approximately one order of magnitude higher than that of the former. In the proposed experiment, it appeared that the corrosion mechanism induced a significantly lower number of ultrasound signals than corrosion-fatigue; however, it was possible to detect corrosion-induced signals throughout the entire damage evolution.

The observations from simulated crack signals on two steel plates (with and without marine growth) indicate that the ultrasound waves can penetrate the marine growth (artificially-fabricated) and can be successfully detected using non-contact AE transducers in submerged conditions. A maximum 12dB drop in signal amplitude can be expected in time-domain due to artificially-made marine growth.

Acoustic Emission-based digital twin for diagnosis of corrosion-fatigue damage in submerged mooring chains

This chapter is based on the journal article and the conference article:

F. Riccioli, Ø. Gabrielsen, I.S. Høgsæt, P.S. Barros, and L. Pahlavan, “Corrosion-fatigue damage identification in submerged mooring chain links using remote acoustic emission monitoring,” *Marine Structures*, vol. 98, p. 103685, Aug. 2024, doi: 10.1016/j.marstruc.2024.103685.

F. Riccioli, A. Tyto, and L. Pahlavan, “Non-contact acoustic emission monitoring of corrosion in mooring chain links,” in *Proceedings of Structural Health Monitoring 2024*, Sep. 2024.

3 ACOUSTIC EMISSION-BASED DIGITAL TWIN FOR DIAGNOSIS OF CORROSION-FATIGUE DAMAGE IN SUBMERGED MOORING CHAINS

3.1 INTRODUCTION

Despite the promising results in corrosion-fatigue damage detection and monitoring using AE, only a few large-scale testing attempts have been made using mooring chains. Rivera et al. [58] conducted a long-term (4-month) chain tensile test to assess the feasibility of monitoring crack initiation and growth in mooring chain links in artificial seawater using the AE technique. The authors identified the cumulative hits (i.e. cumulative number of AE signals measured throughout the test [36]) as one of the most promising AE parameters for continuous monitoring of damage initiation and propagation in mooring chain links. Angulo et al. [59] performed a 72-day large-scale fatigue experiment to assess the capabilities of AE as a monitoring tool to detect crack initiation and propagation in mooring chains under realistic loading and environmental conditions. The authors pointed out the frequency content of the ultrasound signals as the most promising parameter to detect growing damage in the chain links. An increase in the average frequency (i.e. ratio between signal counts and duration [36]) was observed with the growth of the crack in the chain link. However, the difficult environment and the high level of noise recorded during the experiment represented a challenge for a full and comprehensive analysis of the measurements. Limited investigations on the detection and monitoring of ultrasound signals using non-contact AE technique have also been reported in the literature, see for example [75-78].

This chapter presents the feasibility of constructing an AE-based DT through detection, localisation, and monitoring corrosion-fatigue and corrosion damage in full-scale mooring chain links using underwater non-contact AE measurements.

Large-scale corrosion-fatigue (and corrosion only) experiments have been conducted on mooring chains retrieved after operation offshore. Ultrasound signals have been measured using arrays of AE transducers facing the chains from two specific perpendicular planes (front and side). The AE parameters extracted from the measured signals have been analysed throughout the tests. A 3D source localisation algorithm for the damage-induced ultrasound signals has been implemented.

3.2 DETECTION AND LOCALISATION OF CORROSION-FATIGUE USING NON-CONTACT ACOUSTIC EMISSION

The methodology of AE monitoring in this investigation comprises parametrisation of AE signals as well as localisation of AE sources as described below.

3.2.1 ACOUSTIC EMISSION MONITORING OF CORROSION-FATIGUE

Acoustic emission monitoring of fatigue

Parametrisation of the AE signals [36; 42] is used in this study to monitor the acoustic activity induced by the initiation and growth of fatigue damage. Damage-induced ultrasound signals have been continuously recorded using a vertical array of four AE transducers (deployed over the length of the chain segment) throughout the test. The analysis covers 100 h of measurements sampled uniformly throughout the test. The total number of AE signals, the cumulative number of AE signals, and the AE hit rate (defined as the number of burst-type signals [79-80] per loading cycle) have been analysed over the test duration. The total number of AE signals provides insights into the most active areas along the chain segment. The analysis of the cumulative number of AE signals over the test duration enables the assessment of the evolution of the damage-induced signals throughout the test. A relatively steep curve of the cumulative number of signals may be expected during crack initiation and stable growth. Besides that, the AE hit rate is employed to identify active damage zones. Every AE event can indicate the onset of new damage or the progression of

an existing active defect in the material. The variation of the AE hit rate during the test provides insights into the damage growth rate (i.e. crack growth rate).

Acoustic emission monitoring of corrosion

Parametric analysis of the AE signals [36] is used to investigate the feasibility of detecting and monitoring corrosion damage in mooring chain links using non-contact AE measurements. Damage-induced ultrasound signals have been continuously recorded using two perpendicular arrays of AE transducers throughout the test. The analysis covers the entire duration of the test. The total number of recorded AE signals is calculated for each sensor in the perpendicular arrays of AE transducers. The total number of AE signals can provide insights into the most active areas on the chain surface. The cumulative number of AE signals and the AE hit-rate are calculated as a function of testing time to assess the evolution of the corrosion damage. Considering the nature of the AE signals, every relevant AE event can indicate the onset of a new damage zone, the growth of an active corrosion pit, and/or the occurrence of secondary corrosion-induced degradation processes. The evolution of the cumulative number of AE signals can provide information about the evolution of the corrosion damage. The AE burst hit-rate can provide indications of the damage growth rate (i.e. corrosion rate).

3.2.2 DIGITAL TWIN AND AE SOURCE LOCALISATION

A diagnostic DT is constructed based on AE data to identify the location of damage in mooring chain links. A 3D source localisation algorithm for damage-induced ultrasound signals is implemented, and the localisation results mapped onto the 3D geometry of the mooring chain segment for representation of the DT.

The AE source localisation approach in this study utilises the principle of triangulation [81]. In this process, for every AE event, the differential time-of-flight at each sensor is obtained from the waveforms using the Akaike Information Criterion (AIC) [82-83]. A search domain is defined utilizing the surface of the chain

links. Minimising the error between the predicted and measured differential arrival times over the domain is performed to estimate the source location.

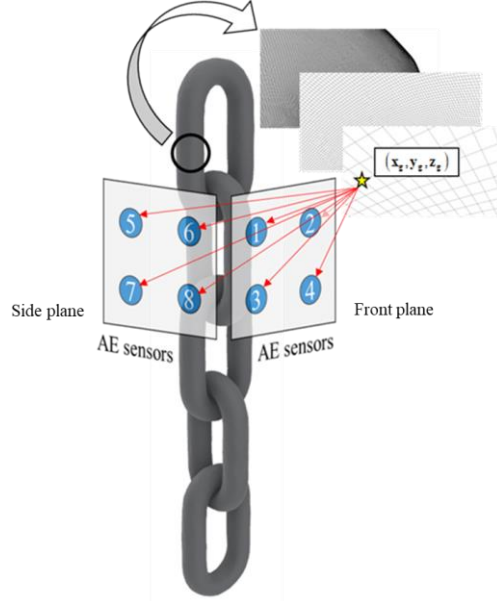


Figure 3.1. Schematic illustration of the sensor holders and the localisation approach. The sensor holders are coupled and move simultaneously.

For an arbitrary point with coordinates \mathbf{x} belonging to the domain Ω defined by the surface of the chain links, the error function, i.e. objective function, is defined as follows:

$$e_k(\mathbf{x}) = \left(\sum_{i=1}^{M_k} \left\| \frac{1}{c_w} (\|\mathbf{x} - \mathbf{x}_i\| - \|\mathbf{x} - \mathbf{x}_r\|) - \tau_i \right\|^2 \right)^{\frac{1}{2}} \quad (3.1)$$

where M_k is the number of sensors participating in the localisation of the k th AE event, \mathbf{x}_i is the vector containing their coordinates and \mathbf{x}_r indicates the coordinates of the (arbitrarily chosen) reference sensor r . c_w denotes the speed of sound in water. τ_i expresses the differential arrival time of the ultrasound signals at sensor i (participating in the recording of the AE event) with respect to the reference sensor.

The most probable location of the source signal \mathbf{x}_k^s can therefore be obtained as:

$$\mathbf{x}_k^s = \arg \min_{\mathbf{x}} e_k(\mathbf{x}) \quad \mathbf{x} \in \Omega \quad (3.2)$$

A maximum allowable error value can be additionally used as a quality criterion to improve the reliability of the source localisation.

For the coupled movable arrays of AE transducers holding the AE transducers on perpendicular planes (Fig. 3.1), participation of a minimum of 3-4 sensors was considered. Once the procedure described above is applied to all AE events, a cumulative normalised inverse error function (ε) is defined for the visualisation of the most probable location of the AE source over the entire measurement period:

$$\varepsilon = \sum_{k=1}^N \alpha_k \beta_k e_k^{-1}(x) \quad (3.3)$$

$$\beta_k = \begin{cases} 0, & \forall e_k > \bar{e}_k \\ 1, & \forall e_k \leq \bar{e}_k \end{cases} \quad (3.4)$$

where N is the total number of localised AE events, and α_k is the normalisation factor limiting the values of $e_k^{-1}(x)$ to $[0,1]$, and β_k is a binary coefficient that selects only the events that satisfy the localisation error threshold.

The scheme described above has been numerically implemented by discretizing the domain Ω . A 3D model of the chain surface obtained with 3D laser scanning has been used for this purpose.

3.3 FULL-SCALE EXPERIMENTS

A 5-link mooring chain segment was subjected to cyclic loading while submerged in artificial seawater to detect and localise damage-induced ultrasound signals using remote AE measurements.

3.3.1 FULL-SCALE FATIGUE TEST

Experimental setup and test specimen

A vertical test rig was used to perform fatigue testing of a 5-link mooring chain retrieved after operation offshore. The chain sample consists of a segment of a studless R4 chain with a nominal diameter of 137 mm and a nominal Minimum Breaking Load (MBL) of 16992 kN. The chain segment was submerged in artificial seawater, i.e. a 3.5 ± 0.1 wt-% sodium chloride aqueous solution, while subjected to cyclic loading. The fatigue test was run in load control. The key parameters for the fatigue experiment are shown (Table 3.1). The vertical test rig was instrumented with non-contact watertight AE transducers to continuously measure damage-induced ultrasound signals during the experiment (Fig. 3.2).

Chain diameter [mm]	137
Chain grade	R4
MBL [kN]	16992
Environment	Artificial seawater (3.5% NaCl)
Middle load [%MBL]	9.4
Load amplitude [%MBL]	4.8
Test frequency [Hz]	0.5

Table 3.1. Test parameters.

Acoustic emission measurements

A vertical array of AE transducers was deployed along the length of the chain sample (Fig. 3.2). The vertical array was placed at a fixed distance from the chain sample and held in position by a combination of sensor holders and carabiners. Two movable arrays of AE transducers were deployed on two perpendicular planes on the front and left sides of the chain sample (Fig. 3.3). The movable arrays of transducers consist of two groups of AE sensors (each at a fixed distance from the chain) with a controllable vertical position. The movable arrays were connected to a separate mechanism to make stops in front of different chain links. Each movable array was

held in position using a sensor holder and two polyester lines (on the sides of the sensor holder) to constrain its rotation around the vertical axis. A centre line (orange rope in Fig. 3.2 and Fig. 3.3) was used to control the vertical position of each sensor holder.

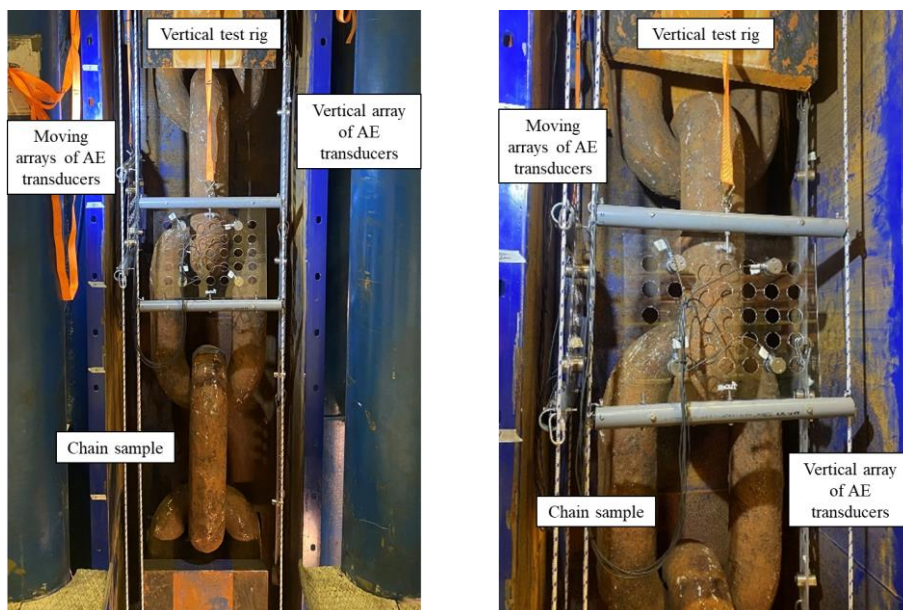


Figure 3.2. Instrumented test rig (left) and non-contact sensors deployment in the test rig (right).

An AMSY-6 Vallen data acquisition (DAQ) system was used to collect and record the damage-induced signals during the experiment. Twelve watertight piezoelectric AE transducers (VS150-WIC-V01, with an integrated preamplifier, gain of 34 dB) were connected to the DAQs using watertight co-axial cables. The AE sensors were resonant piezoelectric transducers with a resonant frequency of 150 kHz and an operating frequency range of 50–450 kHz [58-59; 68]. The transfer function of the transducers can be found in Alkhateeb et al. [68]. The signals were recorded using a sampling rate of 2.5 MHz (with a total sample length of 4096 points). AE signals were continuously measured throughout the entire experiment. The results presented in the study refer to 100 h of AE measurements sampled equally over the test

duration. A schematic illustration of the sensors layout and the positions of the movable arrays of transducers during the experiment is shown (Fig. 3.4).

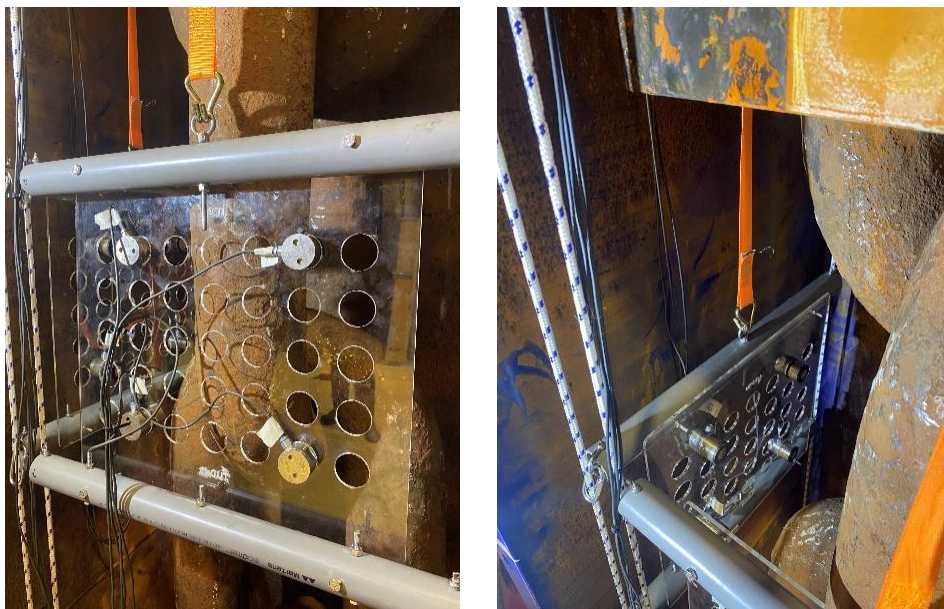


Figure 3.3. Perpendicular movable arrays of AE transducers.

The movements of the two arrays were synchronised and performed manually every 24 h during the experiment. Seven positions were defined before testing (Fig. 3.4). The positions correspond to the 4 link-to-link areas (typically the most susceptible zones to damage in mooring chain links) and 3 flash butt weld regions. The time spent in each position is shown (Table 3.2) as a percentage of the total hours of measurements analysed.

Before the start of the test pencil lead break tests were performed (according to ASTM E976-15 [69]) at different locations on the external side of the closed tank (after filling with artificial seawater) to verify the reproducibility of the AE sensors response in water and proper operation of the AE measurements system.

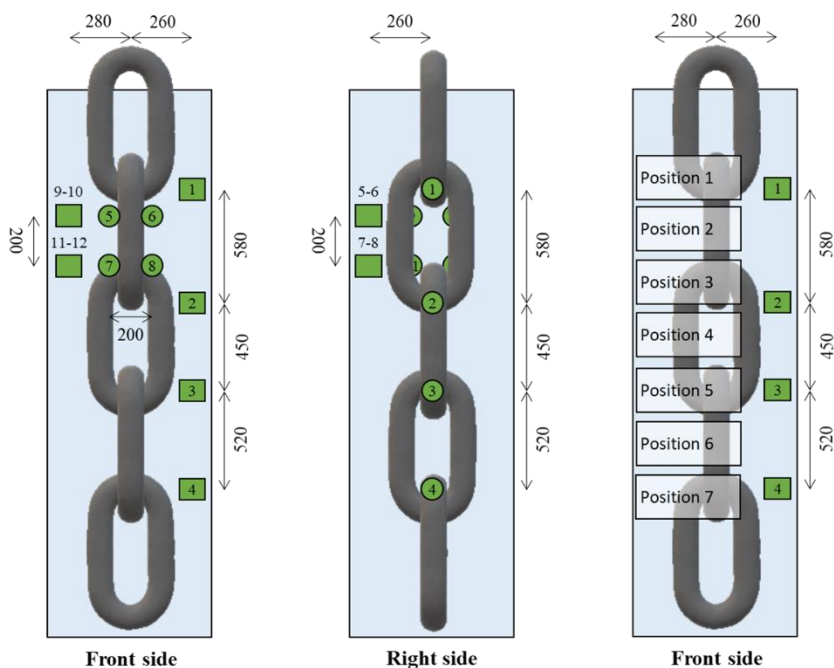


Figure 3.4. Schematic illustration of the AE sensors layout and positions of movable arrays. Dimensions in mm. Green elements schematically indicate sensors numbering and positioning. Transparent rectangles schematically indicate the positions of the movable arrays of sensors.

Position 1	25%
Position 2	11%
Position 3	22%
Position 4	11%
Position 5	18%
Position 6	7%
Position 7	6%

Table 3.2. Measurement time spent in each position by the movable arrays of transducers and used to calculate the AE-based DT. The time is expressed as a percentage of the total hours of measurements analysed.

During the commissioning process, the noise level was assessed. Cyclic loads (using the same loading conditions shown in Table 3.1) were applied to the chain sample submerged in artificial seawater. The measured noise level was about 50 dB. The acquisition threshold was hence set to 60 dB.

The recorded ultrasound signals were pre-processed using a signal-to-noise ratio (SNR) filter of 20 dB to separate potential damage signals from laboratory background noise.

3.3.2 FULL-SCALE CORROSION TEST

Accelerated corrosion experiments have been performed on a large-scale mooring chain sample to assess the feasibility of detecting, localising, and monitoring corrosion damage in large-scale submerged steel structures using non-contact AE transducers.

Experimental setup and test specimen

A dedicated experimental setup was designed and fabricated to apply accelerated corrosion on a large-scale mooring chain sample submerged in natural seawater. A schematic illustration of the setup and equipment is shown (Fig. 3.5, left).

The fabricated test setup includes an aluminium support frame that was used to accommodate the 2-link mooring chain sample in the 1000x1200x1000mm³ glass tank (Fig. 3.5, right). The chain sample was submerged in a natural seawater volume of 1000x1000x1000mm³. The chain sample consists of a segment of a used studless R4 chain with a nominal diameter of 136 mm.

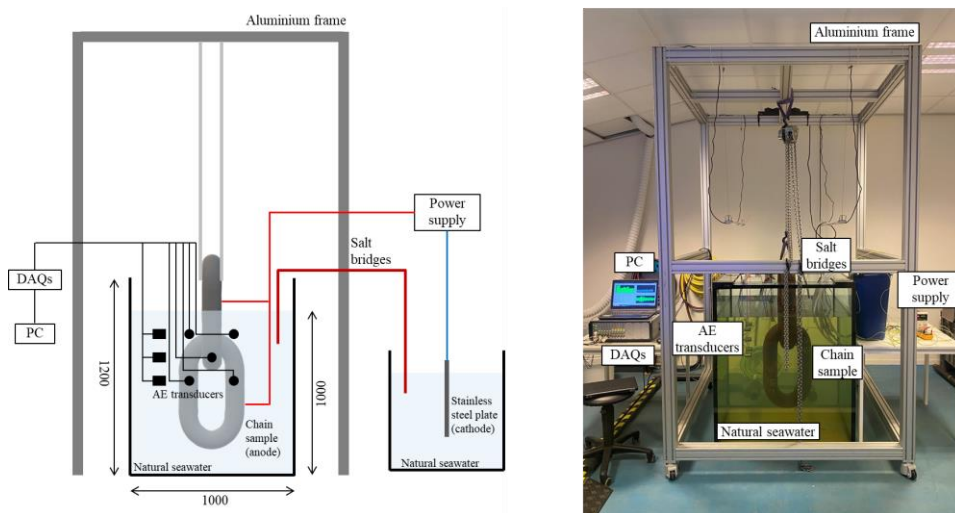


Figure 3.5. Schematic illustration of the large-scale corrosion experimental setup (left), and large-scale corrosion experimental setup with submerged mooring chain sample (right). Dimensions in mm.

Accelerated corrosion process

The corrosion process was accelerated through galvanostatic anodic polarisation. A direct current has been imposed to accelerate the corrosion process with the positive pole connected to the submerged mooring chain sample (i.e. anode) and the negative pole connected to a stainless-steel plate (i.e. cathode). Direct current power supply (i.e. 36 V and 5 A) has been deployed. Both anode and cathode have been submerged in natural seawater to ensure sufficient (and realistic) electrical conductivity. The cathode was positioned in a separate water container to prevent contamination of the main anode water volume by OH^- (hydroxyl) ions produced during cathodic reactions. A total of about 15-20 salt bridges have been placed between the two water volumes. The chain sample was subject to an accelerated corrosion process for about $t = 187$ hours using an anodic current level of $I_a = 0.25$ A.

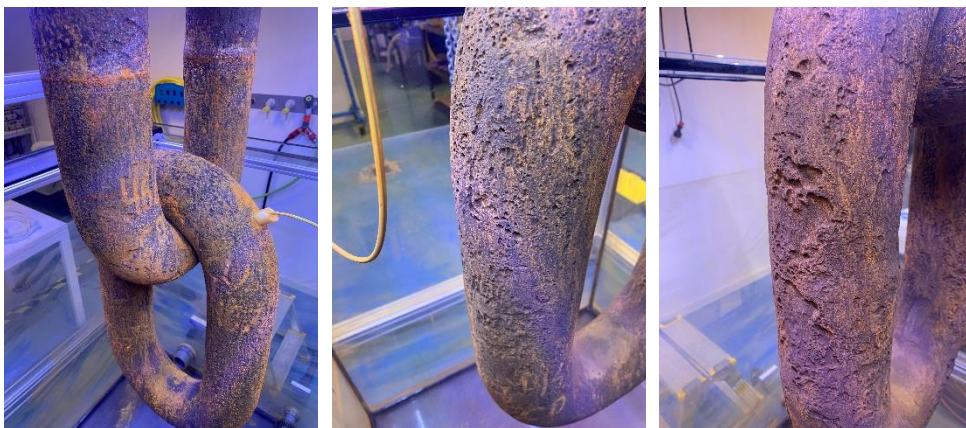


Figure 3.6. Visual assessment of chain surface conditions after accelerated corrosion process.

Acoustic emission measurements

To collect and record the ultrasound signals generated during the corrosion process, an AMSY-6 Vallen data acquisition (DAQ) system and ten watertight piezoelectric AE transducers (VS150-WIC-V01, with an integrated preamplifier, gain of 34 dB) were employed [84]. Watertight co-axial cables connected the piezoelectric AE transducers to the DAQ system. A schematic of the layout of the AE transducers is shown (Fig. 3.7). A fixed distance (equal to 300 mm) was kept between the vertical axis of the chain sample and the two arrays of AE transducers using two sensor holders (400x400mm² acrylic plates with a 7x7 grid of holes 50 mm equally spaced). A sampling rate of 2,5 MHz was used to record the AE signal waveforms (with a total sample length of 4.096 points).

Pencil lead break tests (according to ASTM E976-15 [69]) on the submerged surface of the chain links were performed to check the proper functioning of the AE measurement system and to verify the localisation algorithm before testing.

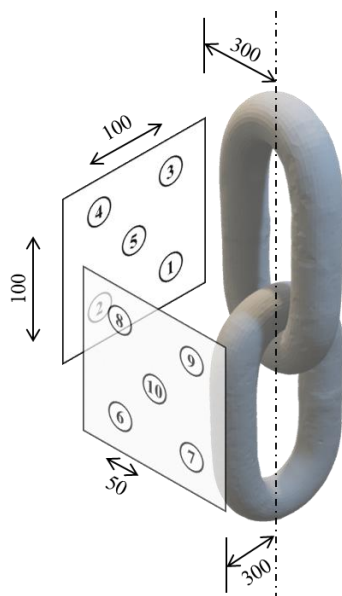


Figure 3.7. Schematic illustration of the layout of the AE transducers. Group 1 includes sensors 1-5. Group 2 includes sensors 6-10. Dimensions in mm.

The maximum measured noise level in the laboratory was about 27 dB. The acquisition threshold was set to 30 dB. The recorded ultrasound signals have been pre-processed using a signal-to-noise ratio filter of 20 dB.

3.4 RESULTS AND DISCUSSION

3.4.1 DETECTION AND LOCALISATION OF FATIGUE

Experiments described (Section 3.3.1) were performed and the methodology for the analysis of the ultrasound signals (Section 3.2) was applied. The present analysis includes ultrasound signals recorded during 100 h of testing. To ensure even distribution, the measurement hours were chosen to span the entire duration of the experiment.

Detection and monitoring of fatigue

Parametrisation of the AE measurements provides general insights into the acoustic activity recorded in the test rig throughout the test. The vertical array of four AE transducers is used to detect and monitor possible damage zones along the chain segment.

The total number of AE signals (Fig. 3.8a) and the cumulative number of AE signals recorded by the vertical array of transducers (Fig. 3.8b) along with the normalised vertical displacement throughout the test are shown (Fig. 3.8).

The total number of AE signals indicates sensor 1 as the most active in the vertical array pointing out Link 1–2 as the most active area in the test rig. This can be due to the combination of main damage-induced ultrasound signals with noise signals from the upper clamp of the test rig. On the other hand, the latter is expected to be limited by the SNR-based filter used in the pre-processing of the data. The acoustic activity decays toward the bottom of the test rig. Sensor 4 displays slightly increased activity (compared to sensor 3), possibly due to an increased noise level generated during the test by sources such as the clamp and the water inlet at the bottom of the test rig. These noise signals will be filtered out in a later stage by using the localisation of AE sources.

The cumulative number of AE signals shows a clear distinction between the activity in the top part of the chain segment and the mid-lower one. The slope of the cumulative trend is represented by the AE hit rate (Fig. 3.9). Note that in previous research, the correlation between crack growth and AE hit rate has been demonstrated [85-86] and the slope of cumulative AE parameters has been used to identify different crack growth stages [42-47].

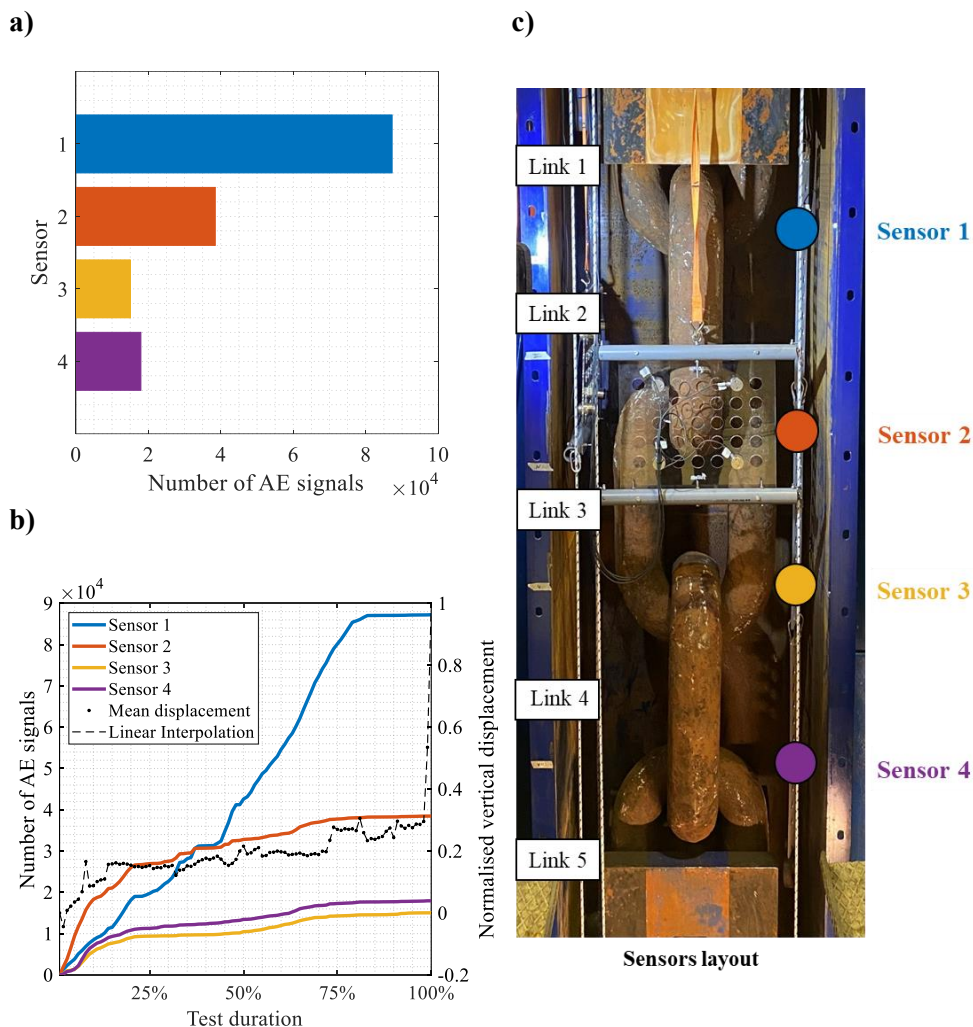


Figure 3.8. (a) Total number of AE signals and (b) cumulative number of AE signals measured by the vertical arrays of transducers and normalised vertical displacement throughout the test. (c) Layout of the vertical array of transducers.

Sensor 1 displays a relatively steep curve throughout the experiment. In particular, two slopes can be observed. First from 0 % to 35 %, and second from 45 % to 85 % of the test duration. This could indicate a corrosion-fatigue damage growth at two different rates between 0-35 % and 45–85 %, respectively. During the latest stage of the test, a characteristic AE quiescence is observed. Besides that, sensors 2–4 show

relatively similar trends that differ from the one followed by sensor 1. The cumulative number of signals measured by sensors 2–4 undergoes a steep increase between 0 and 15 % of the test duration while it has a very low slope during the remaining part of the experiment. The AE activity at the initial part of the test could be related to crack formation. There seems to be a correlation between the local jumps in the elongation curve and changes in the slope of the cumulative number of AE signals in different channels. A more detailed assessment of the correlation however would require the selection of the AE events per damage location, hence not discussed further in this section.

The AE hit rate for the vertical array of transducers is shown (Fig. 3.9). Sensor 1 displays an AE hit rate value of 0.7–0.8 signals per cycle from 0 % to about 35 % of test duration. The AE hit rate jumps above 1.0 signal per cycle after 35 % of the test duration. This possibly indicates two different rates of crack growth. After 85 % of the experiment, the hit rate level drastically decreases (i.e. AE quiescence). Sensors 2–4 show relatively similar behaviour between each other. Initially, they present an AE hit rate level in the range (that is the case for sensors 3 and 4) or even higher (see sensor 2) than the one of sensor 1. After about 25 % of the test duration, however, the hit rate does not exceed 0.5 signal per cycle (suggesting an average of 1 hit per every two load cycles).

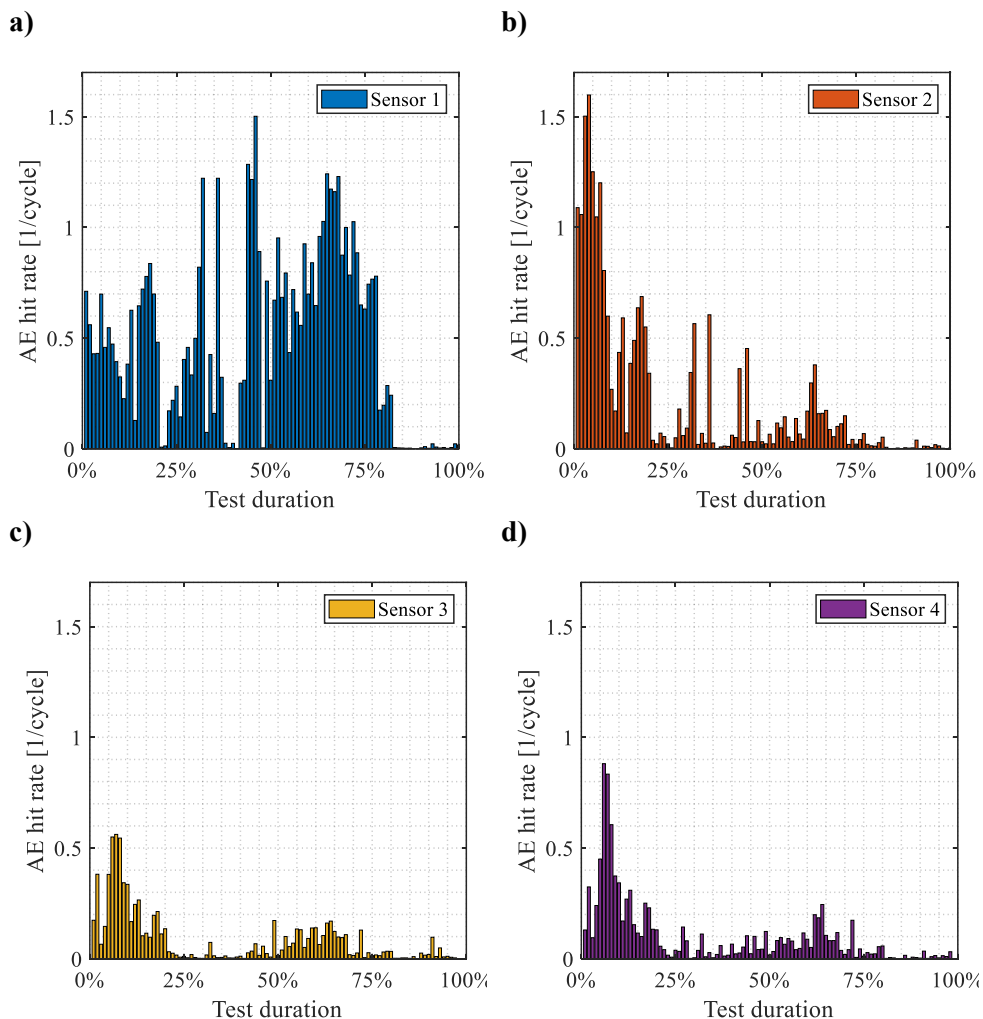


Figure 3.9. AE hit rate measured by the vertical array of AE transducers.

AE-based digital twin of fatigue

Damage-induced ultrasound signals have been localised using two movable arrays of AE transducers deployed on perpendicular planes. Results of the AE source localisation were projected on the 3D geometry of the chain segment in the form of a DT. The AE-based DT has been calculated using the procedure described in Section 3.2.2, and calculated over the grid points for each localised event for all the positions of the movable arrays. The grid has a uniform spacing of 10 mm in x, y,

and z directions. The speed of sound in water is considered to be 1500 m/s at 20°C. Also, a maximum allowable error (between the predicted and the actual differential arrival times of the wave) of 10 μ s has been used.

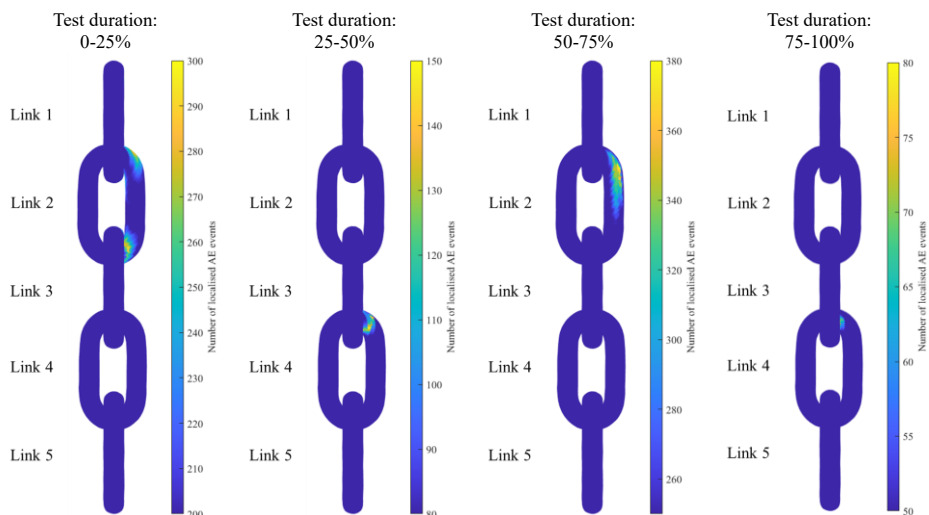


Figure 3.10. AE-based DT for different periods of the test duration.

The AE-based DT for four time periods of the test duration is shown (Fig. 3.10). Only from the AE-based DT, three damage zones can be identified. The damage zones are defined as the areas in the chain segment showing the highest number of localised AE events. These zones are located at the intersections of neighbouring links (i.e. Link 1–2, Link 2–3, and Link 3–4) and can generally be interpreted as the ‘crown areas’ (generally being the most susceptible to cracks, along with the welds). The first part of the test, 0–25 % of test duration, shows localised acoustic activity between Link 1–2 and Link 2–3. Both zones present a range of 250–300 localised AE events. In the second part of the test, 25–50 % of the test duration, the largest area of AE activity is located between Link 3–4, with 120–150 AE events. Between 50 and 75 % of the test duration, a relatively high number of AE events (in the order of 300–400) is localised around the crown area of Link 2, towards Link 1. The final

part of the experiment, between 75 and 100 % of the test duration, shows acoustic activity in the upper crown of Link 4, with 50–80 AE events.

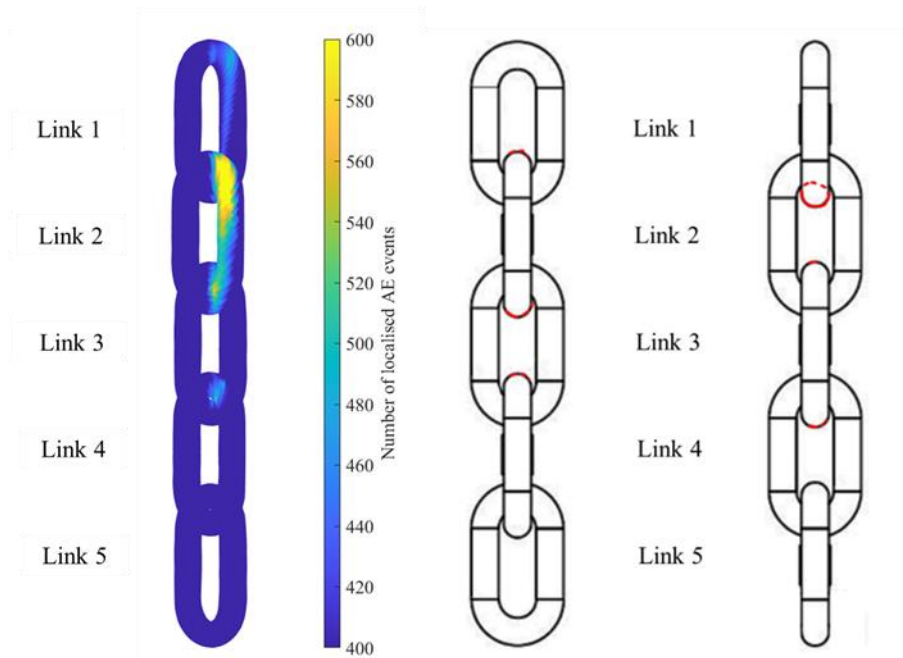


Figure 3.11. The overall AE-based DT of the chain (left) and the observed indications (red circle and red lines respectively) during the post-failure inspection (right).

The overall AE-based DT for the 100 h of measurements analysed is shown (Fig. 3.11). The DT reveals three distinct zones of acoustic activity. Acoustic activity is expected to have been detected all over the chain segment due to the natural corrosion process. However, highly localised AE activity can manifest the presence of fatigue cracks. The most prominent localised area is observed in Link 1–2. This is characterised by a number of localised AE events of approximately 600, spread between the crown and the weld area of Link 2. The second-largest area of AE activity is situated in the crown area of Link 2, towards Link 3, with 550–600 localised AE events. These initial observations suggest that Link 1–3 was the most acoustically active part of the chain, confirming early indications from the

parametric analysis of AE. A third zone of activity is noted in the crown of Link 4, toward Link 3, accounting for a total of localised AE events ranging between 450 and 500. A few limitations and improvement points can be identified in the AE-based DT. First, the localised areas seem to be biased against the middle part of the chain link crown (where fatigue crack is expected to grow). This bias may arise from potential masking effects on the damage-induced ultrasound signals and the limited number of sensors in play in the localisation. Possible improvements involve increasing the number of sensors in the movable arrays and accounting for masking issues in the AE source localisation algorithm. Second, the difference in AE events numbers may be related to the extent and stage of damage, but it is also influenced by the sensitivity of the sensors and the monitoring duration in each specific position (of the movable array). Future work will incorporate the normalisation of the AE source in the DT to enhance a more accurate comparison of the monitoring results.

Post-failure inspection

The condition of the chain segment was assessed at the end of the experiment through visual inspection and magnetic particle (MP) testing. All the links of the chain segment were tested. The positions in each link are labelled A, B, C, and D (Fig. 3.12). The reported observations are located in the crown area of the chain links. The results of the post-failure inspection are shown (Fig. 3.13). The main fracture (Fig. 3.13a) was observed in Link 1 towards Link 2. The results of the post-failure inspection are shown (Table 3.3).

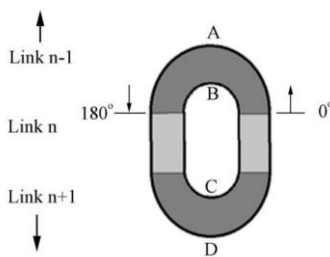


Figure 3.12. Positions in each link. Dark grey areas in the sketch were tested.

Link	Region	Observation	Shown in
Link 1	D	Fracture and linear indication measuring 12 mm.	Fig. 11a
Link 2	A	Linear indications measuring 6 mm, 4 mm, and several linear indications < 2 mm.	Fig. 11b
Link 3	D	Linear indications measuring 40 mm, 15 mm, 10 mm, and multiple linear indications < 5 mm.	Fig. 11c
	A	Linear indication measuring 10 mm.	Fig. 11d
	D	Linear indication measuring 10 mm, and multiple linear indications < 3 mm.	Fig. 11e
Link 4	A	Linear indications measuring 6 mm, 5 mm, and multiple linear indications < 3 mm.	Fig. 11f

Table 3.3. Results of post-failure inspection.

When combined with the previous insights (Fig. 3.11), it can be inferred that the main AE source localised in Link 1–2 correlates with the main fracture (and linear indications) in the chain segment. The entity of the secondary AE sources (i.e. the number of localised AE events) localised in Link 2–3 and Link 3–4 correlate with the indications observed in the respective areas. All the locations where indications were found through MP testing have been detected and localised using the remote AE technique. Furthermore, there are no indications by the AE that have not been found using MP testing. It can be concluded that a good correlation between the post-failure observation and the AE localisation has been found.

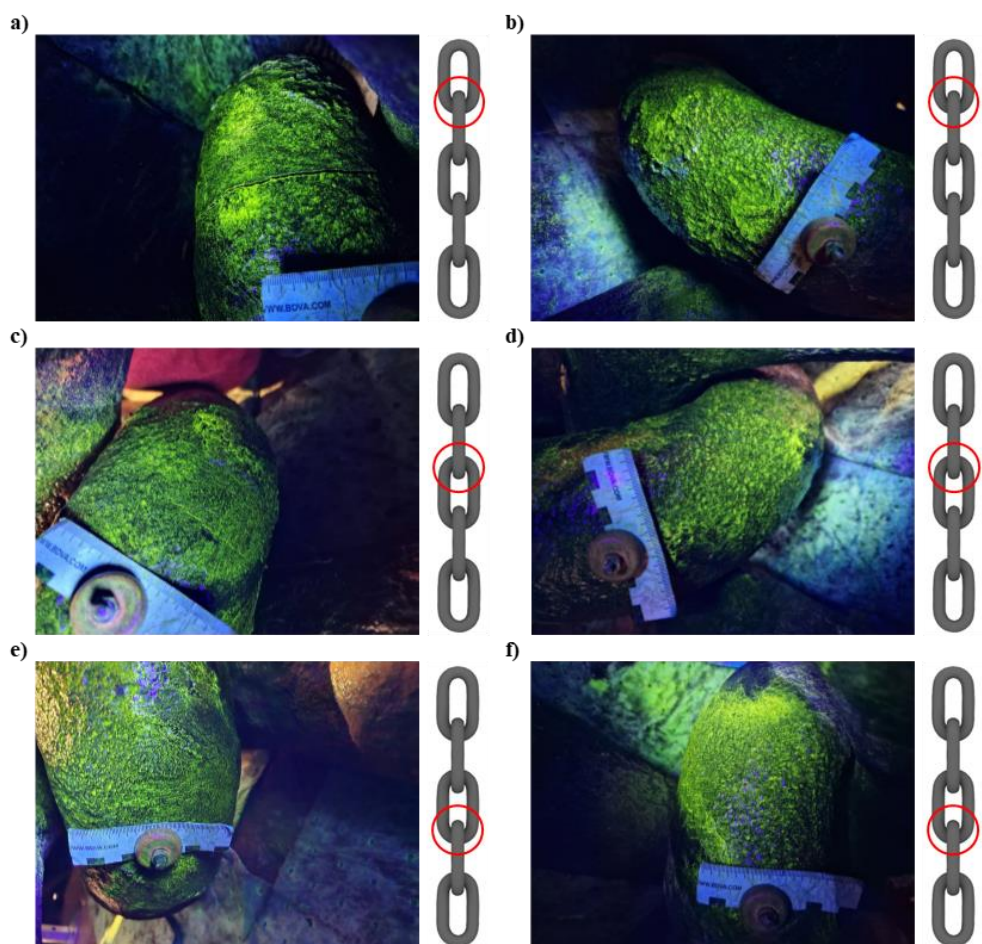


Figure 3.13. Results post-failure inspection. (a) Link 1, position D. (b) Link 2, position A. (c) Link 2, position D. (d) Link 3, position A. (e) Link 3, position D. (f) Link 4, position A.

3.4.2 DETECTION AND LOCALISATION OF CORROSION

Experiments described in Section 3.3.2 were performed and the methodology for the data analysis described in Section 3.2 was applied.

Detection and monitoring of corrosion

The total number of AE signals measured by each sensor in the perpendicular arrays is shown (Fig. 3.14). When combined with the AE sensors layout in Fig. 3.7, it can be inferred that most of the acoustic activity seems to be generated from the side of the links facing sensor group 2. Sensor 10 shows the maximum number of signals recorded (with 3.1×10^6 signals) followed by sensors 8, 6, and 4. This may indicate active AE sources in the part of the upper link towards sensor group 2 and facing sensor group 1. Sensor 1 displays the lowest number of AE signals recorded (with 0.3×10^6 signals) followed by sensors 3 and 5. This seems to suggest relatively low acoustic activity on the opposite side of the chain links.

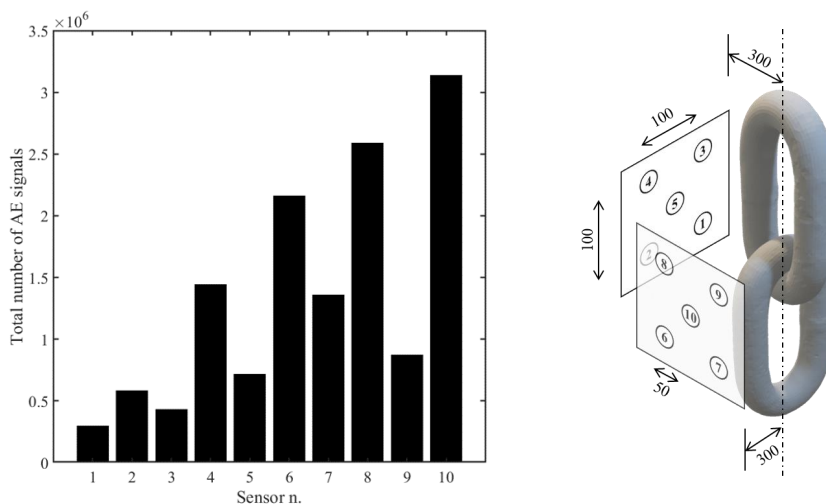


Figure 3.14. Total number of AE signals measured by each sensor (left) and schematic of sensors layout (right).

The cumulative number of AE signals recorded by each sensor in the perpendicular array is shown (Fig. 3.15). Among the sensors in group 1, sensors 1-3, and 5 seem to follow a similar trend throughout the experiment. After 1×10^5 seconds their curves show a constant and similar slope. Sensors 4 and 6-10 show a similar but steeper trend characterised by a constant slope of the curve (throughout the test) possibly indicating constant rate of the degradation process.

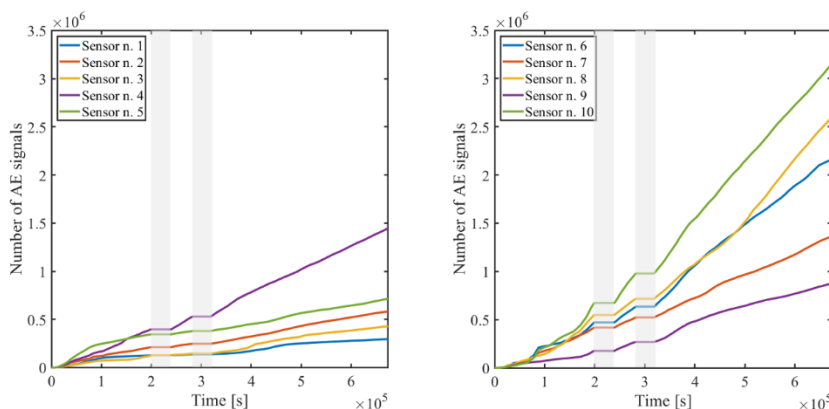


Figure 3.15. Cumulative number of AE signals measured by each sensor. Grey areas indicate the periods where measurements are not available.

The AE hit-rate recorded by the most active sensor in each perpendicular array is shown (Figure 3.16). Although the two sensors differ in the value of AE hit-rate (i.e. 3-4 hits per second) similar variations can be noticed. Sensor 4 measures 2-3 hits per second between 0 and 2×10^5 seconds (Fig. 3.16, left). Sensor 10 shows an increasing trend in AE hit-rate reaching 8-9 hits per second by the end of the same period. After 2×10^5 seconds, sensors 4 and 10 seem to measure a relatively stable AE hit-rate of 2-3 and 6-7 hits per second, respectively.

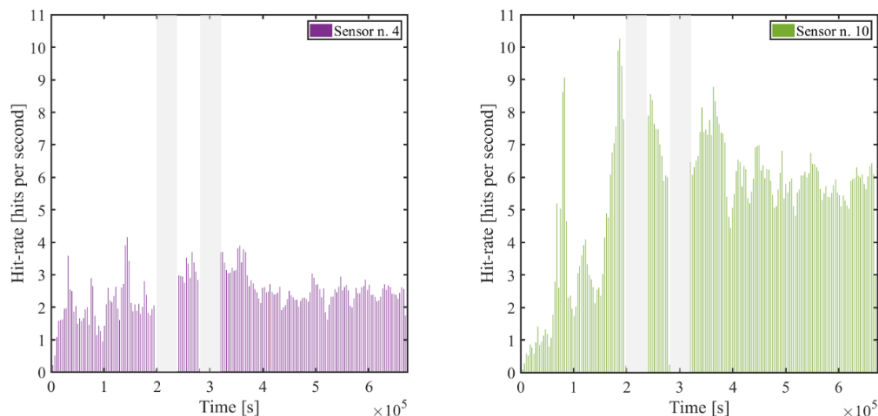


Figure 3.16. AE hit-rate measured by the most active sensor in each perpendicular array.

AE-based digital twin of corrosion

Damage-induced ultrasound signals have been localised using the two arrays of AE transducers facing the chain links from perpendicular planes. Results of the AE source localisation were projected on the 3D geometry of the chain links in the form of DT. The AE-based DT has been calculated using the procedure described in Section 3.2.2, and calculated over the grid points for each localised event recorded during a testing time of about 5 hours (between 4.9×10^5 and 5.1×10^5 seconds). The same parameters (grid spacing, speed of sound, maximum allowable error) as the localisation of fatigue-induced AE have been used.

The AE-based DT for a selected period of the test duration is shown (Fig. 3.17). The DT reveals one zone as the most acoustically active. This activity ranges from 1200 to 1300 localised AE events, resulting in a rate of localised AE events of 240-260 events per hour. An average of about 200 localised AE events is reported for the rest of the chain links surface.

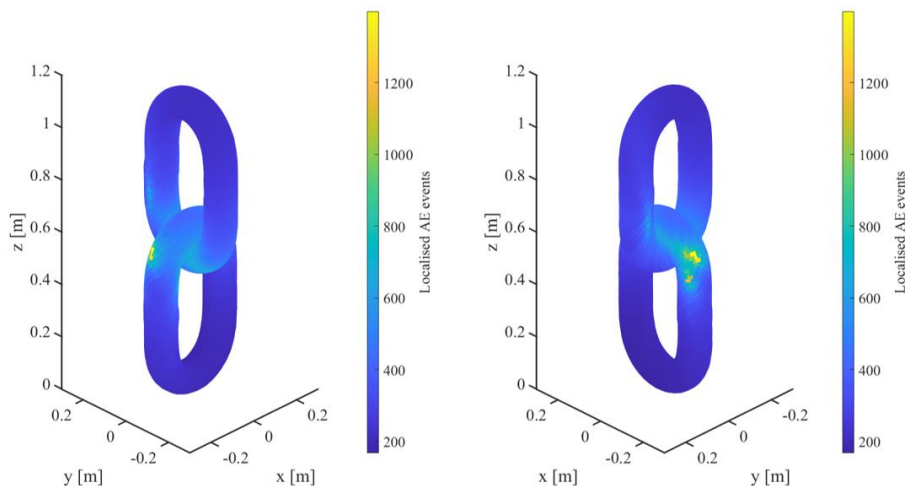


Figure 3.17. AE-based DT for a testing period of 5 hours.

3.4.3 ENVISIONED IMPLEMENTATION

The proposed approach can provide a qualitative assessment of corrosion-fatigue damage. Future work will be needed for in-situ application of the presented approach to real-world offshore mooring chains. The envisioned application may involve permanent instrumentation of the chain or installing the measurement equipment on remotely-operated underwater vehicles (ROVs). Underwater noise may be more pronounced in offshore conditions due to currents, ship propellers, waves, external operations, etc. Nonetheless, these sources are generally characterised by AE signatures with frequencies predominantly below 100 kHz [70-72], whereas corrosion-fatigue-induced AE signals are mostly pronounced in the range of 100–400 kHz. Further investigation will be needed to determine minimum requirements for offshore measurements and acquisition settings.

3.5 CONCLUSIONS

Large-scale corrosion-fatigue experiments were performed to assess the feasibility of detecting, localising, and monitoring corrosion-fatigue damage in mooring chain

links using underwater remote AE technique. A 5-link mooring chain segment was subjected to cyclic loading while submerged in artificial seawater. Ultrasound signals were continuously measured using a combination of a vertical array of 4x AE transducers and two movable arrays of 4x AE transducers each placed on perpendicular planes.

Parametrisation of the AE measurements was used to monitor the acoustic activity induced by the initiation and growth of corrosion-fatigue damage. The total number of AE signals highlighted the most active area in the test rig, i.e. upper links, attributed to a combination of damage-induced ultrasound signals and noise from the upper clamp. The cumulative number of AE signals displayed distinct activity patterns in the upper and mid-lower sections of the chain segment, with damage-induced ultrasound signals (in the upper part of the chain sample) characterised by two different slopes of the curve (possibly indicating a slow and fast rate of damage growth), and a characteristic AE quiescence in the later stage of the test. The AE hit rate confirmed distinct acoustic activity in the upper and mid-lower sections of the chain segment, with the former showing two levels of AE hit rate during the first (from 0 % to 35 %) and the second part (from 35 % to 85 %) of the test duration.

A 3D source localisation algorithm for damage-induced ultrasound signals was successfully implemented. Results of the AE source localisation were projected on the 3D geometry of the chain segment in the form of DT. The AE-based DT revealed three distinct zones of acoustic activity. The range of localised AE events varied between 450 and 600 events for the lowest and highest acoustic activity regions, respectively.

A good correlation between the post-failure MP testing and the AE localisation has been found. All the locations where indications were found through MP testing have been detected and localised using the remote AE technique.

Large-scale corrosion experiments were performed to assess the feasibility of detecting, localising, and monitoring corrosion damage in mooring chain links using non-contact AE technique. A 2-link mooring chain segment was subjected to accelerated corrosion while submerged in natural seawater. The applied acceleration is expected to influence predominantly the rate of corrosion, without altering the general electrochemical processes responsible for AE generation; therefore, the signal characteristics can be considered representative of natural corrosion as well (at a different rate). Ultrasound signals were continuously measured using two arrays of 5x AE transducers placed at a fixed distance from the chain and facing the specimen from perpendicular planes.

Parametrization of the AE measurements was used to monitor the acoustic activity induced by the corrosion process. The total number of AE signals highlighted the most active areas in the chain links. The cumulative number of AE signals displayed distinct activity patterns for two groups of AE sensors. Both the groups show a constant slope of the curve, possibly indicating a constant rate of the degradation process. The AE hit-rate of the two most active sensors in the two perpendicular arrays show high similarity, likely induced by the same AE sources. The AE hit-rate confirmed a relatively stable rate of degradation.

A digital twin representation and a 3D source localisation algorithm for corrosion-induced ultrasound signals were successfully implemented. Results of the AE source localisation were projected on the 3D model of the chain surface in the form of DT. The AE-based DT revealed the most acoustically active zone on the chain surface with 1200-1300 AE events localised in five hours of testing (i.e. 240-260 AE events per hour).

Fatigue crack growth prognosis in submerged mooring chains using non-contact Acoustic Emission monitoring

This chapter is based on the journal article:

F. Riccioli, H. den Besten, and L. Pahlavan, “Feasibility assessment of crack growth prognosis in submerged mooring chains using remote acoustic emission monitoring,” submitted to *Structural Health Monitoring*, 2025.

4 FATIGUE CRACK GROWTH PROGNOSIS IN SUBMERGED MOORING CHAINS USING NON- CONTACT ACOUSTIC EMISSION MONITORING

4.1 INTRODUCTION

Despite the promising results for fatigue crack detection and monitoring in full-scale mooring chains using AE [58-59; 87], earlier studies lack quantitative crack growth information and do not address the potential for fatigue life prediction.

Numerous investigations have been conducted using small-scale experiments to relate the AE data to the crack growth behaviour (e.g. [42-44; 74; 88-97]). In early research, the AE count rate was used to describe the crack growth behaviour. Harris et al. [91] proposed a model relating AE count rate to stress intensity range, based on the energy released during crack growth. Building upon earlier models, Lindley et al. [92] and Sinclair et al. [93] incorporated the influence of plastic deformation and fracture within the plastic zone (in addition to crack extension) on the AE. Research then focused on quantitatively correlating other AE parameters (e.g. AE hits, amplitude, duration, energy, entropy, etc.) with crack growth rate or stress intensity range to predict fatigue crack length [42-43; 89-90; 94-95; 97-99]. Recent studies have identified AE energy as a highly effective indicator for both qualitatively and quantitatively characterising fatigue crack growth [42; 74; 88; 96].

Crack growth prognosis using AE in large-scale specimens presents significant challenges due to multiple complexities. A key difficulty is accurately determining the stress intensity range, which is crucial for assessing fatigue crack growth. This challenge is further compounded by uncertainties in crack geometry, including crack size and propagation path. Additionally, large-scale structures often experience complex loading conditions, with unknown far-field stress states that further hinder precise assessments. Complex crack behaviour, such as crack closure and crack

opening modes (I, II, III) may also influence the AE behaviour. In the case of large-scale mooring chains, limited accessibility during testing - particularly in underwater environments - poses an additional constraint. Direct crack size measurements are often impractical, necessitating the development of novel techniques capable of remotely monitoring crack growth underwater. To the best of the authors' knowledge, no existing research has specifically investigated the use of remote underwater AE for crack growth prognosis in full-scale experiments.

This chapter investigates the feasibility of crack growth prognosis in mooring chains through underwater non-contact AE technique. A segment of a full-scale mooring chain was tested for fatigue in submerged conditions. Crack-induced AE signals have been monitored using underwater transducers in a non-contact manner. Crack growth prognosis is performed using a model based on the Paris-Erdogan relation and AE signals energy. A sensitivity study investigates the influence of varying model parameters on the crack growth prognosis results. The predictive capabilities of the proposed framework are assessed and quantified for future practical applications.

4.2 FATIGUE CRACK GROWTH PROGNOSIS USING NON-CONTACT ACOUSTIC EMISSION

Non-contact AE measurement for a full-scale mooring chain sample underwater is schematically shown (Fig. 4.1). Crack-induced ultrasound waves can travel through bulk materials like mooring chain links as bulk, surface, or guided waves, based on the frequency of the wave [40; 61]. As these waves propagate through seawater, they travel at the constant speed of sound as pressure waves. The interface between two media may cause reflected and transmitted waves [62]. The amplitude of the transmitted and reflected ultrasound waves is influenced by the acoustic impedance (r) and sound speed (c) of both the chain material and seawater, as well as the

incident angle [63]. Ultrasound wave components with enough energy to overcome geometric spreading and material attenuation can reach the ultrasound transducer.

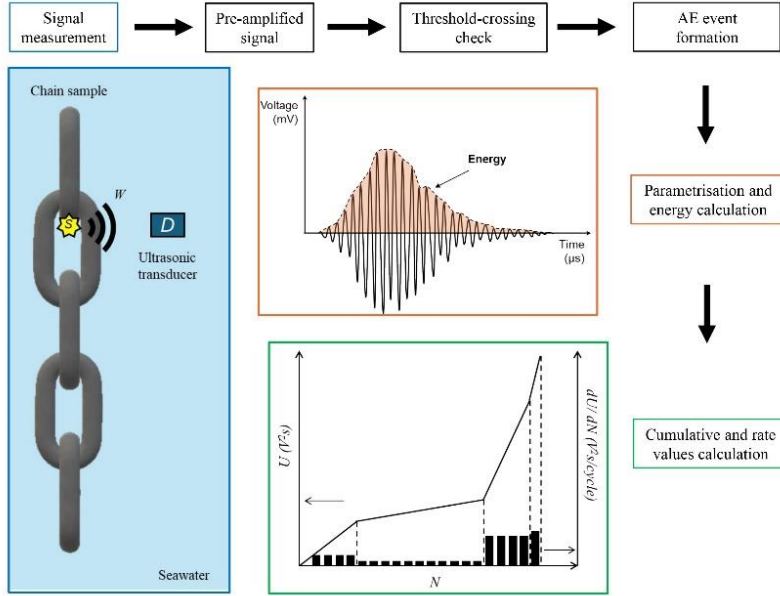


Figure 4.1. Underwater non-contact AE measurement for a mooring chain sample.

In the frequency domain, the measured signal P can be expressed as the convolution of the crack-induced source signal S with the propagation (transfer) function, W , and the transducer transfer function, D , as in

$$P = DWS + N \quad (4.1)$$

where N represents the background noise and any disregarded components of the ultrasound wave, such as reflections from neighbouring surfaces. If N is sufficiently small, the total energy of AE signals measured during the monitoring time can be calculated and approximated as:

$$U = \sum_i U_i = \sum_i \int (P_i)^2 d\omega = \sum_i \int (DWS_i)^2 d\omega = \sum_i \int (ZS_i)^2 d\omega = \sum_i \sum_j \Delta\omega Z_j^2 S_{ij}^2 \quad (4.2)$$

where Z denotes the consolidation of propagation transfer functions on the path from the source S to the ultrasound sensor [64; 87], and ω denotes the angular frequency.

The AE energy rate (i.e. measured signals energy per unit time) can be discretely calculated as:

$$\frac{dU}{dN} \approx \frac{\Delta U}{\Delta N} = \frac{\Delta U}{f \cdot \Delta t} \quad (4.3)$$

where f and Δt are load frequency and monitoring time respectively.

The energy of the AE signals measured by the ultrasound transducer is directly linked to the energy released (as elastic waves) while the crack propagates. Released energy is intrinsically linked to the extent of crack growth. This relationship linking the AE signal energy to the crack extension provides the foundation for determining the crack growth rate. This approach shares the fundamental concept with Griffith [100], who related the energy release rate to crack propagation in brittle materials such as glass.

4.2.1 THEORETICAL MODEL FOR FATIGUE CRACK GROWTH PROGNOSIS USING ACOUSTIC EMISSION

For a given set of loading conditions, stable crack growth behaviour (i.e. Stage II) in the material can be described by the Paris-Erdogan relation [101]:

$$\frac{da}{dN} = C(\Delta K)^m \quad (4.4)$$

where ΔK is the stress intensity range and C and m are material constants, with m typically ranging between 2-4 for ductile metals [102]. Assuming that the fatigue life of the chain segment is dominated by stable crack growth (Eq. 4.4) the relation between AE energy rate and stress intensity range can be expressed as:

$$\frac{dU}{dN} = B(\Delta K)^p \quad (4.5)$$

where B can be considered as a material constant, for a component under certain loading conditions, and p is generally considered equal to $(m + 2)$ [88; 103]. In engineering applications, p may be smaller than $(m + 2)$ due to the attenuation and filtering of the AE signals [74].

For full-scale structures, obtaining the stress intensity range is often challenging due to several factors. These include the complexity of crack geometry (including size and path), the limited information regarding the loading conditions, and the unknown far-field stress state. Therefore, by combining Eq. 4.4 and Eq. 4.5, an expression can be obtained to relate crack growth and AE energy rate independently of ΔK

$$\frac{da}{dN} = D \left(\frac{dU}{dN} \right)^q \quad (4.6)$$

where $D = C / (B)^q$, $q = m / p$.

4.2.2 CALCULATION OF MODEL PARAMETERS

Parameters D and q are required to establish the link between crack growth and AE energy rate (Eq. 4.6). These parameters can be derived in a few different ways, each with its level of complexity and precision. Coefficients may be assumed based on established literature or industry standards. While this approach offers simplicity, the generic values adopted may not reflect the conditions of specific applications (e.g. material behaviour, loading conditions, environmental factors). Calculating them directly from test data is an alternative option. While deriving coefficients from test data is more challenging, it can yield higher accuracy by directly reflecting the conditions and behaviours observed in a specific test. However, this approach often requires specific designed experiments and applicability of the derived coefficients to situations outside the specific test conditions can be limited. Various methods can

be used for calculating these coefficients. Small-scale tests, combined with AE monitoring, offer one approach to characterise the material properties under specific loading conditions [74; 88; 104-106]. However, challenges lie in ensuring that the small-scale test accurately represents the behaviour of the large-scale structure, especially concerning factors like constraint, geometry, and environmental effects. Similarly, large-scale tests can also be conducted to capture data representative of a structure under specific operational conditions [106-108]. While more representative, large-scale tests are significantly more expensive and time-consuming, this often limits their practicality. Furthermore, even large-scale tests might not perfectly replicate real-world operational complexities. Although challenging, field tests also represent a possible option. In addition to the high costs, a key difficulty is that damage cannot be induced in operational units for clear safety reasons, and natural damage progression is often slow and unpredictable. Moreover, accurately quantifying damage in situ is complicated due to limited accessibility and the complexity of monitoring under real operational conditions. Another approach may involve using established equations for the stress intensity factor, which can be combined with finite element modelling (FEM) or analytical expressions of stress (σ) to estimate da/dN as a function of ΔK , therefore determining the relevant constants. This method relies heavily on the stress intensity factor solutions accuracy and the fidelity of the FEM model. Simplifications in the model or inaccuracies in the stress intensity factor equations can lead to inaccurate derivation of the parameters. A similar method could be applied to dU/dN as a function of ΔK , particularly at the initial and final stages of the test where the crack size can be readily known (if the crack length is not measured throughout the entire test), allowing calibration of the relationship across the testing range. Although this approach can benefit from accurate crack length measurements at the beginning and end of the test, it assumes a reliable crack growth model to estimate the crack length at other points which can also introduce uncertainties in the parameters estimation. Alternatively, with known parameters C and m and assuming a known form for the

stress intensity factor equation, one could formulate and solve a system of equations to estimate crack depth, a , and constants as functions of dU/dN across multiple data points, for possibly enhanced understanding of the constants over different stages of crack progression. This approach also relies on the accuracy of the assumed stress intensity factor equation and can be sensitive to the quality of dU/dN data. Furthermore, the approach still relies on the assumption of known C and m parameters.

In this study, which primarily seeks to assess the feasibility of the prognosis model for full-scale mooring chains, coefficients are initially assumed based on literature data, and sensitivity analysis of the model parameters is performed to understand and identify the key dependencies. This approach has been chosen as a first step due to its relative simplicity. The limitations of this assumption are acknowledged, and future work will explore more refined methods for determining D and q , including experimental calibration and advanced modelling techniques.

4.2.3 ESTIMATION OF FATIGUE LIFE USING ACOUSTIC EMISSION

A relationship linking the measured AE energy rate to the crack growth rate is established through the appropriate selection of model parameters. The relationship enables the conversion of AE energy (measured per unit time during a finite monitoring period) into crack growth rate information. The predictive capabilities of the crack prognosis model are assessed following the illustrated schematic (Fig. 4.2). The assessment considers different inspection windows across the structure lifetime. In each inspection window, the increase in crack depth is calculated from the measured AE energy using

$$a - a_{t_i} = \int_{t_i}^{t_e} D \left(\frac{dU}{dN} \right)^q dN \quad (4.7)$$

where a is the crack depth at the final instance (t_e) and a_{t_i} indicates the crack depth at the initial instances (t_i) of the inspection windows (Δt).

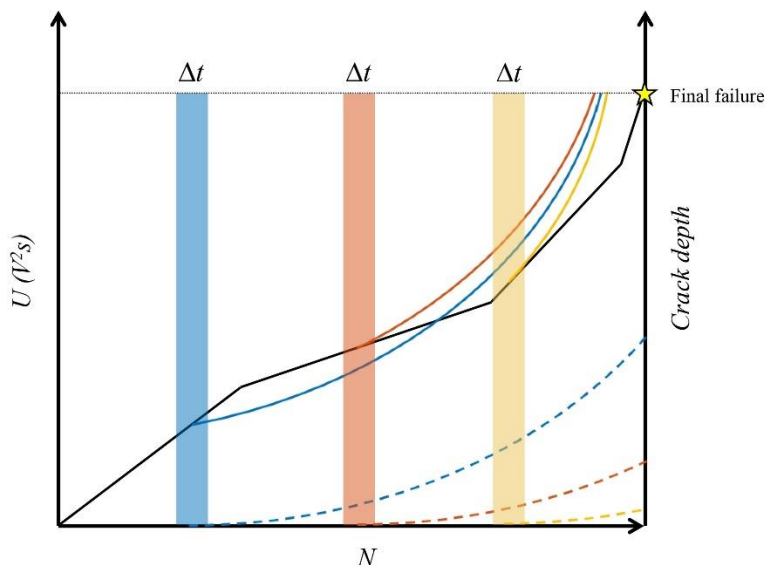


Figure 4.2. Schematic of the assessment of predictive capabilities of crack prognosis model. The solid black line indicates the cumulative energy of AE signals measured over the number of cycles, up to final failure. The solid-coloured lines schematically illustrate the crack growth prediction with known initial crack depth. The dashed-coloured lines schematically represent the crack growth prediction with an initial crack depth unknown (assumed 0.1 mm [109]). The blue, orange, and yellow colours stand for first, second, and third inspection window.

To assess the predictive capabilities of the model, two scenarios are compared for each considered inspection window (Fig. 4.2). In the first scenario, the initial crack depth a_{t_i} is unknown at the moment of detection and hence assumed conventionally zero and the minimum detectable crack size for standard NDTs, 0.1 mm [109-114] (dashed lines, Fig. 4.2). In the second scenario, crack growth is detected and crack

depth a_{t_i} is assumed measured (solid lines, Fig. 4.2). Two assumptions are made: (i) the entire crack growth process is governed by the Paris-Erdogan relation (from the moment of detection until final failure) and (ii) the energy rate term is equal to the one at the moment of damage detection for the entire growth process. The prediction accuracy of the model is evaluated by calculating the error in predicted fatigue life as a percentage of the actual (test) fatigue life. This error quantifies the model effectiveness in forecasting fatigue behaviour under varying initial crack conditions.

4.3 TEST DATA

A full-scale fatigue experiment was performed on a chain segment, subject to fatigue loads while submerged in artificial seawater. Crack-induced AE were monitored using underwater non-contact transducers. This section summarises the highlights of the full-scale test since Chapter 3 presents the experiments in detail.

4.3.1 FULL-SCALE EXPERIMENT

Fatigue testing was carried out on a mooring chain segment retrieved from offshore service using a vertical test rig. The studless R4 steel grade chain sample is characterised by a 137 mm nominal diameter and 16992 kN nominal Minimum Breaking Load (MBL). During the test, artificial seawater (i.e. 3.5 ± 0.1 wt-% sodium chloride solution) surrounded the chain segment subjected to fatigue cycles. The fatigue test was conducted under load control, with test parameters outlined in Chapter 3.

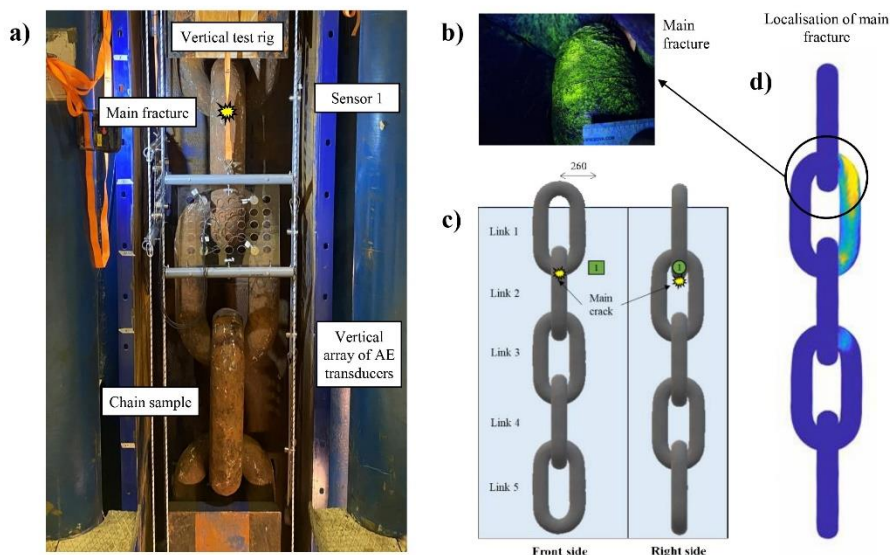


Figure 4.3. (a) Instrumented test rig and vertical array of transducers. (b) Main fracture inspected using MP testing. (c) Schematic of sensor arrangement. Dimensions in mm. (d) AE-based DT showing localisation of main fracture [87].

4.3.2 ACOUSTIC EMISSION MEASUREMENTS

An array of non-contact watertight AE transducers was installed on the vertical rig spanning over the length of the chain segment (Fig. 4.3) to continuously monitor crack-induced ultrasound signals. The transducers were placed at a fixed distance and secured using sensor holders and carabiners. Chapter 3 provides a detailed explanation of the test setup and instrumentation. The sensor closest to the main fracture location (i.e. Sensor 1, Fig. 4.3c) has been considered for the purpose of this investigation.

Crack-induced signals were recorded using AMSY-6 Vallen data acquisition (DAQ) system. Watertight coaxial cables connected the DAQs and the watertight piezoelectric AE sensors (VS150-WIC-V01, preamplifier gain of 34 dB). These transducers have a resonant frequency of 150 kHz and operate within a 50-450 kHz

frequency range [58-59; 68]. The transfer function of the transducers can be seen in Alkhateeb et al. (2022) [68]. The signal sample rate was 2.5 MHz, with a total sample length of 4096 points. The test setup and sensor layout are schematically shown (Fig. 4.3).

Before testing, pencil lead break tests were carried out (as suggested by ASTM E976-15 [69]) in various positions on the outer part of the test rig (after the tank was filled up) to confirm the AE sensor response reproducibility in water and the correct functioning of the AE measurement system. In the commissioning phase, noise levels were evaluated under cyclic loads applied to the submerged chain sample. The recorded noise level was approximately 50 dB, leading to an acquisition threshold set at 60 dB.

4.3.3 POST-FAILURE INSPECTION

The integrity of the chain sample was evaluated before and after fatigue testing through visual and magnetic particle inspection. No crack indications were found before testing. The fatigue test ran until specimen failure. The inspection at the end of the test found the main fracture in Link 1 towards Link 2 (Fig. 4.3b and Fig. 4.3d). Secondary indications of initiated cracks were also found in the other link-to-link areas (i.e. Link 2-3 and Link 3-4). Chapter 3 provides a detailed description of the post-failure inspection.

4.4 RESULTS AND DISCUSSION

Following the experiments (Section 4.3), the proposed methodology (Section 4.2) was applied for the analysis. AE energy was calculated for 22 hours of testing. These time windows were selected to cover the entire duration of the experiment. AE energy rate was calculated for each measurement hour. The energy rate was defined as the total energy measured by the sensor divided by the number of cycles performed within that hour. The cumulative trends were calculated by integrating

the rates over the test duration using the trapezoidal rule. For the analysis, only the signals with amplitudes exceeding 65 dB were considered to filter out potential noise sources.

4.4.1 FATIGUE CRACK GROWTH PROGNOSIS

The crack growth rate was calculated from the AE energy rate (Eq. 4.6). The parameters C and m , as specified in BS 7910 [115], were used. Hence, the values are $C = 2.3 \times 10^{-12}$ and $m = 3$ for da/dN in mm/cycle and ΔK in $\text{N}/\text{mm}^{3/2}$. The AE parameter B was initially estimated to satisfy the condition that $a = D$ at $N = N_f$ (Figure 4.4) while $p = m + 2$ was adopted as proposed by Yu et al. (2011) and (2012) [74; 88].

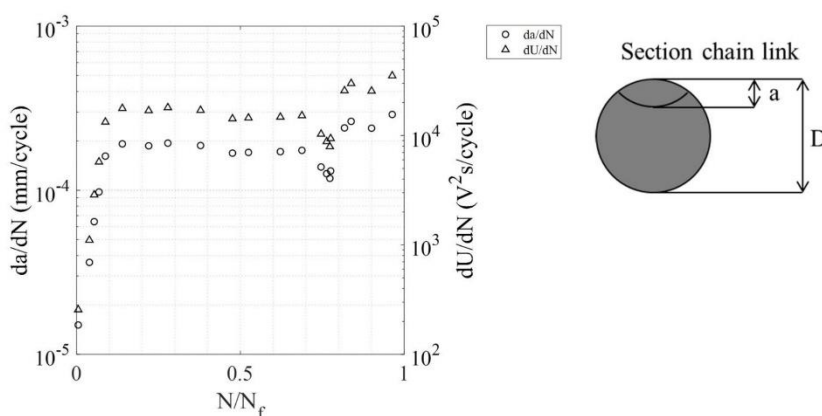


Figure 4.4. Calculated crack growth rate (da/dN) and measured AE energy rate (dU/dN) as a function of the normalised number of cycles. N indicates the number of cycles, divided by the number of cycles at failure N_f . Crack size a is divided over the chain link diameter D .

The calculated crack growth rate and the measured AE energy rate over the normalised number of cycles are shown (Fig. 4.4). The AE energy rate shows an initial increase in values as the test progresses, reaching a relatively stable plateau in

the middle of the test duration. Towards the end, the energy per cycle increases, potentially indicating a change in the crack growth behaviour. The initial increase in energy rate suggests the onset of crack growth, where AE activity begins to rise. The stable rate around the middle of the test likely represents stable crack propagation, where the crack grows at a relatively constant rate and AE energy remains relatively uniform. The increase near the end might indicate a stage where crack growth accelerates, most likely due to the impending failure. The stable phase may correspond to the stable crack growth region described by the Paris relation, while the initial and final phases could represent the transition regions before and after stable growth. Similarly, the calculated crack growth, at the beginning of the test (up to 10-20% of the number of cycles), starts at a lower magnitude, around 1×10^{-5} mm/cycle. This may reflect an early-stage growth phase, corresponding to minor crack advancement or initiation. For a large portion of the test duration (from around 20% to 80%), the crack growth rate remains nearly constant, approximately around 2×10^{-4} mm/cycle. This phase suggests a stable crack growth, where the crack advances at a constant rate under the cyclic loading. This phase aligns with the crack growth stage described by the Paris relation. Near the end of the test (from approximately 80% onwards), there is a noticeable increase in crack growth rate, suggesting accelerated crack growth. This phase might indicate the onset of instability as the crack approaches a critical stage.

The cumulative AE energy and the crack depth as a function of the normalised number of cycles are shown (Fig. 4.5). The plot illustrates a steady accumulation of AE energy as the test progresses. Initially, the cumulative energy grows slowly, followed by a significant increase starting around 10-20% of the normalised number of cycles. Toward the end, the accumulation rate appears to increase, indicating an acceleration in AE energy release, especially in the final cycles of the test. The initially slow growth in energy suggests minimal crack propagation (or early-stage crack nucleation), where AE are likely less frequent or lower in intensity. The middle

phase, characterised by a steep slope, likely represents a period of active crack growth. This phase correlates with high AE activity, possibly due to micro-cracking events and other damage mechanisms. The steeper curve towards the end could signify that the crack has reached an unstable configuration, with a high energetic rate of AE signals.

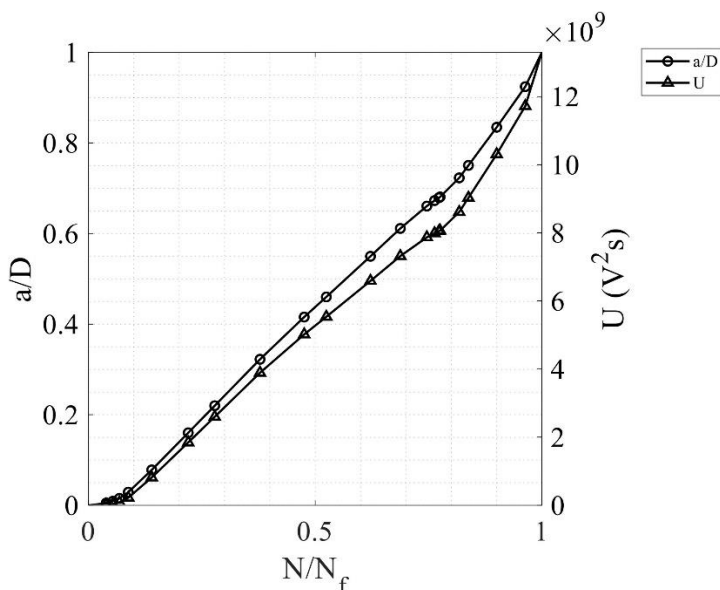


Figure 4.5. Crack depth and cumulative AE energy as a function of the normalised number of cycles.

The crack depth curve shows a slow growth at the beginning of the test. This aligns with typical early-stage crack growth behaviour, where crack initiation or very slow propagation occurs due to lower energy release rates. The low values of crack depth in this phase suggest that significant crack growth has not yet occurred. From approximately 20% to 80% of the test duration, the crack length increases steadily. This linear section indicates a stable crack growth rate. Near the end of the test, there is an evident increase in the crack depth. This accelerated growth suggests an unstable crack propagation phase. This phase is characteristic of the final stages of

fatigue crack growth and indicates the approaching failure. Overall, the observed curve shape is consistent with typical fatigue crack growth behaviour, characterised by an initial slow growth, a stable phase, and an accelerated phase as failure approaches.

4.4.2 SENSITIVITY ANALYSIS

A sensitivity analysis of the calculated crack depth (Fig. 4.5) was conducted to evaluate the influence of the AE parameters B and p on the prognosis quality. The parameters C and m were held constant, as for BS 7910. Although changes in these parameters may additional influence the prognosis results [109; 116], for the purpose of this feasibility study, they have been considered fixed. The combination of parameters used for this analysis is presented (Table 4.1).

B	p
B_0	$m + 1$
$50\%B_0$	$m + 2$
$150\%B_0$	$m + 3$

Table 4.1. Values of parameters B and p used for the sensitivity analysis.

$$B_0 = 1.113 \times 10^{-9}, \text{ to satisfy that } a = D \text{ at } N = N_f.$$

The calculated crack depth over normalised test duration for different combinations of parameters B and p is shown (Fig. 4.6). Varying B results in distinct crack growth trajectories from the baseline (i.e. $B_0 = 1.113 \times 10^{-9}$, solid lines). Reducing B (dashed lines) overestimates crack growth, resulting in the crack reaching a greater depth within the same normalised number of cycles (indicating a shorter fatigue life). Increasing B (dotted lines) underestimates the crack growth and the final crack size, compared to the baseline (potentially leading to a longer fatigue life). This trend is observed in all scenarios of p (i.e. $m + 1$, $m + 2$, and $m + 3$). Decreasing the exponent p leads to significantly larger overall crack depths (scaled up to the order of 10^4 mm)

compared to the baseline case ($m + 2$). Conversely, increasing p (for example to $m + 3$) results in a substantial underestimation of the final crack depth. These variations show how relatively small differences in the exponential term can lead to largely different results.

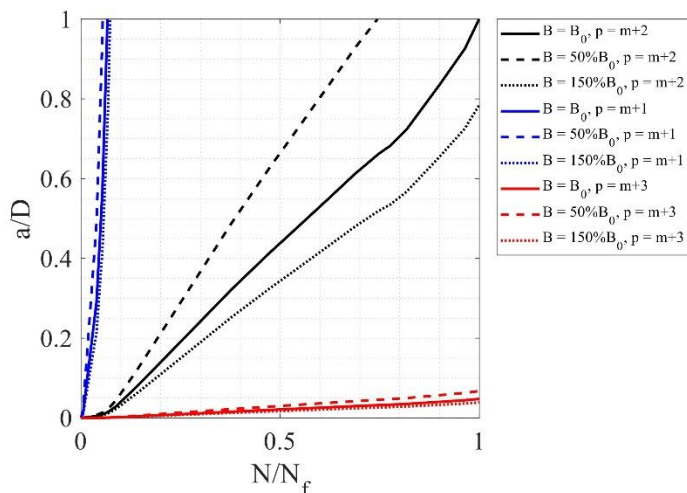


Figure 4.6. Sensitivity analysis of crack depth prognosis.

4.4.3 FATIGUE LIFE ESTIMATION

The fatigue life of the chain sample was estimated using crack growth calculated from AE data to evaluate the quality of the proposed approach in prediction. Three inspections (each of 1 hour of continuous monitoring) are considered during the structure lifetime, corresponding to the test duration (i.e. number of cycles). The three inspections occur at 25%, 50%, and 75% of the test duration (inspections A, B, and C, Fig. 4.7). In each of the considered inspection windows, the crack growth rate is calculated from the AE energy rate based on the methodology described and the parameters $B = 1.113 \times 10^{-9}$ and $p = m + 2$ (with $C = 2.3 \times 10^{-12}$ and $m = 3$).

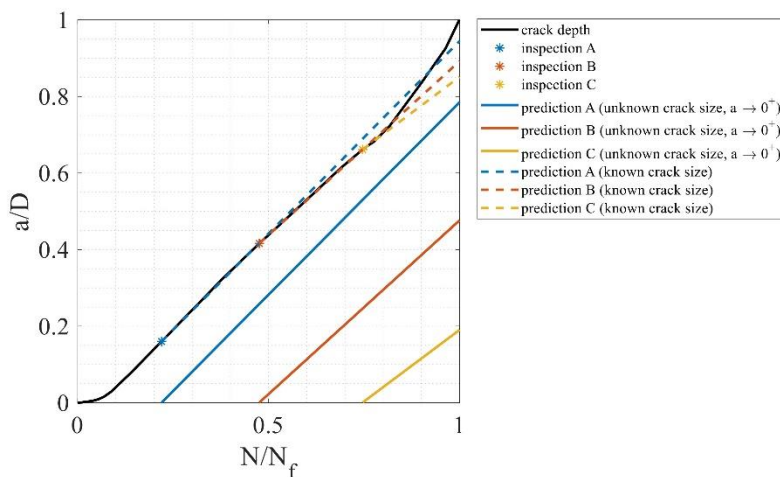


Figure 4.7. Estimation of fatigue life using AE.

Fatigue life predictions for different inspection scenarios are compared (Fig. 4.7). The black solid line represents the calculated crack depth throughout the test duration (for $B = 1.113 \times 10^{-9}$ and $p = m + 2$). Inspection points A, B, and C (at 25%, 50%, and 75% of the test duration, respectively) are marked along this curve. These points provide real-time estimates of the crack growth rate based on the measured AE energy rate. The solid lines for predictions A, B, and C (blue, orange, and yellow, respectively) represent crack depth predictions starting from an unknown and/or negligible initial crack size (assumed equal to 0.1 mm). These predictions appear to underestimate the final crack size resulting in a largely non-conservative final estimation of the fatigue life. This deviation from the actual fatigue life underscores the limitations of assuming a negligible initial crack size. The dashed lines correspond to predictions A, B, and C assuming a known initial crack size at each inspection point (moment of detection). These predictions closely align with the crack depth curve. The closer fit of these predictions suggests that accurate initial crack size information can benefit the prognosis of crack growth.

Scenario	Prediction error (% of test duration)
Prediction A (unknown crack size, $a \rightarrow 0^+$)	21%
Prediction B (unknown crack size, $a \rightarrow 0^+$)	58%
Prediction C (unknown crack size, $a \rightarrow 0^+$)	108%
Prediction A (known crack size)	5%
Prediction B (known crack size)	12%
Prediction C (known crack size)	20%

Table 4.2. Prediction error in percentage of actual fatigue life (test duration) for different scenarios.

The prediction errors across different scenarios are collected (Table 4.2). The results reveal important insights into the quality of fatigue crack growth predictions when using either a minimal initial crack size assumption or known crack sizes. Predictions that used a known initial crack size show much lower error percentages compared to those that assumed the initial crack size (equal to 0.1 mm). Prediction from point A (with known crack size) has an error of only 5%, which is significantly more accurate than the 21% error of the prediction from the same point but with the assumed crack size. Similarly, both the predictions from point B and point C (with known crack size) have errors of 12% and 20%, respectively, which are substantially lower than their counterparts with near-zero crack size assumptions (58% and 108%). This difference highlights the importance of having an accurate estimate of the (initial) crack size or defining it as a model calibration parameter, embedding all uncertainties in it in the future research. The errors for the prediction from point B and point C (with unknown and/or negligible crack size) are 58% and 108%, respectively, indicating a large deviation from actual crack growth. These errors imply that using an assumed initial crack size close to zero may result in overly non-conservative predictions. The prediction error increases with each successive inspection point (from A to C) in both cases (known and unknown crack size). For

example, when crack size is considered virtually zero, errors increase from 21% (Prediction A) to 108% (Prediction C). Similarly, when crack size is known, errors grow from 5% (Prediction A) to 20% (Prediction C). This trend suggests that prediction errors may increase over time as crack growth accelerates. Even when using known initial crack sizes, some model assumptions may not fully capture the crack growth behaviour in later stages. This observation underscores the limitation of the assumption and the importance of periodically feeding the model using new inspection data to ensure ongoing prediction accuracy. With information about initial crack sizes, prediction errors are reduced to 5–20%, making these predictions reliable enough for practical applications. Although incorporating the crack size as the initial condition for the predictive model can improve its accuracy, it is notable that the prediction results are overall non-conservative (in both scenarios). The most likely causes of this are: 1) the limit of the Paris relation (not capturing the final, unstable, stage of the crack growth), and 2) the assumption of unknown crack depth (for the first scenario only).

4.5 CONCLUSIONS

The study demonstrated the feasibility of using remote AE monitoring for crack growth prognosis in submerged mooring chains. A full-scale chain segment was tested for fatigue in artificial seawater, and AE were monitored throughout the fatigue test. This allowed for the evaluation of a prognosis model based on the Paris relation and AE energy, and investigation of key dependencies through sensitivity analysis.

AE energy rates were calculated at various instances of the fatigue test. AE energy and its rate suggested distinct phases of crack growth, including initiation, stable propagation, and acceleration toward failure. Crack growth rate (and crack depth) were calculated from the AE energy rate using the proposed approach. The results highlighted the characteristic stages of crack growth, as the AE energy rate

suggested. The stable phase, spanning most of the test duration, aligns with the Paris relation, while the final stage highlights the transition to unstable growth.

A sensitivity analysis was performed varying AE parameters B and p . The results demonstrated the influence of parameters B and p on crack growth prognosis. Reducing B led to overestimated crack growth and shorter predicted fatigue life, whereas increasing B resulted in underestimated crack growth and longer predicted fatigue life. The choice of p magnified these effects. Smaller p led to significant overestimation of the crack depth, while larger p resulted in a substantial underestimation of final crack depth. This highlights how small differences in the exponential term can lead to relatively large uncertainties in the performed prognosis.

The accuracy of the proposed approach for predicting fatigue life was evaluated and quantified. The predictions highlighted the importance of incorporating an accurate initial crack size and using an adequate and calibrated (perhaps with field data) crack growth model. Predictions that assume an initial crack size of zero tend to underestimate both the final crack depth and the fatigue life (with errors ranging between 21% and 108%). In contrast, predictions that use the exact initial crack size yield significantly more accurate results, with errors typically ranging from 5% to 20%. In both scenarios, prediction errors increased in the later stages of fatigue life. This increase is likely due to the limitations of the selected model (e.g., the Paris-Erdogan relation) in capturing the crack growth process. On the one hand, the crack growth model employed has inherent limitations in capturing all aspects of the fatigue process. On the other hand, more sophisticated models that attempt to address these limitations can become highly complex and computationally demanding. Therefore, a practical balance must be struck: selecting a model that is sufficiently simple for practical use, yet accurately calibrated - potentially using data from field tests on real cracks in mooring chains - to ensure reliable fatigue life predictions.

Overall, the results demonstrate the potential of remote AE monitoring for crack growth prognosis in submerged steel mooring chains.

5

Conclusions & Outlook

5 CONCLUSIONS & OUTLOOK

This thesis lays the foundation for enhanced Digital Twins (DTs) for offshore mooring chains, enabling informed decision-making through real-time monitoring and predictive analysis. Accurate and quantitative integrity assessment techniques are essential to ensure the reliability of DTs and the quality of the measurement data they depend on. A review of the prior art has highlighted the lack of in-water inspection techniques for mooring chains that do not require the removal of marine growth.

To address this gap, the thesis proposed a novel approach using non-contact Acoustic Emission (AE) monitoring in underwater environments. This method overcomes the limitations of conventional techniques, which typically require direct sensor contact with the structure. A methodology is proposed for enhancing DTs through non-intrusive, non-destructive diagnosis and prognosis of corrosion-fatigue damage. This enables structural integrity assessments without the need for surface cleaning. Additionally, the approach supports remote operation and real-time monitoring, reducing dependence on manual inspections in challenging offshore conditions.

5.1 CONCLUSIONS

Chapter 2 addressed the detectability of corrosion-fatigue damage by underwater non-contact AE monitoring using small-scale corrosion-fatigue experiments. The results of experiments highlighted the feasibility of the proposed monitoring approach. Corrosion-fatigue-induced ultrasound signals were detected with a satisfactory signal-to-noise ratio using non-contact AE sensors (in the frequency range of 50–450 kHz). Cumulative (and rate) values of AE parameters showed a good representation of damage progression, identifying four stages of damage evolution. AE energy was the most promising indicator of damage evolution, particularly highlighting crack formation and rapid growth stages. Additionally, corrosion-fatigue-induced signals were characterised by a mean energy of

approximately one order of magnitude higher than corrosion-induced ones. In the experiment, the corrosion mechanism induced a significantly lower number of ultrasound signals than corrosion-fatigue. In another experiment, simulated crack signals were measured on two steel plates (with and without marine growth). This suggests that the ultrasound waves can penetrate the marine growth (artificially-fabricated) and can be successfully detected using non-contact AE transducers in submerged conditions. A maximum 12dB drop in signal amplitude can be expected due to artificial-made marine growth.

Chapter 3 presented the feasibility of constructing a diagnostic DT through detection, localisation, and monitoring corrosion and fatigue damage in mooring chain links using underwater remote AE in large-scale experiments. The studies demonstrated the effectiveness of the proposed approach in detecting, localising, and monitoring growing damage. Parametrisation of the AE measurements effectively monitored the acoustic activity induced by the initiation and growth of corrosion-fatigue damage. A 3D source localisation algorithm for damage-induced ultrasound signals was successfully implemented, and the results were projected on the 3D geometry of the chain segment in the form of DT. In the fatigue test, the AE-based DT revealed three distinct zones of acoustic activity, which correlated well with the post-failure inspection. All the locations where indications were found through MP testing were detected and localised using the remote AE technique.

Building upon the experimental findings of Chapter 3, the feasibility of crack growth prognosis in submerged mooring chains using remote AE monitoring was assessed in Chapter 4. A prognosis model based on the Paris relation and AE energy was proposed, and its predictive capabilities were quantified. The results demonstrated the potential of remote AE monitoring for fatigue crack growth prognosis in submerged mooring chains. The analysis of AE energy at different test stages confirmed distinct phases of crack growth, including initiation, stable propagation, and acceleration toward failure. The results of the prognosis model highlighted the characteristic stages of crack growth, as suggested by the AE energy rate. A

sensitivity analysis on the influence of model parameters showed that reducing B leads to overestimated crack growth and shorter predicted fatigue life, whereas increasing B results in underestimated crack growth and longer predicted fatigue life. The choice of p ($m + 1$, $m + 2$, and $m + 3$) magnifies these effects, with $p = m + 1$ and $p = m + 3$ producing substantially larger and smaller crack depth predictions, respectively. Finally, fatigue life predictions highlighted the importance of incorporating an accurate initial crack size and using appropriate crack growth models.

This thesis leads to the following high-level conclusions:

- Underwater arrays of non-contact AE transducers can measure corrosion- and corrosion-fatigue-induced ultrasound signals at distances of 100-300 mm from the source. The proposed approach detected damage-induced signals with a signal-to-noise ratio of about 10-20 dB in the laboratory environment.
- It is feasible to measure AE through layers of marine growth. Experiments demonstrated a 12 dB amplitude drop for a 15 ± 5 mm fabricated layer of marine growth.
- Damage-induced AE sources can be localised on the geometry of the underwater chain links with an accuracy of a few centimetres using underwater arrays of non-contact AE transducers. Making use of 3D scans of the chain links, the proposed approach can effectively map the damage-induced AE source locations on the geometry of the underwater chain links.
- AE data can be integrated with fatigue models to enhance a digital twin with predictive capabilities for damage prognosis. By correlating AE energy rates with crack growth models like the Paris relation, distinct crack growth phases can be identified. The fatigue life prediction accuracy can be

improved when incorporating precise initial crack sizes and refined model parameters.

5.2 RECOMMENDATIONS

While the research addressed the main and sub-objectives, new topics and questions have arisen leading to the following recommendations for future research:

- Conducting further detailed small-scale experiments under different mechanical and electrochemical, and marine biological conditions to extend the conclusions of this thesis.
- Developing a more rigorous characterisation framework for AE signals based on waveform signature and their features.
- Performing further assessments of modelling parameters and exploring crack sizing using AE data (combined with crack growth models) to enhance the accuracy of crack growth prognosis and improve fatigue life predictions.
- Transitioning from laboratory testing to offshore conditions to demonstrate the approach under realistic environmental scenarios.

Bibliography

- [1] “Energy Transition Outlook 2024: A global and regional forecast to 2050”, DNV, 2024. <https://www.dnv.com/publications/energy-transition-outlook-2024/>
- [2] “Floating Offshore Wind - SBM Offshore,” *SBM Offshore*, Sep. 12, 2024. <https://www.sbmoffshore.com/what-we-do/floating-offshore-wind>
- [3] “FPSO & Operations - SBM Offshore,” *SBM Offshore*, Oct. 10, 2024. <https://www.sbmoffshore.com/what-we-do/fpso-operations>
- [4] Á. Angulo, G. Edwards, S. Soua, and T.-H. Gan, “Mooring Integrity Management: Novel Approaches towards in situ monitoring,” in *InTech eBooks*, 2017. doi: 10.5772/intechopen.68386.
- [5] M. G. Brown, T. D. Hall, D. G. Marr, M. English, and R. O. Snell, “Floating Production Mooring Integrity JIP - Key Findings,” *Offshore Technology Conference*, Jan. 2005, doi: 10.4043/17499-ms.
- [6] I. Milne, R. O. Ritchie, and B. L. Karihaloo, *Comprehensive structural integrity*. 2023. doi: 10.1016/c2010-1-66646-1.
- [7] A. Dumont and A. Vagata, “SuBSeA 3D video survey of mooring chains - Improving safety, effectiveness and efficiency,” *Offshore Technology Conference Brasil*, Oct. 2023, doi: 10.4043/32956-ms.
- [8] E. Fontaine, A. Kilner, C. Carra, D. Washington, K. T. Ma, A. Phadke, and G. Kusinski, “Industry survey of past failures, pre-emptive replacements and reported degradations for mooring systems of floating production units,” *Offshore Technology Conference*, May 2014.

- [9] K. T. Ma, H. Shu, P. Smedley, D. L’Hostis, and A. Duggal, “A historical review on integrity issues of permanent mooring systems,” *Offshore Technology Conference*, May 2013.
- [10] M. Grieves and J. Vickers, “Digital Twin: mitigating unpredictable, undesirable emergent behavior in complex systems,” in *Springer eBooks*, 2016, pp. 85–113. doi: 10.1007/978-3-319-38756-7_4.
- [11] D. M. Botín-Sanabria, A. S. Mihaita, R. E. Peimbert-García, M. A. Ramírez-Moreno, R. A. Ramírez-Mendoza, and J. D. J. Lozoya-Santos, “Digital twin technology challenges and applications: A comprehensive review,” *Remote Sensing*, vol. 14, no. 6, p. 1335, 2022. doi: 10.3390/rs14061335.
- [12] M. Javaid, A. Haleem, and R. Suman, “Digital twin applications toward industry 4.0: A review,” *Cognitive Robotics*, vol. 3, pp. 71–92, 2023. doi: 10.1016/j.cogr.2023.03.002.
- [13] S. Mihai *et al.*, “Digital Twins: a survey on enabling technologies, challenges, trends and future prospects,” *IEEE Communications Surveys & Tutorials*, vol. 24, no. 4, pp. 2255–2291, Jan. 2022, doi: 10.1109/comst.2022.3208773.
- [14] S. Li and F. Brennan, “Digital twin enabled structural integrity management: Critical review and framework development,” *Proceedings of the Institution of Mechanical Engineers Part M Journal of Engineering for the Maritime Environment*, Jan. 2024, doi: 10.1177/14750902241227254.
- [15] S. Matsumoto, V. Jaiswal, T. Sugimura, S. Honjo, and P. Szalewski, “Mooring Integrity Management through Digital Twin and Standardized Inspection Data,” *Offshore Technology Conference*, Aug. 2021, doi: 10.4043/31036-ms.

-
- [16] G. Rangel *et al.*, “Methodology for obtaining a digital twin for a FPSO mooring system,” *Proceedings of the 26th International Congress of Mechanical Engineering*, Jan. 2021, doi: 10.26678/abcm.cobem2021.cob2021-0749.
- [17] S. Pedersen, J. Liniger, F. F. Sorensen, and M. Von Benzon, “On marine growth removal on offshore structures,” *OCEANS 2022 - Chennai*, pp. 1–6, Feb. 2022, doi: 10.1109/oceanschennai45887.2022.9775498.
- [18] “FlexiCleanTM.” <https://stoprust.com/products-and-services/flexiclean>
- [19] J. P. Assaker, “Underwater inspection of fixed offshore steel structures,” *IUMI Eye Newsletter*, Sep. 2020. <https://iumi.com/news/iumieye-newsletter-september-2020/underwater-inspection-of-fixed-offshore-steel-structures>
- [20] A. Technology, “Accurate mooring chain inspections - Ashtead Technology,” *Ashtead Technology*, May 01, 2023. <https://www.ashtead-technology.com/case-study/accurate-mooring-chain-inspections>
- [21] Acteon Group Ltd, “Mooring inspection, maintenance, repair and replacement - Acteon,” *Acteon*, Aug. 30, 2024. <https://acteon.com/specialisms/mooring-inspection-maintenance-repair-and-replacement>
- [22] P. Rizzo, “NDE/SHM of Underwater Structures: A review,” *Advances in Science and Technology*, Sep. 2012, doi: 10.4028/www.scientific.net/ast.83.208.
- [23] S. Caines, F. Khan, and J. Shirokoff, “Analysis of pitting corrosion on steel under insulation in marine environments,” *Journal of Loss Prevention in the Process Industries*, vol. 26, no. 6, pp. 1466–1483, Oct. 2013, doi: 10.1016/j.jlp.2013.09.010.

- [24] D. S. Forsyth, “Non-destructive testing for corrosion,” in *Corrosion Fatigue and Environmentally Assisted Cracking in Aging Military Vehicles*, RTO-AG-AVT-140, 2011.
- [25] J. Bhandari, F. Khan, R. Abbassi, V. Garaniya, and R. Ojeda, “Modelling of pitting corrosion in marine and offshore steel structures – A technical review,” *Journal of Loss Prevention in the Process Industries*, vol. 37, pp. 39–62, 2015. doi: 10.1016/j.jlp.2015.06.008.
- [26] N. A. Zawawi, M. S. Liew, W. S. Alaloul, L. E. Shawn, M. Imran, and I. Toloue, “Non-destructive testing techniques for offshore underwater decommissioning projects through cutting detection: a state of review,” *SPE Symposium: Decommissioning and Abandonment*, OnePetro, 2019. doi: 10.2118/199191-MS.
- [27] “Underwater inspection services.”
https://fairtexgroups.com/under_water_inspection.php
- [28] “NDT inspection of mooring chain links.” <https://www.twi-global.com/media-and-events/insights/ndt-inspection-of-mooring-chain-links>
- [29] “Seaocean Diving & Marine Services.” <https://seaoceandiving.com/>
- [30] J. Rudlin, “Multi-channel ultrasonic inspection of a mooring chain for fatigue cracks,” in *European Conference on Non-Destructive Testing*, Prague, Czech Republic, 2014.
- [31] W. Qian, S. Wu, L. Lei, Q. Hu, and C. Liu, “Time lapse in situ X-ray imaging of failure in structural materials under cyclic loads and extreme environments,” *Journal of Material Science and Technology*, vol. 175, pp. 80–103, Sep. 2023, doi: 10.1016/j.jmst.2023.07.041.

-
- [32] T. J. Stannard, J. J. Williams, S. S. Singh, A. S. S. Singaravelu, X. Xiao, and N. Chawla, “3D time-resolved observations of corrosion and corrosion-fatigue crack initiation and growth in peak-aged Al 7075 using synchrotron X-ray tomography,” *Corrosion Science*, vol. 138, pp. 340–352, Apr. 2018, doi: 10.1016/j.corsci.2018.04.029.
- [33] E. Cheilakou, N. Tsopelas, T. Brashaw, A. Anastasopoulos, I. Nicholson, A. Clarke, and M. Corsar, “Digital radiography inspection of flexible risers in offshore oil and gas industry,” in *International Conference on Welding and Non Destructive Testing*, Oct. 2018.
- [34] “Successful field trials of underwater-inspection system.” <https://www.twi-global.com/media-and-events/press-releases/2018/field-trials-of-new-digital-radiography-based-underwater-inspection-system-hailed-a-success>
- [35] M. Journal, “Mooring chain laser inspection,” *Maritime Journal*, Sep. 08, 2022. <https://www.maritimejournal.com/mooring-chain-laser-inspection/1195115.article>
- [36] L. Calabrese and E. Proverbio, “A review on the applications of acoustic emission technique in the study of stress corrosion cracking,” *Corrosion and Materials Degradation*, vol. 2, no. 1, pp. 1–30, 2020. doi: 10.3390/cmd2010001.
- [37] B. Scheeren, M. L. Kaminski, and L. Pahlavan, “Evaluation of ultrasonic stress wave transmission in cylindrical roller bearings for acoustic emission condition monitoring,” *Sensors*, vol. 22, no. 4, p. 1500, Feb. 2022, doi: 10.3390/s22041500.
- [38] A. Huijter, C. Kassapoglou, and L. Pahlavan, “Acoustic Emission Monitoring of Carbon Fibre Reinforced Composites with Embedded Sensors for In-Situ Damage Identification,” *Sensors*, vol. 21, no. 20, p. 6926, Oct. 2021, doi: 10.3390/s21206926.

- [39] C. Van Steen, L. Pahlavan, M. Wevers, and E. Verstrynge, “Localisation and characterisation of corrosion damage in reinforced concrete by means of acoustic emission and X-ray computed tomography,” *Construction and Building Materials*, vol. 197, pp. 21–29, Nov. 2018, doi: 10.1016/j.conbuildmat.2018.11.159.
- [40] C. U. Grosse and M. Ohtsu, *Acoustic emission testing*. 2008. doi: 10.1007/978-3-540-69972-9.
- [41] S. Yuyama, T. Kishi, and Y. Hisamatsu, “Fundamental aspects of AE monitoring on corrosion fatigue processes in austenitic stainless steel,” *Journal of Materials for Energy Systems*, vol. 5, no. 4, pp. 212–221, Mar. 1984, doi: 10.1007/bf02835719.
- [42] M. Chai, C. Lai, W. Xu, Q. Duan, Z. Zhang, and Y. Song, “Characterization of fatigue crack growth based on Acoustic Emission Multi-Parameter analysis,” *Materials*, vol. 15, no. 19, p. 6665, Sep. 2022, doi: 10.3390/ma15196665.
- [43] M. Chai, X. Hou, Z. Zhang, and Q. Duan, “Identification and prediction of fatigue crack growth under different stress ratios using acoustic emission data,” *International Journal of Fatigue*, vol. 160, p. 106860, Mar. 2022, doi: 10.1016/j.ijfatigue.2022.106860.
- [44] M. Chai, J. Zhang, Z. Zhang, Q. Duan, and G. Cheng, “Acoustic emission studies for characterization of fatigue crack growth in 316LN stainless steel and welds,” *Applied Acoustics*, vol. 126, pp. 101–113, May 2017, doi: 10.1016/j.apacoust.2017.05.014.
- [45] H. Chang, E. Han, J. Q. Wang, and W. Ke, “Acoustic emission study of corrosion fatigue crack propagation mechanism for LY12CZ and 7075-T6 aluminum alloys,” *Journal of Materials Science*, vol. 40, no. 21, pp. 5669–5674, Aug. 2005, doi: 10.1007/s10853-005-1300-9.

- [46] H. Chang, “Acoustic Emission Study of Corrosion Fatigue Crack Propagation Mechanism Identification,” *Applied Mechanics and Materials*, vol. 628, pp. 20–23, Sep. 2014, doi: 10.4028/www.scientific.net/amm.628.20.
- [47] W. Hwang, S. Bae, J. Kim, S. Kang, N. Kwag, and B. Lee, “Acoustic emission characteristics of stress corrosion cracks in a type 304 stainless steel tube,” *Nuclear Engineering and Technology*, vol. 47, no. 4, pp. 454–460, Apr. 2015, doi: 10.1016/j.net.2015.04.001.
- [48] L. Calabrese, L. Bonaccorsi, M. Galeano, E. Proverbio, D. Di Pietro, and F. Cappuccini, “Identification of damage evolution during SCC on 17-4 PH stainless steel by combining electrochemical noise and acoustic emission techniques,” *Corrosion Science*, vol. 98, pp. 573–584, Jun. 2015, doi: 10.1016/j.corsci.2015.05.063.
- [49] H. Bi *et al.*, “Evaluation of the acoustic emission monitoring method for stress corrosion cracking on aboveground storage tank floor steel,” *International Journal of Pressure Vessels and Piping*, vol. 179, p. 104035, Dec. 2019, doi: 10.1016/j.ijpvp.2019.104035.
- [50] D. G. Aggelis, E. Z. Kordatos, and T. E. Matikas, “Acoustic emission for fatigue damage characterization in metal plates,” *Mechanics Research Communications*, vol. 38, no. 2, pp. 106–110, Jan. 2011, doi: 10.1016/j.mechrescom.2011.01.011.
- [51] G. Du, J. Li, W. K. Wang, C. Jiang, and S. Z. Song, “Detection and characterization of stress-corrosion cracking on 304 stainless steel by electrochemical noise and acoustic emission techniques,” *Corrosion Science*, vol. 53, no. 9, pp. 2918–2926, May 2011, doi: 10.1016/j.corsci.2011.05.030.

- [52] H. Chang, "Identification of damage mode in AZ31 magnesium alloy under tension using acoustic emission," *Transactions of Nonferrous Metals Society of China*, vol. 25, no. 6, pp. 1840–1846, Jun. 2015, doi: 10.1016/s1003-6326(15)63790-6.
- [53] V. R. Skals'kyi, Z. T. Nazarchuk, I. Ya. Dolins'ka, R. Ya. Yarema, and T. V. Selivonchuk, "Acoustic-Emission Diagnostics of corrosion Defects in materials (A survey). Part. 1. Detection of electrochemical corrosion and corrosion fatigue," *Materials Science*, vol. 53, no. 3, pp. 295–305, Nov. 2017, doi: 10.1007/s11003-017-0075-x.
- [54] Z. Han, H. Luo, J. Cao, and H. Wang, "Acoustic emission during fatigue crack propagation in a micro-alloyed steel and welds," *Materials Science and Engineering A*, vol. 528, no. 25–26, pp. 7751–7756, Jul. 2011, doi: 10.1016/j.msea.2011.06.065.
- [55] L. Li, Z. Zhang, and G. Shen, "Influence of grain size on fatigue crack propagation and acoustic emission features in commercial-purity zirconium," *Materials Science and Engineering A*, vol. 636, pp. 35–42, Apr. 2015, doi: 10.1016/j.msea.2015.03.046.
- [56] M. Fregonese, H. Idrissi, H. Mazille, L. Renaud, and Y. Cetre, "Initiation and propagation steps in pitting corrosion of austenitic stainless steels: monitoring by acoustic emission," *Corrosion Science*, vol. 43, no. 4, pp. 627–641, Apr. 2001, doi: 10.1016/s0010-938x(00)00099-8.
- [57] C. Jirarungsatien and A. Prateepasen, "Pitting and uniform corrosion source recognition using acoustic emission parameters," *Corrosion Science*, vol. 52, no. 1, pp. 187–197, Sep. 2009, doi: 10.1016/j.corsci.2009.09.001.

-
- [58] F. G. Rivera, G. Edwards, E. Eren, and S. Soua, “Acoustic emission technique to monitor crack growth in a mooring chain,” *Applied Acoustics*, vol. 139, pp. 156–164, May 2018, doi: 10.1016/j.apacoust.2018.04.034.
- [59] Á. Angulo, J. Tang, A. Khadimallah, S. Soua, C. Mares, and T.-H. Gan, “Acoustic emission monitoring of fatigue crack growth in mooring chains,” *Applied Sciences*, vol. 9, no. 11, p. 2187, May 2019, doi: 10.3390/app9112187.
- [60] F. Ferrer, T. Faure, J. Goudiakas, and E. Andrès, “Acoustic emission study of active–passive transitions during carbon steel erosion–corrosion in concentrated sulfuric acid,” *Corrosion Science*, vol. 44, no. 7, pp. 1529–1540, Jul. 2002, doi: 10.1016/s0010-938x(01)00148-2.
- [61] L. Pahlavan, J. Paulissen, R. Pijpers, *et al.*, “Acoustic emission health monitoring of steel bridges,” in *EWSHM – 7th European Workshop on Structural Health Monitoring*, Nantes, France, July 2014.
- [62] J. Krautkrämer and H. Krautkrämer, *Ultrasonic testing of materials*. 1983. doi: 10.1007/978-3-662-02357-0.
- [63] L. E. Kinsler, A. R. Frey, and G. S. Bennett, “Fundamentals of Acoustics,” *American Journal of Physics*, vol. 19, no. 4, pp. 254–255, Apr. 1951, doi: 10.1119/1.1932798.
- [64] B. Scheeren, M. L. Kaminski, and L. Pahlavan, “Acoustic emission monitoring of naturally developed damage in large-scale low-speed roller bearings,” *Structural Health Monitoring*, vol. 23, no. 1, pp. 360–382, May 2023, doi: 10.1177/14759217231164912.
- [65] R. M. Meyer, A. F. Pardini, B. D. Hanson, and K. B. Sorenson, “Review of NDE methods for detection and monitoring of atmospheric SCC in welded

- canisters for the storage of used nuclear fuel,” Jan. 2013. doi: 10.2172/1183636.
- [66] S. Nuthalapati, K. E. Kee, S. R. Pedapati, and K. Jumbri, “A review of chloride induced stress corrosion cracking characterization in austenitic stainless steels using acoustic emission technique,” *Nuclear Engineering and Technology*, 2023. doi: 10.1016/j.net.2023.11.005.
- [67] ASTM E8/E8M-22, *Standard test methods for tension testing of metallic materials*, American Society for Testing and Materials, West Conshohocken, PA, USA, 2022.
- [68] S. Alkhateeb, F. Riccioli, F. L. Morales, and L. Pahlavan, “Non-Contact Acoustic Emission Monitoring of Corrosion under Marine Growth,” *Sensors*, vol. 23, no. 1, p. 161, Dec. 2022, doi: 10.3390/s23010161.
- [69] ASTM E976-15, *Standard guide for determining the reproducibility of acoustic emission sensor response*, American Society for Testing and Materials, West Conshohocken, PA, USA, 2015.
- [70] E. Cruz, T. Lloyd, J. Bosschers, F. H. Lafeber, P. Vinagre, and G. Vaz, “Study on Inventory of Existing Policy, Research and Impacts of Continuous Underwater Noise in Europe,” WavEC Offshore Renewables and Maritime Research Institute Netherlands, EMSA report EMSA/NEG/21/2020, 2021.
- [71] L.-F. Huang, X.-M. Xu, L.-L. Yang, S.-Q. Huang, X.-H. Zhang, and Y.-L. Zhou, “Underwater noise characteristics of offshore exploratory drilling and its impact on marine mammals,” *Frontiers in Marine Science*, vol. 10, Feb. 2023, doi: 10.3389/fmars.2023.1097701.

-
- [72] G. Jimenez-Arranz, N. Banda, S. Cook, and R. Wyatt, “Review of Existing Data on Underwater Sounds Produced by the Oil and Gas Industry,” JIP Topic – Sound Source Characterisation and Propagation, 2020.
- [73] DNVGL-OS-E301, *Position Mooring*, Offshore Standards, 2018.
- [74] J. Yu, P. Ziehl, B. Zárate, and J. Caicedo, “Prediction of fatigue crack growth in steel bridge components using acoustic emission,” *Journal of Constructional Steel Research*, vol. 67, no. 8, pp. 1254–1260, Apr. 2011, doi: 10.1016/j.jcsr.2011.03.005.
- [75] P. L. Schmidt, J. K. Nelson, R. G. Handy, J. S. Morrell, M. J. Jackson, and T. M. Rees, “Noncontact measurements of acoustic emissions from the single-point turning process,” *The International Journal of Advanced Manufacturing Technology*, vol. 93, no. 9–12, pp. 3907–3920, Jul. 2017, doi: 10.1007/s00170-017-0756-5.
- [76] P. Sutowski, K. Nadolny, and W. Kaplonek, “Monitoring of cylindrical grinding processes by use of a non-contact AE system,” *International Journal of Precision Engineering and Manufacturing*, vol. 13, no. 10, pp. 1737–1743, Sep. 2012, doi: 10.1007/s12541-012-0228-7.
- [77] W. Xiao and L. Yu, “Non-contact passive sensing of acoustic emission signal using the air-coupled transducer,” *Health Monitoring of Structural and Biological Systems XV*, vol. 11593, p. 12–419, 2021. doi: 10.1117/12.2583218.
- [78] T. Matsuo and D. Hatanaka, “Development of Non-Contact Fatigue crack propagation Monitoring method using Air-Coupled Acoustic Emission System,” *Engineering Transactions*, vol. 67, no. 2, pp. 185–198, Apr. 2019, doi: 10.24423/engtrans.1009.20190405.

- [79] A. Terchi and Y. H. J. Au, “Acoustic emission signal processing,” *Measurement and Control*, vol. 34, no. 8, pp. 240–244, Oct. 2001, doi: 10.1177/002029400103400804.
- [80] M. Ohtsu, M. Enoki, Y. Mizutani, and M. Shigeishi, “Principles of the acoustic emission (AE) method and signal processing,” in *Springer eBooks*, 2016, pp. 5–34. doi: 10.1007/978-4-431-55072-3_2.
- [81] T. Kundu, “Acoustic source localization,” *Ultrasonics*, vol. 54, no. 1, pp. 25–38, 2014. doi: 10.1016/j.ultras.2013.06.009.
- [82] H. Akaike, “Markovian representation of stochastic processes and its application to the analysis of autoregressive moving average processes,” *Annals of the Institute of Statistical Mathematics*, vol. 26, no. 1, pp. 363–387, Dec. 1974, doi: 10.1007/bf02479833.
- [83] J. H. Kurz, C. U. Grosse, and H.-W. Reinhardt, “Strategies for reliable automatic onset time picking of acoustic emissions and of ultrasound signals in concrete,” *Ultrasonics*, vol. 43, no. 7, pp. 538–546, Dec. 2004, doi: 10.1016/j.ultras.2004.12.005.
- [84] “Vallen Systeme,” *Vallen Systeme*, Jul. 20, 2023. <https://www.vallen.de/>
- [85] R. Pullin, M. J. Eaton, J. J. Hensman, K. M. Holford, K. Worden, and S. L. Evans, “Validation of acoustic emission (AE) crack detection in aerospace grade steel using digital image correlation,” *Applied Mechanics and Materials*, vol. 24–25, pp. 221–226, Jun. 2010, doi: 10.4028/www.scientific.net/amm.24-25.221.
- [86] D. O. Gagar, “Validation and verification of the acoustic emission technique for structural health monitoring,” 2013. [Online]. Available: https://dspace.lib.cranfield.ac.uk/bitstream/1826/8402/1/Gagar_D_O_Thesis_2013.pdf

-
- [87] F. Riccioli, Ø. Gabrielsen, I. S. Høgsæt, P. S. Barros, and L. Pahlavan, “Corrosion-fatigue damage identification in submerged mooring chain links using remote acoustic emission monitoring,” *Marine Structures*, vol. 98, p. 103685, Aug. 2024, doi: 10.1016/j.marstruc.2024.103685.
- [88] J. Yu and P. Ziehl, “Stable and unstable fatigue prediction for A572 structural steel using acoustic emission,” *Journal of Constructional Steel Research*, vol. 77, pp. 173–179, Jun. 2012, doi: 10.1016/j.jcsr.2012.05.009.
- [89] A. Keshtgar, C. M. Sauerbrunn, and M. Modarres, “Structural reliability prediction using acoustic Emission-Based modeling of fatigue crack growth,” *Applied Sciences*, vol. 8, no. 8, p. 1225, Jul. 2018, doi: 10.3390/app8081225.
- [90] D. Li, K. S. C. Kuang, and C. G. Koh, “Fatigue crack sizing in rail steel using crack closure-induced acoustic emission waves,” *Measurement Science and Technology*, vol. 28, no. 6, p. 065601, Apr. 2017, doi: 10.1088/1361-6501/aa670d.
- [91] D. O. Harris and H. L. Dunegan, “Continuous monitoring of fatigue-crack growth by acoustic-emission techniques,” *Experimental Mechanics*, vol. 14, no. 2, pp. 71–81, Feb. 1974, doi: 10.1007/bf02323130.
- [92] T. C. Lindley, I. G. Palmer, and C. E. Richards, “Acoustic emission monitoring of fatigue crack growth,” *Materials Science and Engineering*, vol. 32, no. 1, pp. 1–15, Jan. 1978, doi: 10.1016/0025-5416(78)90206-9.
- [93] A. C. E. Sinclair, D. C. Connors, and C. L. Formby, “Acoustic emission analysis during fatigue crack growth in steel,” *Materials Science and Engineering*, vol. 28, no. 2, pp. 263–273, May 1977, doi: 10.1016/0025-5416(77)90180-x.

- [94] T. M. Roberts and M. Talebzadeh, "Acoustic emission monitoring of fatigue crack propagation," *Journal of Constructional Steel Research*, vol. 59, no. 6, pp. 695–712, Mar. 2003, doi: 10.1016/s0143-974x(02)00064-0.
- [95] S. Shi *et al.*, "Quantitative monitoring of brittle fatigue crack growth in railway steel using acoustic emission," *Proceedings of the Institution of Mechanical Engineers Part F Journal of Rail and Rapid Transit*, vol. 232, no. 4, pp. 1211–1224, Jun. 2017, doi: 10.1177/0954409717711292.
- [96] J. Xu *et al.*, "Study on acoustic emission properties and crack growth rate identification of rail steels under different fatigue loading conditions," *International Journal of Fatigue*, vol. 172, p. 107638, Mar. 2023, doi: 10.1016/j.ijfatigue.2023.107638.
- [97] Z. Zhang, G. Yang, and K. Hu, "Prediction of fatigue crack growth in gas turbine engine blades using acoustic emission," *Sensors*, vol. 18, no. 5, p. 1321, Apr. 2018, doi: 10.3390/s18051321.
- [98] M. Chai, Z. Zhang, and Q. Duan, "A new qualitative acoustic emission parameter based on Shannon's entropy for damage monitoring," *Mechanical Systems and Signal Processing*, vol. 100, pp. 617–629, Sep. 2017, doi: 10.1016/j.ymssp.2017.08.007.
- [99] M. Chai, Z. Zhang, Q. Duan, and Y. Song, "Assessment of fatigue crack growth in 316LN stainless steel based on acoustic emission entropy," *International Journal of Fatigue*, vol. 109, pp. 145–156, Jan. 2018, doi: 10.1016/j.ijfatigue.2017.12.017.
- [100] A. A. Griffith, "VI. The phenomena of rupture and flow in solids," *Philosophical Transactions of the Royal Society of London Series A Containing Papers of a Mathematical or Physical Character*, vol. 221, no. 582–593, pp. 163–198, Jan. 1921, doi: 10.1098/rsta.1921.0006.

-
- [101] P. Paris and F. Erdogan, “A critical analysis of crack propagation laws,” *Journal of Basic Engineering*, vol. 85, no. 4, pp. 528–533, Dec. 1963, doi: 10.1115/1.3656900.
- [102] T. L. Anderson, *Fracture mechanics : fundamentals and applications*. 1995.
- [103] I. M. Daniel, J. -j. Luo, C. G. Sifniotopoulos, and H. -j. Chun, “Acoustic emission monitoring of fatigue damage in metals,” *Nondestructive Testing and Evaluation*, vol. 14, no. 1–2, pp. 71–87, Jan. 1998, doi: 10.1080/10589759808953043.
- [104] T. M. Roberts and M. Talebzadeh, “Fatigue life prediction based on crack propagation and acoustic emission count rates,” *Journal of Constructional Steel Research*, vol. 59, no. 6, pp. 679–694, Mar. 2003, doi: 10.1016/s0143-974x(02)00065-2.
- [105] M. Aursand, G. T. Frøseth, P. J. Haagenzen, and B. H. Skallerud, “Crack growth in high strength mooring line steel under variable amplitude loading,” *Marine Structures*, vol. 93, p. 103534, Oct. 2023, doi: 10.1016/j.marstruc.2023.103534.
- [106] M. Aursand, P. J. Haagenzen, and B. H. Skallerud, “Remaining fatigue life assessment of corroded mooring chains using crack growth modelling,” *Marine Structures*, vol. 90, p. 103446, May 2023, doi: 10.1016/j.marstruc.2023.103446.
- [107] Ø. Gabrielsen, S. A. Reinholdtsen, B. Skallerud, *et al.*, “Fatigue capacity of used mooring chain – results from full scale fatigue testing at different mean loads,” in *International Conference on Offshore Mechanics and Arctic Engineering*, Hamburg, Germany, June 5–8, 2022, paper no. OMAE2022-79649, V001T01A030.

- [108] V. Hellum, Ø. Gabrielsen, and S. K. Ås, “Fatigue crack growth in mooring chain steel at different mean load levels,” *Marine Structures*, vol. 92, p. 103507, Aug. 2023, doi: 10.1016/j.marstruc.2023.103507.
- [109] C. M. Rizzo, “Application of reliability analysis to the fatigue of typical welded joints of ships,” *Ship Technology Research*, vol. 54, no. 2, pp. 89–100, Apr. 2007, doi: 10.1179/str.2007.54.2.004.
- [110] Z. Wang, K. Wang, Q. Han, J. Ni, and Z. Wu, “Crack imaging of underwater concrete components using interfacial waves and transducer array,” *Mechanical Systems and Signal Processing*, vol. 224, p. 111998, Oct. 2024, doi: 10.1016/j.ymssp.2024.111998.
- [111] F. Carere, A. Sardellitti, A. Bernieri, L. Ferrigno, S. Sangiovanni, and M. Laracca, “An Eddy current probe for the detection of subsuperficial defects of any orientation,” *IEEE Transactions on Instrumentation and Measurement*, vol. 73, pp. 1–13, Jan. 2024, doi: 10.1109/tim.2024.3395324.
- [112] X. Yuan *et al.*, “A flexible alternating current field measurement magnetic sensor array for in situ inspection of cracks in underwater structure,” *IEEE Transactions on Instrumentation and Measurement*, vol. 73, pp. 1–10, Jan. 2024, doi: 10.1109/tim.2024.3383056.
- [113] J. Xin *et al.*, “A crack characterization model for subsea pipeline based on spatial magnetic signals features,” *Ocean Engineering*, vol. 274, p. 114112, Mar. 2023, doi: 10.1016/j.oceaneng.2023.114112.
- [114] Y. Li *et al.*, “Vision-guided crack identification and size quantification framework for dam underwater concrete structures,” *Structural Health Monitoring*, Nov. 2024, doi: 10.1177/14759217241287906.

- [115] BS 7910:2019, *Guide to methods for assessing the acceptability of flaws in metallic structures*, British Standards Institution, 2019.
- [116] C. M. Rizzo and E. Ayala-Uraga, “Fatigue crack growth assessment of welded joints in ship structures: a reliability based sensitivity study,” in *Proceedings of the 25th International Conference on Offshore Mechanics and Arctic Engineering (OMAE06)*, Hamburg, Germany, June 2006, paper OMAE2006-92136, ISBN 0-7918-4748-9.

Acknowledgements

Completing this thesis would not have been possible without the support, guidance, and contributions of many individuals. For all the lessons, encouragement, and help I have received along the way, I wish to express my sincere and genuine gratitude.

To the PhD committee members, for carefully reading and critically assessing the work presented in this thesis.

To the Donut JIP project partners, for the fruitful collaborations and invaluable support that made the project a success.

To the co-authors of all the scientific publications, for the shared effort, feedback, and stimulating discussions that strengthened the research.

To Pooria, for his guidance, mentorship, and friendship.

To Bart, Arno, Maarten, Cecilia, and Romain, for the invaluable exchange of ideas, practical collaborations, and generous support in both experimental and analytical challenges.

To Jacob, Martin, Hugo, Mohammed, Wei Jun, Ruben, Bram, Niels, Punya, Leonard, and Nikolaos, for the daily exchanges, encouragement, and kindness that made the work environment both productive and enjoyable.

To Peter, for his friendship and discreet guidance.

To Rakesh, for his prompt help, patience, and practical support.

To TU Delft ME Faculty and M&TT Department technical and management staff, for providing excellent technical support and creating the conditions that allowed me to focus on my research and complete this PhD successfully.

Acknowledgements

To Gabriele and Vittorio, for always looking out for me and supporting me through this journey.

To Stella, Edoardo, Irene, Irene, Marcello, Renske, Justus, Charlie, Marco, Quito, Alessia, Federico, and Francesco, for the countless memorable moments we shared over these years.

To Giovanni and Rosa Maria, for their daily inspiration and unconditional love.

To Edoardo, for showing me the true value of family.

To Ida, for her love, patience, and continuous participation in this journey.

Thank you.

Curriculum vitae

Personal Data

31-03-1994 Born in Carate Brianza, Milano, Italy.

Education

2022-2025 Ph.D. research
Department of Maritime and Transport Technology
Delft University of Technology, Delft, The Netherlands
Thesis: A Digital Twin for Offshore Mooring
Chains based on Acoustic Emission
Monitoring
Promoters: Prof.dr.ir. B.J. Boersma
Dr. L. Pahlavan

2017-2020 M.Sc. study with honors
Naval Engineering (Yacht Design)
University of Genova, La Spezia, Italy

2016-2017 Single courses
Ingegneria Nautica
University of Genova, La Spezia, Italy

2013-2016 B.Sc. study
Ingegneria Aerospaziale
Politecnico di Milano, Milano, Italy

Work Experience

2021-2022 Junior Researcher
Delft University of Technology

Curriculum vitae

2019-2020	Intern - Graduate Student MARIN and Delft University of Technology
2017-2018	Intern CNR-INSEAN

List of publications

Journal papers:

S. Alkhateeb, F. Riccioli, F. L. Morales, and L. Pahlavan, “Non-contact acoustic emission monitoring of corrosion under marine growth,” *Sensors*, vol. 23, no. 1, p. 161, Jan. 2023, doi: 10.3390/s23010161.

F. Riccioli, A. Huijter, N. Grasso, C. M. Rizzo, and L. Pahlavan, “Development of a retrofit layer with an embedded array of piezoelectric sensors for transient pressure measurement in maritime applications,” *Marine Structures*, vol. 89, p. 103395, Apr. 2023, doi: 10.1016/j.marstruc.2023.103395.

F. Riccioli, Ø. Gabrielsen, I. S. Høgsæt, P. S. Barros, and L. Pahlavan, “Corrosion-fatigue damage identification in submerged mooring chain links using remote acoustic emission monitoring,” *Marine Structures*, vol. 98, p. 103685, Aug. 2024, doi: 10.1016/j.marstruc.2024.103685.

F. Riccioli, S. Alkhateeb, A. Mol, and L. Pahlavan, “Feasibility assessment of non-contact acoustic emission monitoring of corrosion-fatigue damage in submerged steel structures,” *Ocean Engineering*, vol. 312, p. 119296, Nov. 2024, doi: 10.1016/j.oceaneng.2024.119296.

F. Riccioli, H. den Besten, and L. Pahlavan, “Feasibility assessment of crack growth prognosis in submerged mooring chains using remote acoustic emission monitoring,” submitted to *Structural Health Monitoring*, 2025.

Conference papers:

D. Dessi, E. Faiella, and F. Riccioli, “A procedure for the identification of hydrodynamic damping associated to elastic modes,” in *Practical Design of Ships and Other Floating Structures: Proceedings of the 14th International Symposium PRADS 2019*, Yokohama, Japan, Sep. 22–26, 2019, vol. II, pp. 305–320, Springer Singapore, 2021, doi: 10.1007/978-981-15-9279-8_21.

F. Riccioli and L. Pahlavan, “Non-contact acoustic emission monitoring of corrosion-fatigue damage in submerged steel structures,” in *Proceedings of Structural Health Monitoring 2023*, Palo Alto, CA, Sep. 2023.

F. Riccioli, A. Tyto, and L. Pahlavan, “Non-contact acoustic emission monitoring of corrosion in mooring chain links,” in *Proceedings of Structural Health Monitoring 2024*, Sep. 2024.

